Atomic-scale Studies of Confined & Correlated Electron States on Semiconductor Surfaces

Asif M. Suleman

A dissertation submitted in partial fulfillment

of the requirements for the degree of

Doctor of Philosophy

of

University College London.

Department of Physics & Astronomy

University College London

December 19, 2017

I, Asif M. Suleman, confirm that the work presented in this thesis is my own. Where information has been derived from other sources, I confirm that this has been indicated in the work.

Abstract

I have investigated atomic-scale condensed matter, with a view towards future technology, covering two areas: point defects in a well studied and used system, Si; and a less studied semiconductor, MoS_2, where I have focussed on the fundamental properties and have observed charge density waves (CDWs).

Scanning tunnelling microscopy (STM) has been used over the past two decades to investigate semiconductor point defects. Here, an investigation of dangling bonds (DBs) on H-terminated Si(001) is presented. The STM tip is used to desorb H atoms to create DBs [1]. Pairs, or dimers, of DBs interact as their excited states overlap, signalled by a bright protrusion appearing between them [2]. Tip-induced band bending calculations show the dimer's excited state comes into tunnelling range at high biases and low currents. The energy alignment with the tip Fermi level is also affected by additional DBs in the vicinity. 2D structures of DBs, including trimers and tetramers, exhibited 2D excited states. By modelling each DB with a 2D potential well holding two bound states, we could simulate the DB structure's bound states. Using a tunnelling matrix element approximation, the bound states were combined to successfully re-create imaged quantum states.

STM has been used to study correlated ground states of layered materials, including transition-metal dichalcogenides (TMDs). Here, it is used to discover and characterise the CDW of K-intercalated MoS_2. This TMD is semiconducting but it is doped by the intercalating species, giving it metallic character and inducing superconductivity [3, 4]. The CDW was observed at temperatures of 78 K and below, appearing in patches localised to subsurface defects. The CDW coverage increased as the bias magnitude was decreased, however the wavevector or periodicity re-

mained invariant; a feature of CDWs. Other evidence presented includes a gap in the density of states and the occupied and unoccupied state modulations being out of phase.

Acknowledgements

First and foremost, I would like to thank my supervisor, Dr Steven Schofield, for providing me with the opportunity to complete a PhD, as part of his research group, in such an exciting field and with the guidance to help me develop as a research physicist.

I would also like to thank my second supervisor, Dr Neil Curson, and my unofficial third supervisor, Dr Cyrus Hirjibehedin, for their additional support and guidance and for always making time available to answer my questions. Discussions with Neil about football, and our regular battles in fantasy football, were a welcome relief from the busy research life.

In addition, I want to thank all members, past and present, of the larger Scanning Tunnelling Microsopy group that I had the pleasure of working with, for creating a great working atmosphere in lab B2.01, and always willing to provide a helping hand. This includes the PhD students: Adam Rahnejat, Manuel Siegl, Gareth Moore, Kitiphat Sinthiptharakoon, Muhammad Shu'aib Kamaludin, Alex Kölker, Ben Warner, Toby Gill, and Roland Leber; the post-doctoral researchers: Tingbin Lim, Holly Hedgeland, Taylor Stock, and Henning Prüser; and the various master's and summer project students during my time. In particular, Adam and Kitiphat, for teaching me how to use a scanning tunnelling microscope, and Tingbin, for baking such great cakes for our Journal Club meetings—a weekly highlight.

A special mention to my collaborators, Dr Chris Howard and his student Mohammed Kashim Subhan, for fabricating the molybdenum disulfide samples I studied and for giving me an insight into the fascinating world of layered materials. Much was gratefully learnt from our many fruitful discussions on reciprocal space

and data analysis techniques.

Finally, I thank my parents, Bashir and Naseem, and my brother, Sohib, for their unconditional help and encouragement, during this long journey, and for always being there when I needed them. Without such support I would not have been able to complete my PhD.

Contents

List of Figures

List of Tables

Chapter 1

Introduction

For the past half century, advances in technology have been following the path laid out by Moore's law, which states that the number of transistors on an integrated circuit doubles approximately every year and a half, in order to keep satisfying the processing demands of software programs [5]. Simultaneously, consumers are increasingly preferring smaller, lighter electronic devices, moving on from desktop personal computers to hand-held smartphones. As a result, integrated circuits cannot expand in size and instead it is the transistors that have to be scaled down [38]. The two trends of Moore's law and the miniaturisation of electronics are illustrated in Figure 1.1. Further advantages of miniaturised electronics are that it is able to process faster and consume less power.

Switches and transistors have already reached dimensions on the order of tens of nanometres and in the next decade, they are expected to move towards the atomic-scale. In this regime, continuous charge distributions and smooth surfaces no longer apply, meaning that small, individual atomic differences in otherwise identical transistors can result in differing properties [38]. Additionally, the dielectric, oxide layer is now thin enough to possibly allow for electrons to quantum mechanically tunnel across. Another issue is that recent transistor densities have led to excessive heat production and subsequent restrictions to ensure product safety.

This all points towards the need to identify new systems, possibly quantum related, for devising and building next-generation electronic devices. Point defects in semiconductors have been touted as potential candidates, capable of trapping and

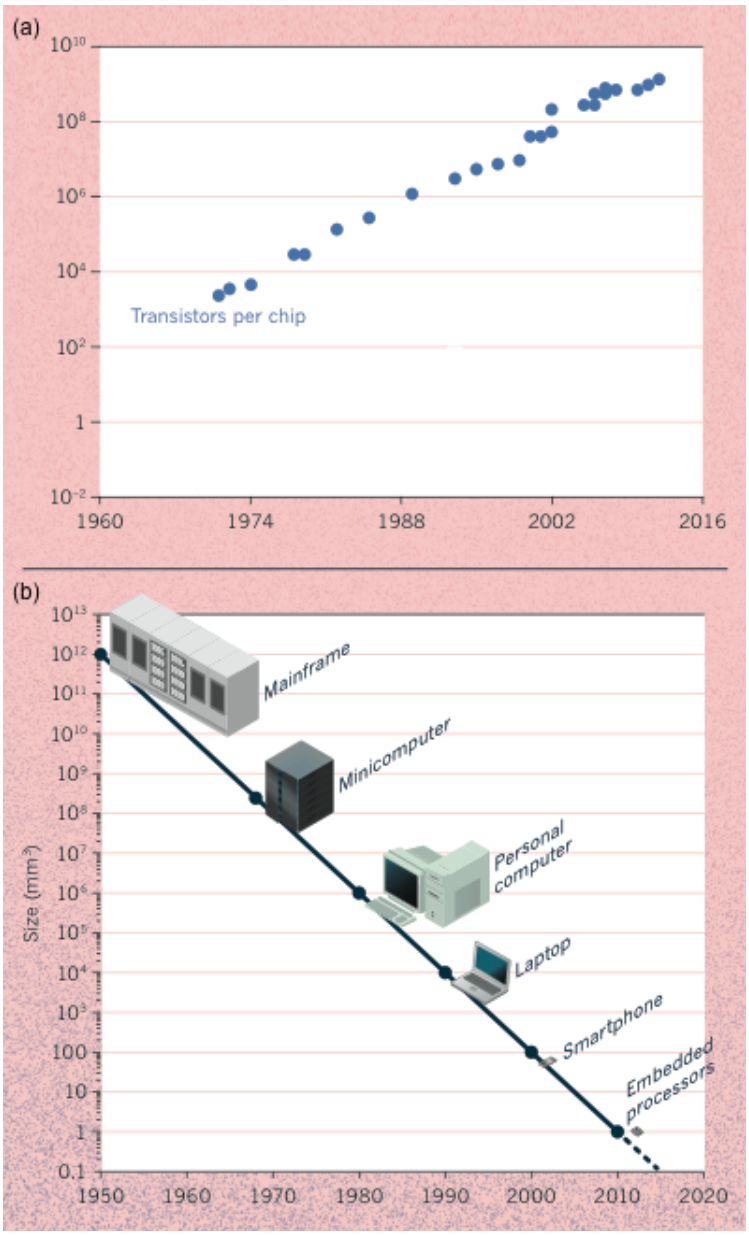

Figure 1.1: (a) A plot displaying Moore's law and (b) a plot displaying the scaling down of computer sizes in accordance with Moore's law. Figure reproduced from Reference [5].

confining individual charge carriers [39]. Such zero-dimensional quantum dots will always be identical, and those related to the Si(001) surface, which is the foundation of modern electronics, are ideal in order to maintain continuity with today's current technologies. Moreover, the impact of such research will be felt with regards to fundamental condensed matter physics, including investigations into methods to precisely fabricate defects in chosen locations and the physics behind the interactions

of defects with one another and with the semiconductor host.

My investigations have included creating dangling bond defects on the hydrogen-terminated silicon (001) surface, using scanning tunnelling microscopy to perform hydrogen-lithography. Dangling bonds have been created in one- and two-dimensional structures, for an ensuing study of how the dangling bonds interact as their individual quantum bound states overlap. It was examined how varying the imaging settings and the creation of an additional dangling bond in the vicinity can influence the appearance of the excited bound states of the defect structure. Two-dimensional structures, containing three or four dangling bonds, displayed quantum bound states that span two-dimensions, and it was explored how the symmetry of the structure with respect to the dimerised reconstruction of the silicon surface can affect said interactions and the ordering of the quantum bound states.

More recently, fundamental research conducted on atomically-thin, two-dimensional (2D) materials has been of great interest [40]. Investigated 2D layers include: the 2D allotropes of Group IV and V elements, such as graphene, an allotrope of carbon, the first and most famous example; silicene, an allotrope of silicon; and phospherene, an allotrope of phosphorus; single layers of transition-metal dichalcogenides, for example molybdenum disulfide, which has differing properties when in monolayer form compared to bulk form; and other 2D compounds like insulating hexagonal boron nitride.

Such studies are concerned with understanding the origins of the exotic physics on display and creating heterostructure devices of nanoscale thickness, which would offer great flexibility. These structures would contain several different 2D layers, stacked in an order or configuration that makes use of each individual layer's interesting properties and characteristics. With the layers held together by van der Waals forces, analogous to the way many of these monolayers stand in their natural bulk form, such that lattice mismatch is not an issue. One current proposal by F. Withers *et al.* uses graphene layers as gates, boron nitride layers as dielectrics and a layer of molybdenum disulfide as the semiconductor — see Figure 1.2. The direct band gap of single-layer MoS_2 makes this a potential opto-electronic device [41, 6].

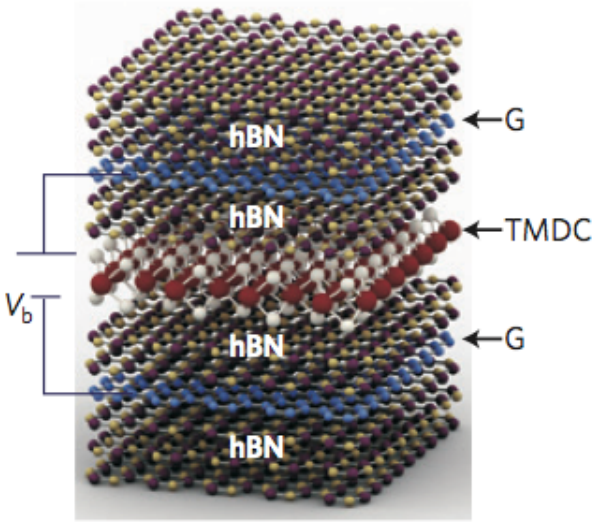

Figure 1.2: Schematic diagram of Withers' van der Waals heterostructure, of stacked graphene (G), boron nitride (hBN) and molybdenum disulfide (TMDC) layers. Image is reproduced from Reference [6].

Scanning tunnelling microscopy and spectroscopy studies of 2D materials is of particular interest because this instrumentation allows one to simultaneously explore the physical and electronic properties of the surface at the atomic-scale. In low-temperature topographic images of the surface, exotic, correlated, electronic phases hosted by the 2D material, such as charge density waves, can be discovered and observed. Combining imaging with spectroscopy can lead to the spatial mapping of the local density of states and the ability to directly associate features in the spectroscopy to changes in structure, for example the appearance of a gap in the band structure due to a charge density wave.

Using this experimental technique of low-temperature scanning tunnelling microscopy and spectroscopy, a charge density wave state of an intercalated form of molybdenum disulfide has been discovered and characterised. The molybdenum disulfide sample used was electronically doped by intercalation with potassium, giving it metallic character. Its charge density wave was initially observed in patches surrounding a defect, with the coverage and intensity increasing as the magnitude of the sample bias was decreased. Characterisation of this commensurate charge density wave included determining the wavevector and, subsequently, the periodicity of the modulations, and measuring the energy gap in the density of states. The

results are reported and analysed in this thesis.

Chapter 2

Background theory

2.1 Scanning Tunnelling Microscopy

A scanning tunnelling microscope (STM) is a tool used for imaging and studying conducting and semi-conducting surfaces with an extremely high resolution; on the atomic-scale [42, 43]. Since its invention, its capabilities have broadened to include spectroscopy and atomic manipulation [44] techniques. An STM functions by scanning a metal probe tip across the surface of a metal or semi-conducting sample, see Fig. 2.1. This tip is positioned a few angstroms (Å), approximately between 3 to 8 (Å), above the sample. The use of piezoelectric crystals allows for very fine controlled movements of the tip. When a bias voltage is applied across the tip-vacuum-sample junction, electrons are capable of quantum tunnelling across the potential barrier in the vacuum gap. This tunnel current is compared to a user defined set-point current, via a pre-amplifier; if the tunnel current is higher than the set-point the tip is retracted from the sample, and if the current is lower the tip approaches closer. This feedback loop determines an equilibrium height as the tip scans the surface; and in this process a contour plot is produced displaying the equilibrium heights, z-coordinate, for each set of x-y coordinates in the surface plane. Therefore, the contour plot corresponds to a surface of equal tunnelling current, equal to the set-point value, which can be transformed into an image of the surface topography.

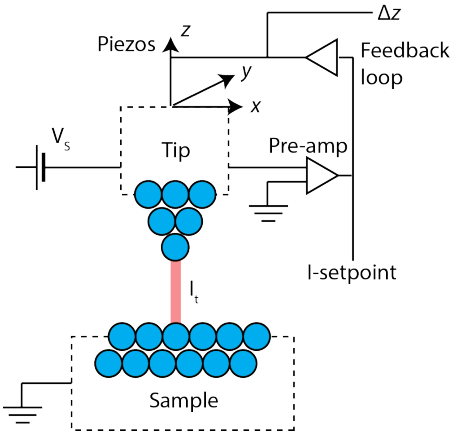

Figure 2.1: Schematic diagram of the STM set-up.

2.1.1 Quantum-mechanical tunnelling

Classically it would be expected that a travelling particle would not be able to pass through a potential barrier if its energy E is less than the barrier height U ($E = \frac{\hbar^2 k^2}{2m}$, where $\hbar$ is the reduced Planck's constant, k is the wavevector and m is the particle mass.). However, according to quantum mechanics there is a small possibility of the particle passing through the barrier.

In this section, the basic one-dimensional approximation for tunnelling is described [45]. The particle wavefunction (ψ) is in the form of a travelling wave before and after the barrier, but within the barrier there is an exponential decay of the wavefunction, see Fig. 2.2, so that after tunnelling the amplitude of ψ has decreased. Upon entering the barrier, part of the wave is reflected back along its incident path. By solving the Schrödinger equation and applying appropriate boundary conditions, where ψ and its first derivative remain continuous, the wavefunction of the particle

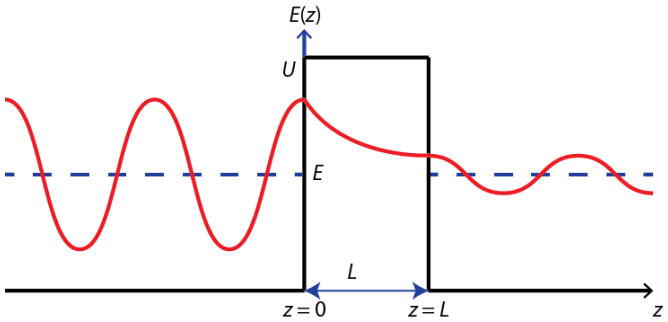

Figure 2.2: A particle of energy E tunnelling through a potential barrier of height U and width L.

in the barrier region can be determined. The following, is a simplified determination of the tunnelling, or transmission, probability (w), resulting from consideration of the direction of the travelling particle and its decaying wavefunction [43].

Consider the region outside the potential barrier, here the Schrödinger equation becomes

$$\frac{\hbar^2}{2m}\frac{d^2\psi}{dz^2} - E\psi = 0, \tag{2.1}$$

which has the following plane wave solution:

$$\psi = Ae^{ikz} + Be^{-ikz}, \tag{2.2}$$

where A and B are constants and

$$k = \frac{\sqrt{2mE}}{\hbar}. \tag{2.3}$$

Within the barrier, where $U > E$, the following is true,

$$\frac{\hbar^2}{2m}\frac{d^2\psi}{dz^2} + (U-E)\psi = 0, \tag{2.4}$$

for which the wavefunction is

$$\psi = Ce^{\kappa z} + De^{-\kappa z}, \tag{2.5}$$

where C and D are constants and the decay constant is

$$\kappa = \frac{\sqrt{2m(U-E)}}{\hbar}. \tag{2.6}$$

Here ψ is the sum of two real functions. Considering the solution that decays left to right, as illustrated in Figure 2.2, therefore the probability density is given by

$$|\psi|^2 = |D|^2 e^{-2\kappa z}, \tag{2.7}$$

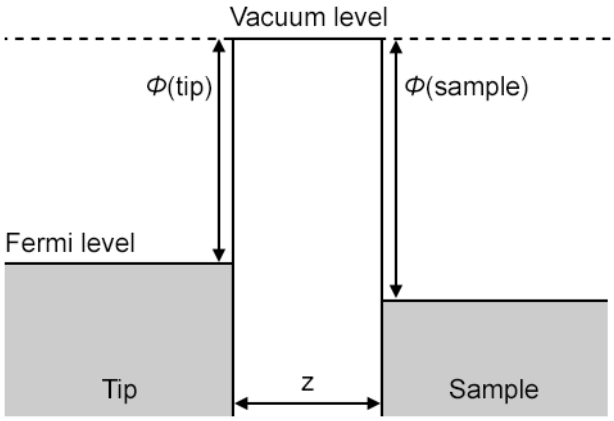

Figure 2.3: A metal-vacuum-metal tunnelling junction, where 'ϕ' depicts the work function and 'z' is the tip-sample separation.

and

$$w \propto e^{-2\kappa L}, \tag{2.8}$$

where L is the barrier width.

In the case of an STM, the particle is an electron and the potential barrier is due to the vacuum gap. The barrier height is given by the work functions (ϕ) of tip and sample, and the width is the tip-sample separation (z), as illustrated in Figure 2.3. The electron tunnelling probability has an exponential dependence on the tip-sample separation, making it highly responsive to small changes in the tip height which is what gives the STM its extraordinarily high height resolution. Using a typical value of 5 eV for ϕ, then for every angstrom the tip approaches the sample, the tunnelling current increases by approximately an order of magnitude.

2.1.1.1 Particle flux explanation to tunnelling

In order to obtain the full equation for the probability of tunnelling, one has to consider the particle flux (Γ) for the travelling particles [45]. The particle flux, sometimes referred to as the probability flux, is the rate of the average number of particles flowing past a point (z).

$$\Gamma(z) = \frac{-i\hbar}{2m}\left(\psi^* \frac{\partial \psi}{\partial z} - \psi \frac{\partial \psi^*}{\partial z}\right) \tag{2.9}$$

For a wavefunction of the form,

$$\psi(z) = Ae^{\pm ikz}, \tag{2.10}$$

where A is a constant, the particle flux is,

$$\Gamma(z) = \frac{\hbar k}{m}|A|^2, \tag{2.11}$$

determined using Equation 2.9.

Referring to Figure 2.2: for the region to the left of the potential barrier (1), the wavefunction is given by Equation 2.2; for the region inside the barrier (2), the wavefunction takes the form of Equation 2.5; and for the region to the right (3), the wavefunction is

$$\psi = Fe^{ikz}. \tag{2.12}$$

The wavefunction, after passing through the potential barrier, only holds one term because it is certain the particles will only be travelling in the positive z-direction. The incident, reflected, and transmitted beams are described by Ae^{ikz}, Be^{-ikz}, and Fe^{ikz}, respectively. Moreover, A is known to be non-zero, since it is certain all the incident particles are moving from left to right, along the positive z-direction, and it is expected to be one as the wavefunction is usually normalised to one particle per unit length.

The first derivative of the wavefunction for the three regions is as follows,

$$\psi_1'(z) = ike^{ikz} - ikBe^{-ikz},$$

$$\psi_2'(z) = \kappa Ce^{\kappa z} - \kappa De^{-\kappa z},$$

$$\psi_3'(z) = ikFe^{ikz}.$$

Keeping the wavefunction and their derivatives continuous at the barrier edges, $z = 0$ and $z = L$, leads to,

$$1 + B = C + D,$$

$$1 - B = \frac{\kappa}{ik}C - \frac{\kappa}{ik}D,$$

$$Ce^{\kappa L} + De^{-\kappa L} = Fe^{ikL},$$

$$Ce^{\kappa L} - De^{-\kappa L} = \frac{ik}{\kappa}Fe^{ikL}.$$

Using these boundary conditions, the constants, including F, can be determined.

$$F = \frac{4ik\kappa}{(\kappa + ik)^2 e^{-\kappa L} - (\kappa - ik)^2 e^{\kappa L}} e^{-ikL} \tag{2.13}$$

The probability of tunnelling through the barrier is given by the ratio of the probability, or particle flux, of transmission to the probability of incidence,

$$w = \left| \frac{\Gamma_{\text{transmitted}}}{\Gamma_{\text{incident}}} \right| = \left| \frac{\frac{\hbar k}{m}|F|^2}{\frac{\hbar k}{m}|A|^2} \right| = |F|^2, \tag{2.14}$$

using Equation 2.11 and the fact that $A = 1$. Therefore,

$$w = |F|^2 = \frac{16k^2\kappa^2}{|(\kappa + ik)^2 e^{-\kappa L} - (\kappa - ik)^2 e^{\kappa L}|^2}. \tag{2.15}$$

Usually $\kappa L \gg 1$ and thus $e^{\kappa L} \gg e^{-\kappa L}$, for this reason the $e^{-\kappa L}$ term can be ignored.

$$w \approx \frac{16k^2\kappa^2}{|(\kappa - ik)^2 e^{\kappa L}|^2} = \frac{16k^2\kappa^2}{(\kappa^2 + k^2)^2} e^{-2\kappa L} \tag{2.16}$$

Substituting equations for k (Equation 2.3) and κ (Equation 2.6) gives the following,

$$w = \frac{16E(U - E)}{U^2} e^{-2\kappa L}. \tag{2.17}$$

Relating this back to Equation 2.8, it has the same dependence on L, justifying the earlier simplification.

2.1.1.2 Tersoff-Hamaan theory

This theory applies knowledge of electron tunnelling through a metal-insulator-metal junction to STM, in order to formulate an equation for the tunnel current [43, 46].

Assume the work function of the tip and sample are equal, which is a good approximation for a tungsten tip and silicon sample. The work function for tungsten is about 4.5 eV. In the case of a semiconductor, the work function equivalent value is given by $\chi + (E_C - E_F)$, where χ is the electron affinity (4.05 eV for silicon), E_C is the conduction band minimum and E_F is the Fermi level. The difference $(E_C - E_F)$ is expected to be small for a highly n-type sample, around 25 meV.

Applying a small sample bias voltage (V_s) will allow electrons to tunnel from occupied sample states, within the bias range $E_F - eV_s$ to E_F, to empty tip states. The small bias ensures that the tip and sample Fermi levels E_F are almost equal and all the states involved in tunnelling are close to E_F.

The local density of states for the sample, i.e. the number of states per unit volume and per unit energy, at a position r and energy E, is as follows

$$\rho_s(r,E) = \frac{1}{eV_s} \sum_{E-eV_s}^{E} |\psi(r)|^2. \tag{2.18}$$

If V_s is small, it can be assumed that $\rho_s(r,E)$ remains constant with respect to E.

The tunnel current is proportional to the sum of the sample states within this small bias range and thus it can be defined by the following summation

$$I_t \propto \sum_{E_F-eV_s}^{E_F} |\psi(r_0)|^2 e^{-2\kappa z}. \tag{2.19}$$

Using the definition of $\rho_s(r,E)$ in Equation 2.18 gives

$$I_t \propto V_s \rho_s(r_0, E_F) e^{-2\kappa z} \tag{2.20}$$

$$\propto V_s \rho_s(r_z, E_F), \tag{2.21}$$

where $\rho_s(r_0, E_F)$ is the local density of sample states at the sample surface and $\rho_s(r_z, E_F)$ is the equivalent but at the position of the tip. The tip surface states are not included in this expression since they are usually represented by a single s-type orbital, in other words they are a constant which is acceptable for a clean, metal tip. Therefore, according to Tersoff-Hamaan theory [47], a constant-current STM

image is in fact a contour representing a surface of constant local density of sample states at the Fermi level.

2.1.1.3 Wentzel-Kramers Brillouin theory

While the Tersoff-Hamaan approximation may be true for metals at low biases, it is a crude approximation for semiconductors. Usually much higher scanning biases, commonly around 2 V, are used for imaging semiconductors like silicon. In this regime, all the states in the bias window between E_F and $E_F + V_s$ are involved in tunnelling. According to Wentzel-Kramers Brillouin (WKB) theory [46], which assumes planar tunnelling, the tunnelling current is

$$I_t = \int_0^{eV} \rho_s(r,E)\rho_t(r,-eV_s+E)T(E,eV_s,r)\,dE, \tag{2.22}$$

where $\rho_s(r,E)$ and $\rho_t(r,E)$ are the same as before, local density of states for the sample and tip, respectively, and $T(E,eV,r)$ is the tunnelling transmission probability and it has an exponential form.

$$T(E,eV,r) = \exp\left(-\frac{2z}{\hbar}\sqrt{2m\left(\frac{1}{2}(\phi_s+\phi_t+eV_s)-E\right)}\right), \tag{2.23}$$

where z is again the tip-sample separation and ϕ_s and ϕ_t are the work functions of the sample and tip, respectively. In this case, a constant-current STM image is a contour representing a function of density of sample states, density of tip states, and the tunnelling transmission probability.

2.1.2 Voltage-dependent imaging

The applied bias between the tip and sample can be referred to as a sample bias or a tip bias, with the two having opposite polarity i.e. a positive sample bias corresponds to a negative tip bias. Here the conventional sample bias will be preferred.

When imaging with a positive sample bias, the applied tip bias is negative. The tip Fermi level is raised above the sample Fermi level, and the empty, or unoccupied, states above the sample Fermi level are imaged. For a semiconductor these empty states normally lie in the conduction band, and in this case electrons are tunnelling

from the tip to the sample. This mode of operation is therefore known as empty- or unoccupied-states imaging.

In the alternative filled-state imaging mode, sometimes referred to as occupied-states imaging, the tip Fermi level is below the sample Fermi level. Electrons tunnel from the filled states, located in the valence band, of the semiconductor sample to the empty states of the tip.

In empty-states imaging, the tunnelling transmission probability $T(E, eV, r)$, in Equation 2.23, gives a greater probability of tunnelling to states closer to the Fermi level of the tip. In the filled-states, it gives a greater tunnelling probability to states closer to the sample Fermi level.

2.1.3 Scanning Tunnelling Spectroscopy

Spectroscopy of the electronic states of a metal or a semiconductor can be performed with an STM, this is known as scanning tunnelling spectroscopy STS. First the tip's position is fixed; the lateral position is chosen by the user and the height is regulated by the bias and tunnel current settings. The bias is then swept through a specified range and the resulting tunnel current changes are measured. This produces a current-voltage curve that can be numerically differentiated to give the differential conductance as a function of bias. This technique allows atomic-scale, spectroscopic examination of the surface electronic states with energies around the sample Fermi level.

The theory behind STS can be understood via the Bardeen approach [43]. It involves treating the wavefunction of the sample states ψ_s and tip states ψ_t separately and describing them by individual Schrödinger equations. It uses time-dependent perturbation theory and the Fermi golden rule to evaluate the tunnelling matrix element M, or the electron transfer rate between the sample and tip, which is an integral of ψ_s and ψ_t states across an arbitrary surface within the tunnelling gap, typically in the middle.

$$M = \frac{\hbar}{2m} \int \left(\psi_t^* \frac{\partial \psi_s}{\partial z} - \psi_s \frac{\partial \psi_t^*}{\partial z} \right) dS \tag{2.24}$$

M essentially is a measure of the tip's influence on the sample states and, vice-versa,

the sample's influence on tip states.

The probability of elastic tunnelling from ψ_s states, of energy E_{ψ_s}, to ψ_t states, of energy E_{ψ_t}, is given by

$$w = \frac{2\pi}{\hbar}|M|^2\delta(E_{\psi_s} - E_{\psi_t}). \tag{2.25}$$

In this case, the tunnel current is an integral across all occupied sample states and degenerate unoccupied tip states and is described by

$$I_t = \frac{4\pi e}{\hbar}\int_{-\infty}^{+\infty}(f(E_F - eV_s + E) - f(E_F + E))\cdot\rho_s(E_F - eV_s + E)\rho_t(E_F + E)|M|^2\,dE, \tag{2.26}$$

where V_s is the applied sample bias, $\rho_s(E)$ and $\rho_t(E)$ are the density of states of the sample and tip, respectively, and $f(E)$ is the Fermi-Dirac distribution.

$$f(E) = \frac{1}{1+\exp(\frac{E-E_F}{k_BT})}, \tag{2.27}$$

k_B is Boltzmann's constant and T is temperature. At low temperatures, $f(E)$ takes the form of an approximate step function and assuming $|M|$ remains constant within the bias range, then the tunnel current expression simplifies to a convolution of $\rho_s(E)$ and $\rho_t(E)$:

$$I_t \propto \int_0^{eV_s}\rho_s(E_F - eV_s + E)\rho_t(E_F + E)\,dE. \tag{2.28}$$

This means that a feature in the STS may be due to a characteristic of $\rho_s(E)$ or $\rho_t(E)$. However, using a metal tip, one can assume a constant and featureless $\rho_t(E)$ and now the differential conductance is directly proportional to the sample density of states:

$$\frac{dI}{dV} \propto \rho_s(E_F - eV_s). \tag{2.29}$$

Averaging a large number of experimentally obtained STS curves can help to rule out tip changes as a source of features.

2.1.4 Tip-induced Band Bending

When the electrostatic potential of the STM probe tip reaches the semiconductor sample, during STM imaging, it causes a local distortion in the electronic bands and states. This is known as tip-induced band bending (TIBB) [48].

This band bending, towards and away from the constant Fermi level, can lead to a spatially localized accumulation, depletion, or inversion of majority charge carriers. That is, an increase or decrease in the number of electrons (holes) for an n-type (p-type) semiconductor, or complete inversion between n- and p-type.

TIBB is analogous to the gating effect in a metal-oxide-semiconductor field-effect transistor (MOSFET) [49, 50], which is where this band bending effect was first observed. The metal film forming the gate of the MOSFET is analogous to the STM tip, while the insulating oxide layer and underlying semiconductor substrate are analogous to the vacuum gap and sample, respectively. A comparison between STM and a MOSFET is made in Figure 2.4.

Applying a charge to the metal gate induces an opposite charge on the semiconductor. Take the case of an n-type semiconductor, in empty-state imaging, see the energy level diagrams in Figure 2.5 (b), the gate voltage or tip bias is negative and the sample bias is positive. Electrons are repelled from the semiconductor surface, leading to depletion and upward band bending. In filled-state imaging, see panel (c) of Figure 2.5, the tip bias is positive and the sample bias is negative, resulting in an accumulation of electrons at the semiconductor surface and downward

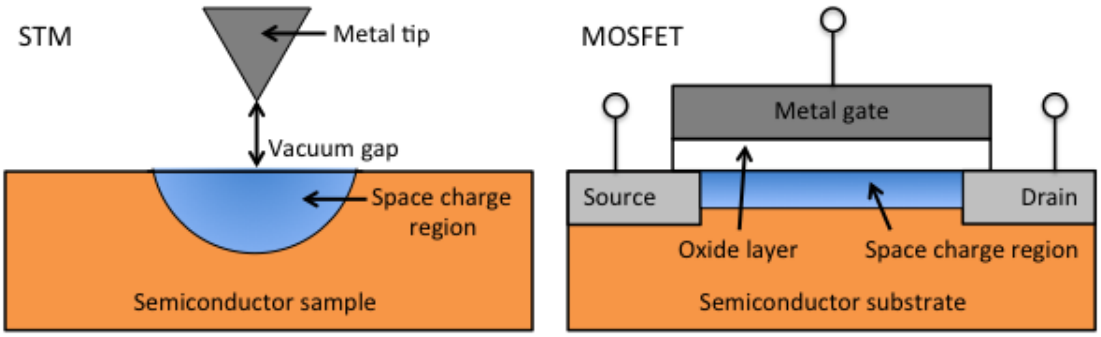

Figure 2.4: The band bending, and consequential space charge region, induced at the semiconductor surface in the analogous STM and MOSFET systems.

band bending.

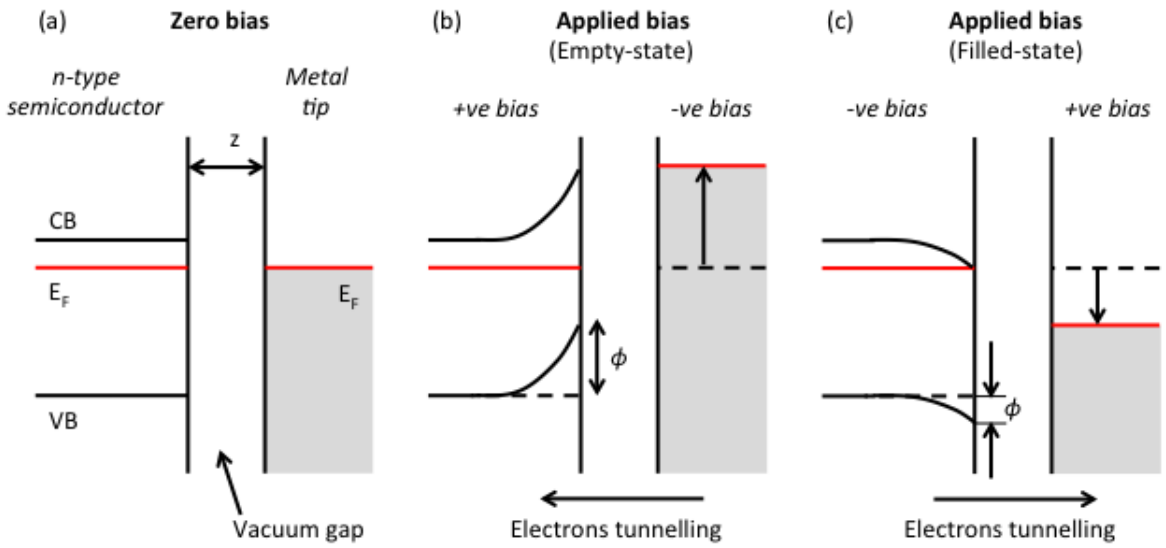

Figure 2.5: Energy level diagrams of the STM junction for the situation of (a) zero bias, assuming no contact potential, and an applied bias, in the case of (b) empty-state and (c) filled-state imaging. Where z is the tip-sample separation, E_F is the Fermi level, CB is the conduction band, VB is the valence band and ϕ is the TIBB at the surface. A rigid band bending model is assumed.

TIBB, ϕ, can be calculated using Poisson's equation:

$$\nabla^2\phi = -\frac{\rho}{\varepsilon_r\varepsilon_0},$$

where ρ is the charge density of the semiconductor sample, ε_r is the relative permittivity (or dielectric constant) of the semiconductor and ε_0 is the permittivity of free space. The charge density is given by:

$$\rho = e(p - n + N_D^+ - N_A^-), \tag{2.30}$$

and includes the density of electrons n, holes p, ionised donors N_D^+ and ionised acceptors N_A^-, e being the electron charge. ρ is a function of the Fermi level position. The densities for each of the four charged species are based on Fermi-Dirac statistics, and are derived and given in Appendix A. Integrating Poisson's equation will give the electric field, $\xi = -\nabla\phi$, and applying boundary conditions, that the electric displacement, $D = \varepsilon_r\varepsilon_0\xi$, is constant at the semiconductor-vacuum interface,

determines the TIBB.

Poisson's equation can be solved analytically for the one-dimensional case.

$$\frac{d^2\phi}{dz^2} = -\frac{\rho}{\varepsilon_r\varepsilon_0}$$

Integrating Poisson's equation from the neutral bulk, i.e. the Fermi level, to the surface of the semiconductor gives the electric field at the surface.

$$\int_{bulk}^{surf} \frac{d^2\phi}{dz^2}\, d\phi = -\frac{1}{\varepsilon_r\varepsilon_0}\int_{bulk}^{surf} \rho\, d\phi \tag{2.31}$$

$$\int_0^{\frac{d\phi}{dz}} \frac{d\phi}{dz}\, d\left(\frac{d\phi}{dz}\right) = -\frac{1}{\varepsilon_r\varepsilon_0}\int_{\phi_{E_F}}^{\phi} \rho\, d\phi \tag{2.32}$$

$$\frac{1}{2}\left(\frac{d\phi}{dz}\right)^2 = -\frac{1}{\varepsilon_r\varepsilon_0}\int_{\phi_{E_F}}^{\phi} \rho\, d\phi \tag{2.33}$$

$$\xi = \sqrt{-\frac{2}{\varepsilon_r\varepsilon_0}\int_{\phi_{E_F}}^{\phi} \rho\, d\phi}. \tag{2.34}$$

Applying boundary conditions to the electric field result, such that the constant electric displacement drop across the vacuum gap is equal to the electric displacement on the semiconductor surface, will determine ϕ. For a metal–vacuum–metal junction all the potential is dropped in the vacuum gap, whereas if one of the electrodes is a semiconductor, then the potential is partially dropped in the vacuum region with the remaining dropped at the surface region of the semiconductor. Here, it is being assumed that there is no contact potential. The Fermi level of the tip aligns with the Fermi level of the sample when no bias is applied, and the junction behaves like a parallel plate capacitor, where the tip and sample are the parallel plates and the vacuum gap is the dielectric in between. This idea is used to compute the electric field across the vacuum region.

$$\begin{aligned} D_{vac} &= D_{surf} \\ \varepsilon_0\xi_{vac} &= \varepsilon_r\varepsilon_0\xi \\ \varepsilon_0\left(\frac{\phi_T - \phi}{z}\right) &= \varepsilon_r\varepsilon_0\xi. \end{aligned}$$

Rearranging gives the tip potential ϕ_T, the energy by which the tip Fermi level is raised, as a function of the TIBB ϕ,

$$\phi_T = \phi + z\varepsilon_r\xi. \tag{2.35}$$

Here z is the tip-sample separation. The equation derived above leads to the band bending behaviour shown in the energy level diagrams of Figure 2.5, once you have inserted an appropriate expression for the charge density ρ into the electric field ξ expression.

2.2 The Si(001) surface

The Si(001) surface is the surface upon which microelectronics are built. This surface is thus of extreme technological importance. Atomic-scale investigations of this surface are becoming more significant, considering the ongoing miniaturisation of electronics.

Theoretically, cutting a bulk Si sample at the (001) plane will initially reveal a square arrangement of Si atoms on the surface, where each atom is bonded to two atoms in the layer below. Since a Si atom can form four bonds in total, it additionally hosts two dangling bonds, each holding a single electron. This 1×1 reconstruction has a surface lattice constant of 0.383 nm, whereas the bulk value is 0.542 nm.

However, the surface energy can be lowered by reducing the number of dangling bonds (DBs), Si atoms thus pair up via σ bonds to form dimers. In turn, these dimers form rows running along the (110) direction. The result is the 2×1 surface reconstruction, which has a metallic nature.

The strong σ bond of the dimer brings the two Si atoms closer together, resulting in limited overlap between the remaining singly occupied DBs, creating a weak π bond. Within these π bonds, charge is redistributed to further lower the surface energy producing buckling of the dimers, a consequence of Jahn-Teller distortions. A dimer now consists of an 'up' atom, of greater charge, its DB is sp^3-like, and a 'down' atom, of lesser charge, its DB is sp^2-like. The buckling alternates along and

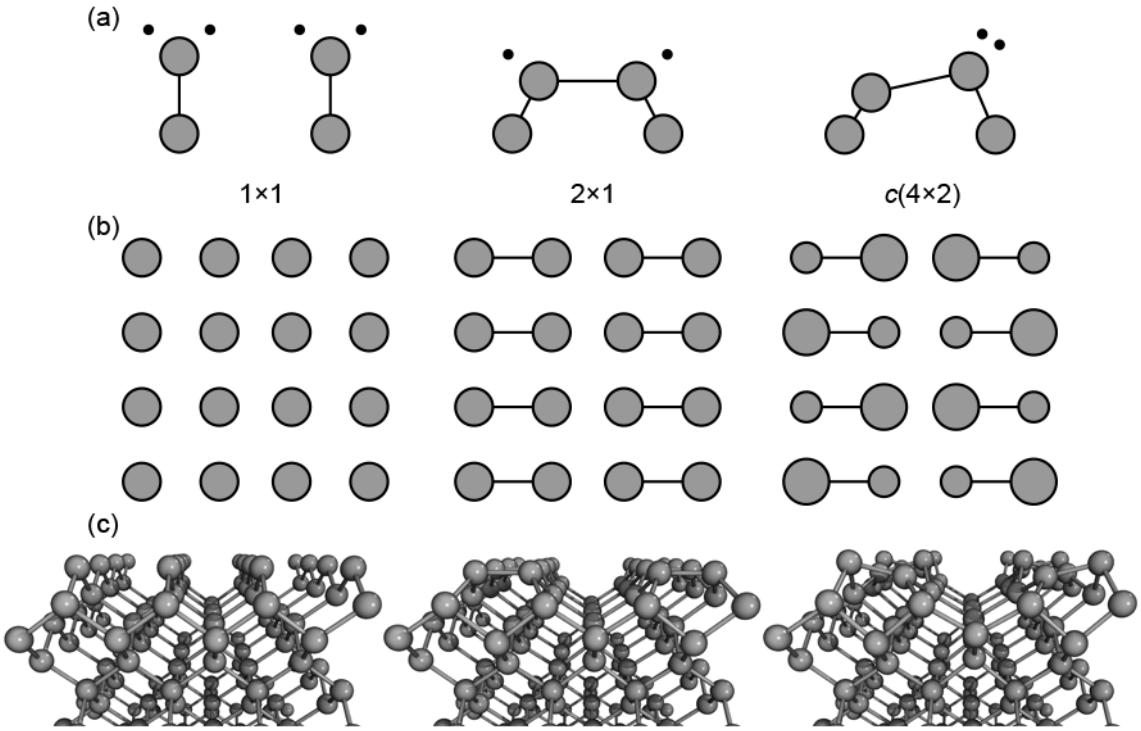

Figure 2.6: (a) Side, (b) top and (c) perspective views of the 1×1, 2×1 and $c(4 \times 2)$ surface reconstructions of Si(001). The 2×1 reconstruction has symmetric dimers and the $c(4 \times 2)$ reconstruction has buckled dimers. The grey circles denote Si atoms and the black dots denote electrons in a dangling bond. For the top view of $c(4 \times 2)$, the large circles represent up atoms and the small circles represent down atoms. The side view (a) of the $c(4 \times 2)$ reconstruction, in this figure, is an approximation: both electrons do not completely transfer to the up atom, some charge remains on the down atom.

across the dimer rows, in a $c(4 \times 2)$ arrangement. The buckled, asymmetric dimers were first proposed by D. J. Chadi [51]. Figure 2.6 summarises the 1×1, 2×1, and $c(4 \times 2)$ surface reconstructions and the steps undertaken in forming a buckled dimer, and this is the surface observed experimentally.

In the buckled dimer, the dimer bond is at an angle of about 20° to the surface plane and the length of the bond is approximately 0.23 nm. The two bonds from each surface Si atom to the atoms in the layer below only have to be rotated to accommodate the dimer and its buckling, with the bond length remaining the same. Therefore, the associated energy costs in forming the reconstruction are kept to a minimum. Terraces on the surface are separated by single atomic height steps, consequently the dimer row direction is perpendicular on adjacent terraces.

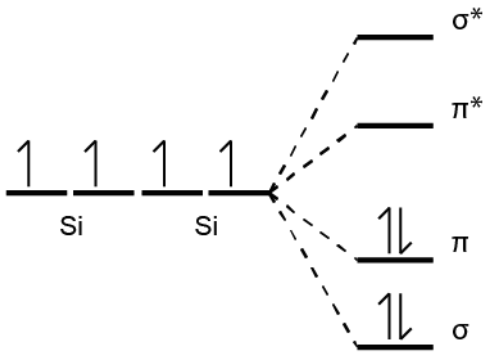

Figure 2.7: The bond formation and energy splitting that occurs when two Si atoms interact, each holding two singly occupied dangling bonds. The two σ states are in the Si electron bands, σ in the valence band and σ^* in the conduction band, and the two π states are in the Si band gap, separated by ~ 0.5 eV.

Figure 2.7 contains an energy level diagram showing the bonds produced during the construction of a buckled Si dimer. The energy splittings give a measure of the bond strength. The σ bond is relatively strong, demonstrated by the large gap between the occupied (σ) and unoccupied (σ^*) state. These two states can be imaged in STM at high filled-state and high empty-state bias voltages, respectively. Whereas for the π bond, the gap between the occupied (π) state, corresponding to the up atom, and the unoccupied (π^*) state, corresponding to the down atom, is small as expected for a weak bond. In STM imaging, the former is observed at low filled-states biases and the latter at low empty-states biases, see Figure 2.8. The presence of many dimers extends these states into bands and the energy gap between the surface state bands is around 0.5 eV, it can be measured in scanning tunnelling spectroscopy and it is proof the buckled dimerised surface is semiconducting.

Dimer buckling is observed in STM imaging at liquid nitrogen and liquid helium temperatures. But scanning at room temperature, symmetric dimers are observed because the higher temperature, and thus greater thermal energy, allows the buckling to constantly flip and the surface appears to be a 2×1 reconstruction; an average of the two buckled formations. The buckling can be pinned by surface defects, such as vacancies, allowing the $c(4 \times 2)$ reconstruction to be observed in localised regions at higher temperatures.

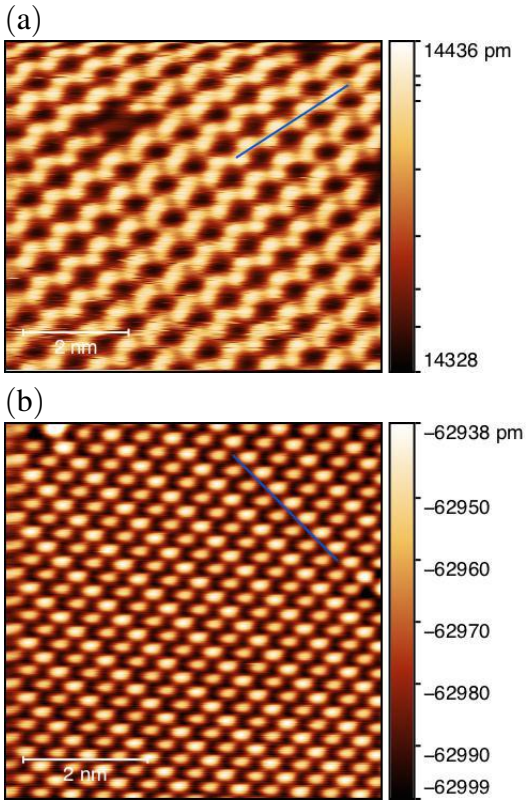

Figure 2.8: STM images taken at 77 K of (a) Si(001), −1.8 V and 50 pA, and (b) H-terminated Si(001), 1.1 V and 150 pA. Since (a) is a filled-states image of clean Si(001), the dimer row is imaged as a zig-zag of up atoms. The equivalent empty-states image would display the down atoms. Whereas (b) shows no buckling, just rows of symmetric dimers. The blue line denotes the dimer row direction and it lies across the centre of a dimer row. In image (b), the atoms on one side of the dimer row appear brighter than the other side, due to a double tip effect.

2.2.1 The Hydrogen-terminated Si(001) surface

Figure 2.9 displays the different possible hydrogen terminations of the Si(001) surface. The regular mono-hydride termination (b) has a 2×1 surface reconstruction.

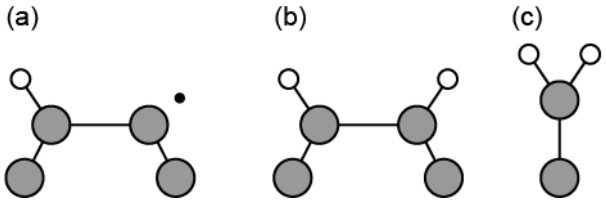

Figure 2.9: Schematic diagram of the (a) hemi-hydride, (b) mono-hydride and (c) di-hydride terminations. The grey circles denote Si atoms, the black dots denote electrons in a dangling bond and the white circles denote H atoms.

No dimer buckling is possible in this termination, since a single H atom has bonded to every Si atom through the single remaining DB, passivating the surface states in the process. For the di-hydride termination (c) to form it requires H atoms to break the σ bond of the Si dimer to allow two H atoms to be bonded to every Si atom. However, di-hydrides are usually found alongside mono-hydrides in a 3×1 reconstruction, alternating between di- and mono-hydrides across the dimer row direction [52].

The thermal desorption spectrum (TDS) for hydrogen from a H-terminated Si(100) surface, featured in Figure 2.10, has two desorption peaks at 400 and 520°C, respectively. But the oxygen and water levels only decrease after the second peak, suggesting the silicon surface only becomes exposed and oxidised after the second desorption. Although, there is hydrogen desorption at 400°C, sufficient hydrogen remains to cover and passivate the entire surface. Therefore the termination must change from the di-hydride phase to the mono-hydride phase. The second peak at

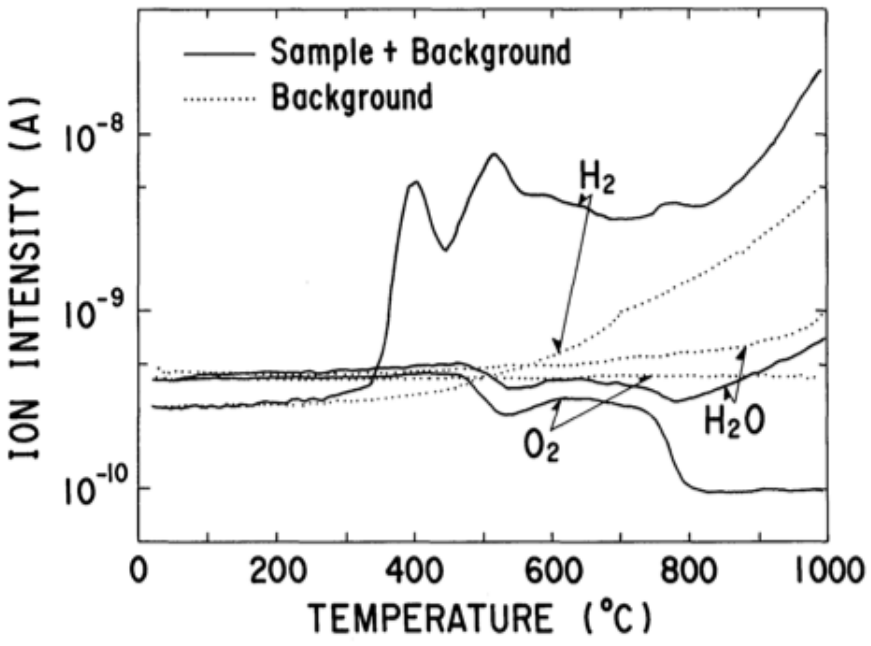

Figure 2.10: Thermal desorption spectra (TDS) of hydrogen, oxygen and water from a hydrogen terminated silicon surface, in an environment containing oxygen and water. Surface was hydrogen terminated by HF treatment. Figure reproduced from Reference [7].

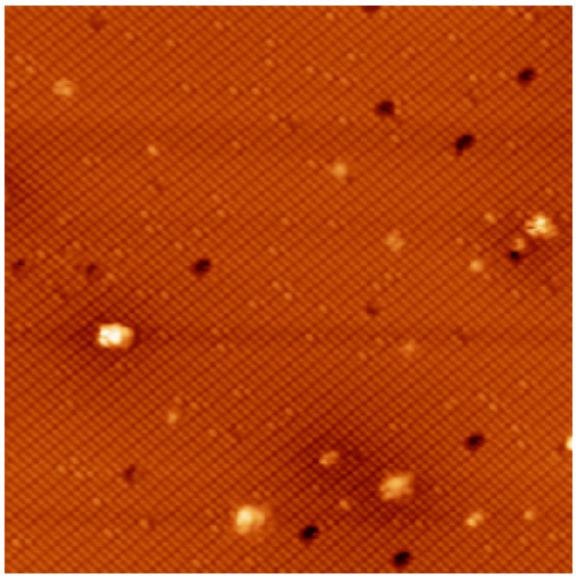

Figure 2.11: A large-scale, empty-state STM image of H-terminated Si(001) (settings: 1 V, 300 pA, 77 K and 25×25 nm^2).

520°C signals that enough hydrogen has been desorbed to leave the bare silicon surface exposed, to oxidation [7].

The STM image in Figure 2.11 is of a Si(001) surface with a mono-hydride termination and a 2×1 reconstruction. A similar STM image of smaller scale is displayed in Figure 2.8 (b). Each silicon atom is passivated by a single hydrogen atom and rows of symmetric dimers can clearly be seen. Yet a large density of oval shapes are present, which occupy the region of a dimer. These are single di-hydrides, and their large numbers suggest the termination process took place at a slightly lower temperature than the ideal conditions required for the mono-hydride phase. The appearance of a single di-hydride resembles that of a clean, unpassivated dimer, in both the empty- and filled-states. The dark depressions on the surface are dimer vacancies and the bright (tall) protrusions are clusters of dangling bonds, as patches of silicon atoms have not been terminated. Other protrusions, of lesser height, are contaminants.

2.3 Semiconductor point defects

Semiconductor point defects can be divided into two categories: hydrogenic defects, for example substitutional dopants, and deep centre defects [53, 54]. An example

of a hydrogenic defect is a substitutional dopant, like P donors in Si [55] and B acceptors in Si [8], and an example of a deep centre defect is the nitrogen-vacancy (NV^{-1}) centre in diamond [39]. Hydrogenic defects can be modelled with the effective mass approximation, i.e. a donor can be modelled like a hydrogen atom in a crystal field, but deep centre defects do not fit this model.

The energy of the n^{th} level in a hydrogen atom [56], given by

$$E_n = \frac{-me^4}{8\varepsilon_0^2 h^2}\frac{1}{n^2} = \frac{-13.58\text{ eV}}{n^2}, \tag{2.36}$$

where m is the electron mass, e is the electron charge, ε_0 is the permittivity of free space and h is Planck's constant.

When a donor element with an extra valency is introduced into a semiconductor host, such that the donor atom substitutes for a host atom in the lattice, one electron is left unaccounted for, and not involved in a bond, for every donor. The extra electron remains loosely bound and weakly attracted to its positively charged parent ion. Equation 2.36 can be applied to this system of donor atom and electron, however one has to consider that the electron is no longer free but moving through the field of the semiconductor crystal. Therefore, in response, the electron has an effective mass of m_e^* and the Coulomb potential of the impurity ion is screened by the relative permittivity ε_r of the semiconductor. Equation 2.36 now becomes

$$E_n = \frac{-(m_e^* m)e^4}{8(\varepsilon_r\varepsilon_0)^2 h^2}\frac{1}{n^2} = \frac{-31.45\text{ meV}}{n^2},$$

using the Si values of $m_e^* = 0.328$ and $\varepsilon_r = 11.9$ [57]. This value of -31.45 meV is an estimate of the ionisation energy of a typical donor in Si, e.g. P (45 meV [57]), As (54 meV [58]) and Sb (39 meV [58]), in other words it is a measure of the binding energy between the donated electron and the donor atom.

Unlike hydrogenic defects, which have small binding energies and much larger spanning wavefunctions, deep centre defects have highly localised potentials and wavefunctions that are spatially confined to length scales on the order of a lattice constant. Initially, the dividing factor was thought to be that deep centre defect

states lie deep in the band gap, hence the name, whereas hydrogenic defect states sit near the electron band edges, which is why they are sometimes referred to as shallow defects. But some overlap has been discovered since; some deep centres have been found to have electronic states nearer to the conduction band minimum and the valence band maximum.

2.3.1 Dangling Bonds

A dangling bond (DB) is a semiconductor point defect, in particular it is a type of deep centre defect. The P_b centre defect found at the silicon-silicon dioxide interface is an example of a dangling bond defect in the bulk [59], it is an electron trap state that has detrimental effects on the functioning of transistors. A DB can hold 0, 1 or 2 electrons, which correlate to a positive (DB^+), neutral (DB^0) or negative (DB^-) charge state, respectively. Moreover with the addition of each electron to the DB, the height of its host Si atom is raised with respect to the rest of the surface, as the DB orbital changes from sp^2-like to sp^3-like. In a fashion somewhat analogous to changing from a 'down' atom of a buckled dimer to an 'up' atom, see Section 2.2. Figure 2.12 displays the dimer buckling corresponding to the different DB charge states.

DBs can be controllably constructed on the surface of a semiconductor using scanning tunnelling microscopy (STM). Individually selected hydrogen atoms can be removed from an H-terminated Si(001) surface to create DBs, by utilising the STM tip. The passivating, monoatomic layer of hydrogen acts as a resist in this lithography technique. The desorption process entails an excitation of the Si-H

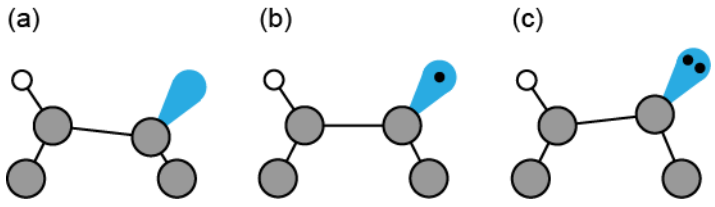

Figure 2.12: Schematic diagram of a dangling bond (DB) on H-terminated Si(001), holding (a) 0, (b) 1 and (c) 2 electrons, showing how the buckling of the dimer changes with the different DB charge states. The grey circles denote Si atoms, the black dots denote electrons in a dangling bond and the white circles denote H atoms.

bond by tunnelling electrons. Once an H atom is removed, its Si host atom has only formed three bonds, resulting in a dangling bond being attached to the Si atom.

DBs on H-terminated Si(001) have been commonly used as adsorption sites for the deposition of a number of species including metal atoms, non-metals e.g. phosphorus [60] and organic molecules [61]. This patterning is possible because the DBs, which appear bright in STM imaging, have a high reactivity, specifically in comparison to the passivated background surface. DB wires have been suggested as possible candidates for interconnects in atomic-scale circuits because they have been found to have almost metallic characteristics [19].

2.3.2 Defect-induced Band Bending

A charged point defect on the surface, or sub-surface, of a semiconductor can induce localised band bending in a similar fashion to tip-induced band bending (TIBB, Section 2.1.4) [62]. A charged defect, much like a charged STM tip, has an electrostatic interaction with the free charge carriers in the semiconductor; the Coulomb potential of the charged defect is screened by carriers of opposite charge. This screened Coulomb potential results in a local changing of the semiconductor band energies and can be imaged by STM. The defect may lie on the surface or in the bulk of the semiconductor and hold a fixed charge, whereas the tip is external and of greater charge.

A result of this defect-induced band bending (DIBB) is that the appearance of a charged defect varies in bias-dependent STM imaging, particularly when the bias polarity is switched. The DIBB alters the number of sample states that electrons tunnel into (empty-state imaging) or out of (filled-state imaging), thus altering the tunnel current, and this determines the appearance of the defect. Bias-dependent imaging, along with DIBB, is commonly exploited to find out the charge of a defect.

For example, if a defect is negatively charged giving upward DIBB, in empty-state imaging, this will increase the already present upward TIBB, reducing the window of resonant states to tunnel into and appearing as a dark depression. In the filled-states, the DIBB will decrease the downward TIBB, appearing as a bright protrusion. This effect is illustrated in Figure 2.13. If the defect was positive it

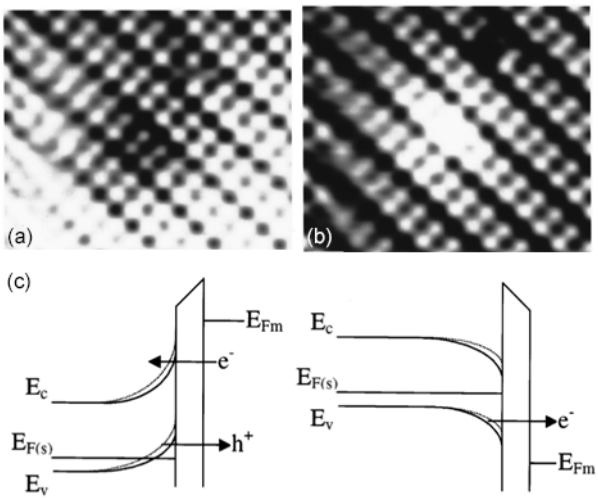

Figure 2.13: (a) Empty-state (2 V) and (b) Filled-state (-2 V) STM image of negatively charged, sub-surface B acceptor in H-terminated Si(100) (other image settings are 50 pA and 5×5 nm^2). (c) Accompanying energy level diagrams where the dotted lines represent the additional upward DIBB. Figure reproduced from Reference [8].

would have the opposite appearance, protrusion in empty-states and depression in filled-states. The DIBB does not vary between n- and p-type samples.

2.3.2.1 Imaging of Neutral Defects

There have been many reports in the literature that demonstrate how charged, ionised dopants appear as symmetric, circular protrusions or depressions [8, 63], but some dopants have been observed with broad, asymmetric appearances, of which two examples are included in Figure 2.14. Initially this asymmetry was interpreted as Friedel oscillations, with electrons backscattering from the semiconductor-vacuum interface [64, 65]. It has since been realised that what is being imaged is the wavefunction of the neutral dopant being projected onto the surface [9, 10]. The size and span of the asymmetric feature has been used to determine the depth of the sub-surface dopant and which layer of the substrate it is located in.

In this thesis, new data is presented for localised deep centre defects and the long range effects of the defects' charge, and for 2D materials and the CDW states around charged defects, but, maps of neutral dopant states, such as those in Figure 2.14, are not reported.

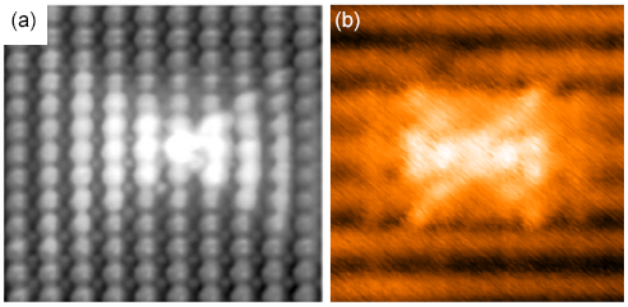

Figure 2.14: (a) 0.6 V STM image of a neutral, sub-surface Mn acceptor in GaAs(110). Image is 5.6×5.0 nm^2 in size and reproduced from Reference [9]. (b) -1.2 V STM image of a neutral, sub-surface As donor in H-terminated Si(001). Image is 5.0×5.0 nm^2 in size and reproduced from Reference [10].

2.4 Molybdenum Disulfide & Other Transition Metal Dichalcogenides

Transition metal dichalcogenides (TMDs) are a group of layered materials whose chemical formulae have the form MX_2, where M is a transition metal and X is a chalcogen. They have strong intra-layer, in-plane covalent bonding, but weak interlayer, out-of-plane van der Waals bonding. Each quasi-two-dimensional layer consists of three sub-layers: a hexagonal layer of transition metal atoms sandwiched between two hexagonal layers of chalcogen atoms. Schematic diagrams of TMD layers are on show in Figure 2.15. Molybdenum Disulfide (MoS_2) is a famous example of a TMD.

TMDs can be of semiconducting, semi-metallic, or metallic nature and they come in a number of polytypes, which have a different number of layers in the unit cell with different stacking orders. The three main polytype varieties are on view in Figure 2.15. Both factors, electronic behaviour and polytype, depend on which group of the Periodic Table the transition metal belongs to i.e. its *d* orbital filling, as summarised in Table 2.1. Group VI elements make semiconducting TMDs because their *d* orbitals are half-filled.

The coordination refers to the arrangement of chalcogen atoms around the transition metal atom [11]. If the metal atom has octahedral coordination, the polytype has tetragonal symmetry and the unit cell features one layer — 1*T* (Fig. 2.15 (a)). If

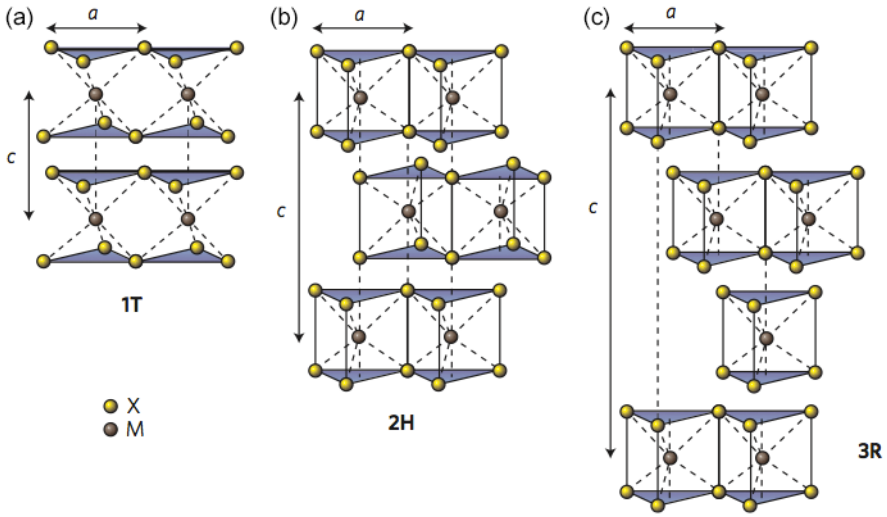

Figure 2.15: The three main polytypes of TMDs, (a) 1*T*, (b) 2*H*, and (c) 3*R*, see main text for more details. *a* is the lattice constant and *c* is the height of a unit cell. Figure reproduced from Reference [11].

the metal atom has trigonal prismatic coordination, the polytype has hexagonal symmetry and the unit cell features two layers — 2*H* (Fig. 2.15 (b)). If the metal atom has trigonal prismatic coordination, the polytype may have rhombohedral symmetry and in this case the unit cell features three layers — 3*R* (Fig. 2.15 (c)).

Group	Transition metal	Polytype	Electronic behaviour
IV	Ti	1*T*	Semi-metal
V	Nb, Ta	2*H*	Metal
VI	Mo, W	2*H*	Semiconductor

Table 2.1: Summary of the transition metals that can form TMDs, and the resulting structural and electronic properties of the TMD. The chalcogen is typically either S, Se or Te.

Metallic TMDs have demonstrated exotic many-body phases, including charge density waves and superconductivity. Conflicting explanations have been put forward for their origins and the transformation between phases. These explanations will be discussed later in the literature review (Section 3.4.2). A charge density wave (CDW) is a correlated electronic ground state, where energy is saved by breaking symmetry and the appearance of an energy gap at the Fermi energy. The resulting lattice deformation is accompanied by a periodic charge density modulation,

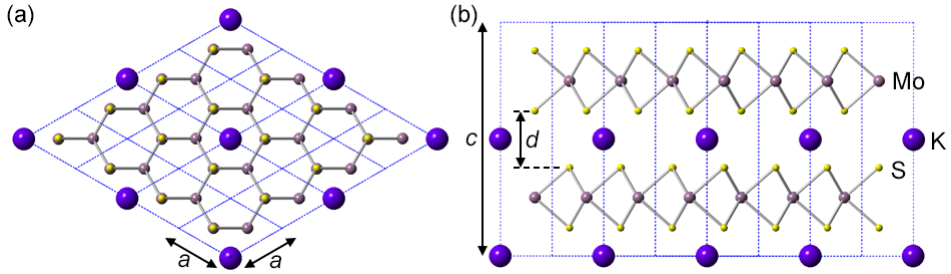

Figure 2.16: (a) Top view and (b) side view, displaying the structure, of the K-intercalated $2H$-MoS_2 sample ($K_{0.25}MoS_2$) used in the experiments of this thesis. The Mo, S and K atoms are indicated. The blue dashed lines depict the unit cell, for which $a = b = 0.322$ nm and $c = 1.637$ nm [12]. Diagram was created using crystal structure data from [13]. If the MoS_2 sample was not intercalated then $a = 0.316$ nm and $c = 1.230$ nm [13]. These distances consider the sample to be held at room temperature, but at low temperatures, say 5 K, a and c would decrease by very small amounts: approximately 0.5 pm and 17.2 pm, respectively [14].

due to the coupling between electrons and phonons [66].

The electronic structures of semiconducting TMDs, like MoS_2, have been controlled and modified; more charge carriers have been introduced by the use of electrostatic gating effects [67] and chemical doping methods [3, 4]. Both techniques have been shown to introduce superconductivity. Since the seventies, MoS_2 has been chemically doped by intercalating alkali metal atoms into the van der Waals gap between the TMD layers, using the liquid ammonia procedure, see Figure 2.16. K, Rb and Cs have been intercalated into crystals of MoS_2, phasing in superconductivity below a critical temperature of 6.9 K [4].

The Nobel Prize winning isolation of graphene, a material which has great strength and exceptional electronic properties, by K. S. Novoselov and A. K. Geim [68] has sparked an interest in other low-dimensional and atomically thin materials. This has led to a resurgence in TMD research, where single layers can be extracted by mechanical exfoliation from bulk crystals, akin to the preparation of graphene from graphite, where the weak, short-range interlayer bonding is easily overcome [69].

Semiconducting TMDs are of particular interest because, unlike graphene, their band gap allows for use in devices e.g. transistors. In single-layer form, many semiconducting TMDs, such as MoS_2, transform from having an indirect

band gap to a larger, direct band gap, with an energy falling within the visible range (read Section 3.4.1). Along with other interesting electrical properties, this aspect makes these 2D semiconducting TMDs an option for future nano-electronic and nano-opto-electronic devices [11].

2.5 Reciprocal lattice

The reciprocal lattice is the Fourier transform of the real or direct lattice of a crystal structure. If there are any periodicities in the spatial wavefunction of the direct lattice, they are represented in the reciprocal lattice by a spot at the corresponding wavevector. By inverse Fourier transforming the reciprocal lattice, one is able to re-obtain the direct lattice.

If we consider the direct lattice to be a Bravais lattice, which is usually the case, it can be described by a discrete set of vectors $\mathbf{R}$, and if we take a plane wave $e^{i\mathbf{K}\cdot\mathbf{r}}$ to have the same periodicity as the lattice, then the following is true [70]:

$$e^{i\mathbf{K}\cdot(\mathbf{r}+\mathbf{R})} = e^{i\mathbf{K}\cdot\mathbf{r}} \tag{2.37}$$

$$e^{i\mathbf{K}\cdot\mathbf{r}}e^{i\mathbf{K}\cdot\mathbf{R}} = e^{i\mathbf{K}\cdot\mathbf{r}} \tag{2.38}$$

$$\therefore e^{i\mathbf{K}\cdot\mathbf{R}} = 1. \tag{2.39}$$

So the reciprocal lattice is also a Bravais lattice, defined by a set of vectors $\mathbf{K}$ that satisfy equation 2.39.

The reciprocal lattice is used to investigate crystal periodicities, by way of measuring the wavevector in reciprocal space one can more accurately determine the lattice constant in real space.

2.5.1 Fourier transform STM

The Fast Fourier Transformation (FFT) of an STM image converts the image from a basis of real space to a basis of reciprocal space, outputting a series of spots representing the discrete wavevectors that constitute the periodicities of the image.

In the FFT, the spots are symmetric about a bright, central spot, which is an average of all the constituent sine functions and is used as the zero point when

measuring the distances to the spots. The FFT maps the real space lattice to reciprocal space, hence lines in the real space image are represented by spots in the FFT. Spots that are closer to the centre, have a smaller wavevector corresponding to larger wavelength periodicities in real space, following $k = \frac{2\pi}{\lambda}$, where k is the wavevector and λ is the wavelength. The brighter the spot, greater magnitude, the more the sine wave of the spot's wavevector contributes to the image.

Here, the FFT analysis technique is used to reveal regular ordering in the STM images, and to accurately measure the wavevector, and hence lattice constants, of the periodic structures of real space images. In general, this FFT technique gives more accurate results than measuring the lattice constants directly from the real space images. An example of its use is featured in Figure 2.18, which will be explained in more detail below.

If an STM image has the dimensions $L \times L$ and $N \times N$, where L is the length in nanometres and N is the number of pixels per line, then the distance between successive, horizontal or vertical, pixels l is

$$l = \frac{L}{N}.$$

The equivalent for the Fourier transform (FT) of the image, L_{FT} and l_{FT}, is then given by,

$$L_{FT} = \frac{1}{l} = \frac{N}{L} \text{ and } l_{FT} = \frac{1}{L}.$$

L_{FT} and l_{FT} have units of reciprocal length, units of inverse nanometres (nm^{-1}) if L and l were given in nanometres. Therefore, optimal Fourier transforms are produced by aiming for larger scan areas, to give a higher resolution FT, with a greater number of data points and a larger area FT.

2.5.2 Si(001) surface

The Si(001) surface has a $c(4 \times 2)$ surface reconstruction, as shown in Figure 2.17, for which the primitive lattice vectors that define the unit cell are as follows:

$$\mathbf{a_1} = 2a\hat{\mathbf{i}} + a\hat{\mathbf{j}},$$

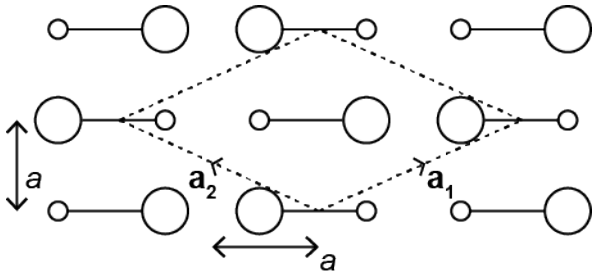

Figure 2.17: Top view of the Si(001)-$c(4\times2)$ surface, with the unit cell, containing one dimer, and definitive primitive lattice vectors $\mathbf{a_1}, \mathbf{a_2}$ highlighted. The lattice constant is a. Small circles denote down Si atoms and large circles denote up Si atoms in this buckled dimer formation.

$$\mathbf{a_2} = -2a\hat{\mathbf{i}} + a\hat{\mathbf{j}},$$

$$\mathbf{a_3} = \hat{\mathbf{k}}.$$

The lattice vector for any point on the surface can be written in terms of these primitive vectors, as a linear sum.

The corresponding primitive vectors of the reciprocal lattice are determined using the equations [70]:

$$\mathbf{b_1} = \frac{\mathbf{a_2}\times\mathbf{a_3}}{\mathbf{a_1}\cdot(\mathbf{a_2}\times\mathbf{a_3})}, \tag{2.40}$$

$$\mathbf{b_2} = \frac{\mathbf{a_3}\times\mathbf{a_1}}{\mathbf{a_2}\cdot(\mathbf{a_3}\times\mathbf{a_1})}, \tag{2.41}$$

$$\mathbf{b_3} = \frac{\mathbf{a_1}\times\mathbf{a_2}}{\mathbf{a_3}\cdot(\mathbf{a_1}\times\mathbf{a_2})}. \tag{2.42}$$

A factor of 2π has been omitted from these equations. This is possible by rewriting equation 2.39 as

$$e^{2\pi i\mathbf{K}\cdot\mathbf{R}} = 1. \tag{2.43}$$

This definition is commonly used in crystallography.

Using equation 2.40 gives,

$$\mathbf{b_1} = \frac{1}{4a}\hat{\mathbf{i}} + \frac{1}{2a}\hat{\mathbf{j}},$$

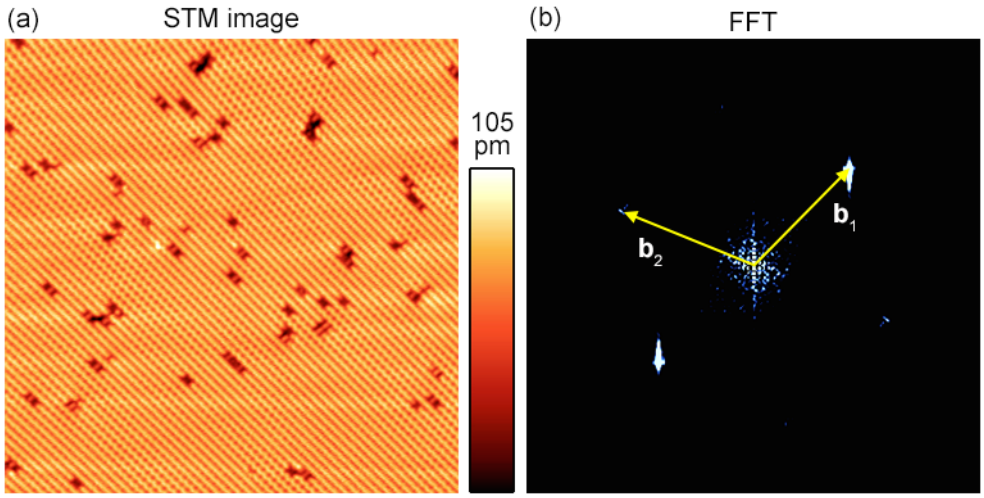

Figure 2.18: (a) STM image of Si(001) (settings: -1.6 V, 50 pA, 40×40 nm^2, and 77 K). The dark defects on the surface are Si dimer vacancies. (b) Fourier transform of the image in (a) reveals a rectangular lattice, as anticipated for the $c(4 \times 2)$ surface reconstruction, and the spots have a wavevector of 1.542 nm^{-1}. This corresponds to a real space lattice constant of 0.363 nm, determined using Equation 2.44, close to the expected value of 0.383 nm.

and, similarly, equation 2.41 gives,

$$\mathbf{b_2} = -\frac{1}{4a}\hat{\mathbf{i}} + \frac{1}{2a}\hat{\mathbf{j}}.$$

The magnitude b of the primitive vectors of the reciprocal lattice gives a relationship between the wavevector in reciprocal space, b in this case, and the lattice constant a.

$$b = |\mathbf{b_1}| = |\mathbf{b_2}| = \frac{\sqrt{5}}{4a} \tag{2.44}$$

The lattice constant for Si(001) is 0.383 nm, therefore $b = 1.460\text{nm}^{-1}$ and it is expressed in units of reciprocal length. This relationship was used to experimentally determine the lattice constant from the Fourier transform of the STM image in Figure 2.18.

2.5.3 Simple hexagonal lattice

Figure 2.19 is a schematic of a simple hexagonal lattice and the primitive vectors of this direct lattice are as follows,

$$\mathbf{a_1} = a\hat{\mathbf{i}},$$

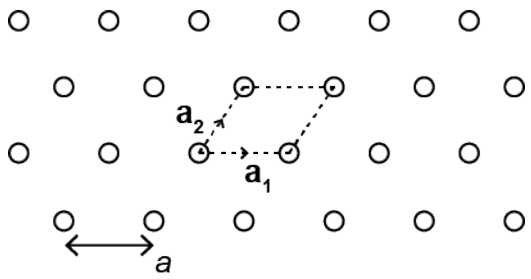

Figure 2.19: Schematic of a simple hexagonal lattice, depicting its defining unit cell and the primitive lattice vectors $\mathbf{a_1}, \mathbf{a_2}$. The lattice constant is a.

$$\mathbf{a_2} = \frac{1}{2}a\hat{\mathbf{i}} + \frac{\sqrt{3}}{2}a\hat{\mathbf{j}},$$

$$\mathbf{a_3} = \hat{\mathbf{k}}.$$

From this, and with the use of equation 2.40, we can determine the primitve vector of the reciprocal lattice and thus a relationship between the wavevector in reciprocal space and the lattice constant.

$$\mathbf{b_1} = \frac{1}{a}\hat{\mathbf{i}} - \frac{1}{\sqrt{3}a}\hat{\mathbf{j}} \tag{2.45}$$

$$b = |\mathbf{b_1}| = \frac{2}{\sqrt{3}a} \tag{2.46}$$

By definition, see equations 2.40, 2.41 and 2.42, each reciprocal primitive vector is orthogonal to two real primitive vectors due to the cross product included in the numerator. This leads to the following identity [70]:

$$\mathbf{b_i}.\mathbf{a_j} = \delta_{ij} = \begin{cases} 0 & \text{if } i \neq j, \\ 1 & \text{if } i = j. \end{cases}$$

Another way of looking at this, is that the vector for any point in the direct lattice $\mathbf{R}$ can be written in terms of the primitive vectors $\mathbf{a_1}, \mathbf{a_2}, \mathbf{a_3}$ and the vector for any point in the reciprocal lattice $\mathbf{K}$ can be written in terms of the primitive vectors $\mathbf{b_1}, \mathbf{b_2}, \mathbf{b_3}$. Therefore, for equation 2.43 to be true then $\mathbf{K}(\mathbf{b_1}, \mathbf{b_2}, \mathbf{b_3}) \cdot \mathbf{R}(\mathbf{a_1}, \mathbf{a_2}, \mathbf{a_3})$ must be an integer.

The Kronecker delta function δ_{ij} can be used to give a different route to deter-

mine the reciprocal primitive vectors, as shown next. Using the same direct lattice vectors as before and assuming the reciprocal lattice vectors take the form:

$$\mathbf{b_1} = {b_1}^x\hat{\mathbf{i}} + {b_1}^y\hat{\mathbf{j}},$$

$$\mathbf{b_2} = {b_2}^x\hat{\mathbf{i}} + {b_2}^y\hat{\mathbf{j}}.$$

Then,

$$\begin{aligned}
\mathbf{b_1}.\mathbf{a_1} &= a{b_1}^x = 1 && \Rightarrow {b_1}^x = \tfrac{1}{a},\\
\mathbf{b_1}.\mathbf{a_2} &= \tfrac{1}{2}a{b_1}^x + \tfrac{\sqrt{3}}{2}a{b_1}^y = 0 && \Rightarrow {b_1}^y = \tfrac{2}{\sqrt{3}a}(-\tfrac{1}{2}a{b_1}^x) = -\tfrac{1}{\sqrt{3}a},\\
\mathbf{b_2}.\mathbf{a_1} &= a{b_2}^x = 0 && \Rightarrow {b_2}^x = 0,\\
\mathbf{b_2}.\mathbf{a_2} &= \tfrac{1}{2}a{b_2}^x + \tfrac{\sqrt{3}}{2}a{b_2}^y = 1 && \Rightarrow {b_2}^y = \tfrac{2}{\sqrt{3}a}(1 - \tfrac{1}{2}a{b_2}^x) = \tfrac{2}{\sqrt{3}a}
\end{aligned}.$$

$$\therefore \mathbf{b_1} = \frac{1}{a}\hat{\mathbf{i}} - \frac{1}{\sqrt{3}a}\hat{\mathbf{j}} \text{ and } \mathbf{b_2} = \frac{2}{\sqrt{3}a}\hat{\mathbf{j}}$$

And

$$b = |\mathbf{b_1}| = |\mathbf{b_2}| = \sqrt{\frac{4}{3a^2}} = \frac{2}{\sqrt{3}a}.$$

Giving an identical result to equations 2.45 and 2.46.

Chapter 3

Literature review

3.1 Dangling bonds on H-terminated Si(001)

3.1.1 Single, isolated DBs

Haider *et al.* have studied DBs on H-terminated Si(100) at room temperature [15]. In empty-state imaging of a low doped n-type sample ($\sim 10^{15}$ cm^{-3}), bright protrusions are observed (see Fig. 3.1 (a)) which they suggest are neutral DBs (DB^{0}s). For a sample with a higher doping ($\sim 10^{18}$ cm^{-3}), depressed regions, forming a halo, around a bright, central spot are found instead (see Fig. 3.1 (b)) which they claim are negatively charged DBs (DB$^-$s). DB$^-$ induces upward band bending, as described in Section 2.3.2, decreasing the tunnel current into the sample and to compensate the tip approaches the surface creating a depression [15, 16, 17].

The reason given for these observations is that a low doped n-type sample has a lower Fermi level so the DB is only singly occupied, but with a higher doping and a higher Fermi level, the DB can be doubly occupied. Such small changes in the Fermi level are unlikely to support such changes in the DB occupation especially since it is known the DB states are deeper in the band gap [16]. This explanation was thus later modified by Livadaru *et al.*, in Ref. [16], to take the scanning tip into account, and explaining how TIBB can control the DB occupation.

The transport of electrons through DBs, particularly during empty-state STM imaging, has been discussed by Livadaru *et al.* [16]. The presence of a biased tip results in TIBB at the sample surface and in the case of empty-state imaging, the

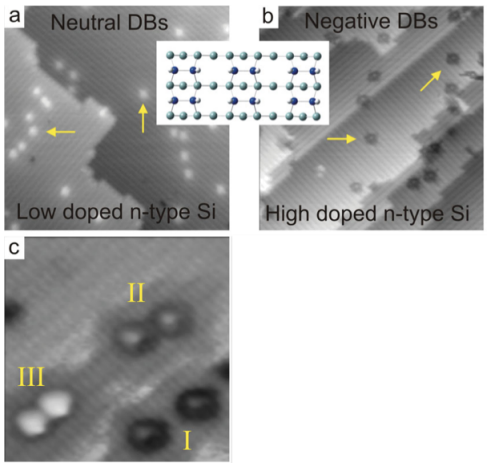

Figure 3.1: (a) STM image, 35 nm × 35 nm, 2 V, 0.1 nA. (b) Same as (a) except bias is 2.2 V. (c) STM image, 9 nm × 9 nm, 2 V, 0.2 nA. Three DB pairs separated by (I) 2.32 nm, (II) 1.56 nm, and (III) 1.15 nm. Pair (I) is not coupled, pair (III) is coupled, and pair (II) is in an intermediate stage. Inset is a schematic of the Si(100):H surface. Figure reproduced from Ref. [15].

electron bands are bent upwards leading to depletion and the formation of a space charge region at the surface, see Figs. 3.2 (b) and 3.4 (c). TIBB is a long range effect, acting laterally so the surface is depleted of electrons and more intrinsic compared to the bulk. Whereas, in filled-state imaging, see Fig. 3.2 (a), downward BB occurs and the DB remains below the Fermi level, and there is an excess of electrons, leaving the DBs completely filled (negative charge state) [2].

Electrons from the tip tunnel into the DB, across the barrier due to the vacuum gap, and electrons from the DB tunnel into the Si sample across the barrier due to the

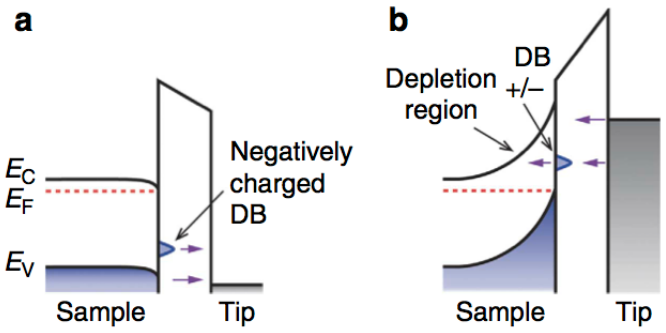

Figure 3.2: Energy level diagrams corresponding to (a) filled-state and (b) empty-state STM imaging of a single DB. In the filled-states, the DB is negatively charged and in the empty-states, the DB can be positive or negative — refer to main text for explanation. Figure reproduced from Ref. [2].

space charge region. This tip-DB-Si junction, or 'double barrier tunnel junction', is reminiscent of a single electron transistor (SET), where the DB is the island, the tip is the source, and the Si is the drain. When the rate of electrons tunnelling into the DB and the rate of electrons tunnelling out are equal the DB is in a steady state, although in a double barrier tunnel junction the two barriers will most likely differ. The surface barrier can be greater than the vacuum barrier, so that the tunnel rate in would be greater than the tunnel rate out resulting in non-equilibrium charging of the DB. Therefore the DB can become doubly occupied and negatively charged even though it is above the Fermi level.

As the tip laterally approaches the DB during a scan, the magnitude of the upward band bending increases. So that in the period between the DB state being raised above the Fermi level to when it becomes negatively charged, i.e. the point where the surface barrier becomes greater than the vacuum barrier, the DB is positive. This is observed as enhancement disc in the imaging with a halo or depression at the centre [2], as displayed in Fig. 3.3 (b, d). Whereas in filled-states imaging, Fig. 3.3 (a, c), a DB is a small, bright protrusion with a slight, decaying enhancement — further evidence it is negatively charged.

DB^-s are observed as these halo features in empty-state imaging, in agreement with the work by Haider *et al.*. The shape of this halo is a reflection of the tip shape [16, 17].

Livadaru states there are two methods for electrons to travel between the tip and a DB: tunnelling from tip to DB (see Fig. 3.4 (3)); and tunnelling from tip to Si, in region close to DB, and subsequent capture by DB (Fig. 3.4 (1 & 2)). There are several methods for electron transportation from DB to Si, they include: thermal excitation to conduction band (CB) (Fig. 3.4 (5)); elastic tunnelling to a CB state, resonant to DB state, across surface barrier (Fig. 3.4 (4)); and recombination with a hole captured by the DB which depends on the density of holes near the DB (Fig. 3.4 (6)). The amount of band bending at the surface determines the hole concentration, for example, inversion results in a large number of holes. Here TIBB is making the surface intrinsic-like, so the process of DB electrons recombining with

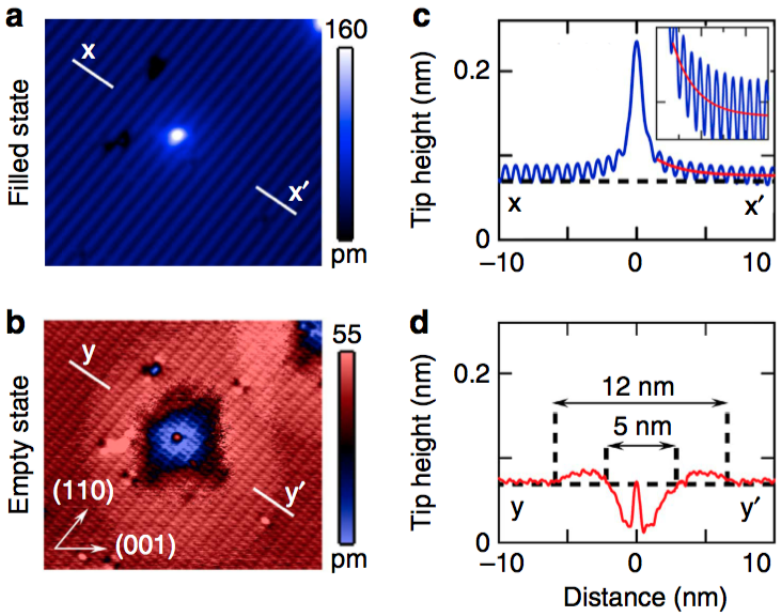

Figure 3.3: (a) Filled-state (-1.7 V, 25 pA) and (b) Empty-state (1.7 V, 25 pA) STM images of a single DB. Images are 16 nm × 14 nm in size and were taken at 77 K. (c, d) Associated line profiles, taken at positions indicated by white markers on the images. Figure reproduced from Ref. [2].

holes is unlikely to occur. The thermal emission of electrons is the main method by which DBs lose charge but at lower temperatures this is negligible. Therefore, the main discharge route becomes tunnelling from DB to CB [17].

Taucer *et al.* [17] have shown in their spectroscopy that a DB can display Coulomb blockade behaviour at low temperatures. The characteristic Coulomb staircase is observed, where the steps represent the addition of a single electron to the DB, as it overcomes the charging energy, allowing it to go through its quantised charge states from being positive to neutral to negative. Charge repulsion ensures only one electron tunnels at a time. This is somewhat expected because, as mentioned earlier, the DB is small enough to be the island of this SET-like junction. At liquid helium temperatures of 4.4 K, bias-dependent imaging of DBs displays similar charging effects, however unexpected noise could repeatedly be seen at the edge of the halos. Taking a telegraph signal, a measurement of current with time, at this position, with the height (feedback loop off) and bias fixed, showed that the current had a preference for three particular values which represent the three DB charge states. Fig. 3.5 shows the different charge states induce differing band

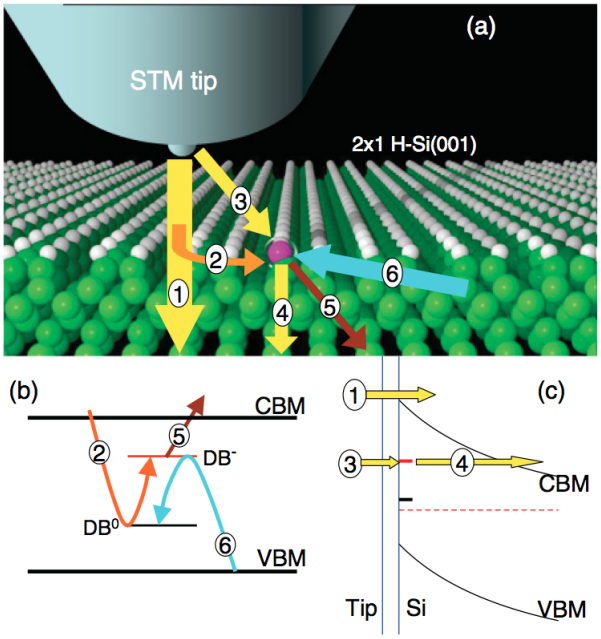

Figure 3.4: (a) Schematic of a single DB on Si(001):H being imaged with an STM. (b) Diagram of Si band gap. (c) Energy level diagram displaying TIBB in empty-state imaging. The numbers 1 to 3 represent the methods of electron transport from tip to DB and the numbers 4 to 6 highlight the carrier transport modes between DB and bulk Si. Refer to main text for more details. Figure reproduced from Ref. [16].

bending and thereby different currents; during empty-state imaging DB^+ induces a larger current, imaged as an enhancement, and DB^- decreases the tunnel current and the surface appears depressed. At room temperature, the rate at which electrons are loaded to and unloaded from the DB are too fast for the pre-amplifier of the STM, which as a result cannot distinguish between the different charge states and no noise is seen in the imaging.

3.1.2 Pairs of interacting DBs

3.1.2.1 Tunnel-coupling

Haider *et al.* have theoretically modelled DBs in order to explain a tunnel-coupling effect between pairs of DBs [15]. This effect is observed experimentally when two DBs are created within 1.5 nm of each other (see Fig. 3.1 (c)).

To model such a pair of DB^-s, two isolated potential wells are brought closer together, but it is said that the electrostatic repulsion between them renders the

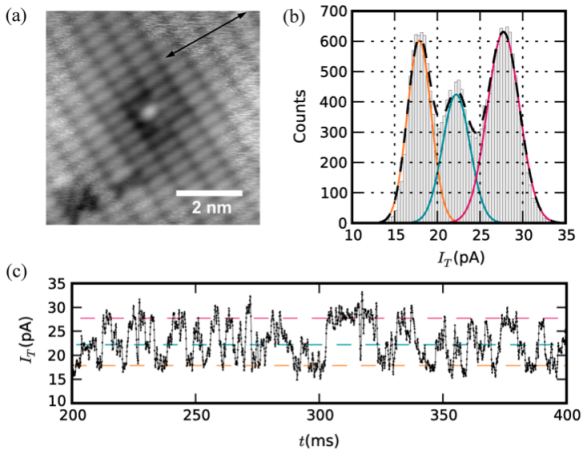

Figure 3.5: (a) STM image of single DB, 1.4 V, 20 pA. (b) Histogram of tunnel currents measured during telegraph signal measurement (tip positioned 3.14 nm from the DB). The peak at lowest current is due to DB^- charge state, the middle peak is DB^0, and the higher current peak is DB^+. (c) One of the telegraph signals taken. Figure reproduced from Ref. [17].

system unstable and so to relax, one electron, from the total of four, is lost to the conduction band. Once one of the DBs has lost an electron, a space opens up for an electron from the other DB to tunnel into, so the two DBs become 'tunnel-coupled', as in one electron can tunnel between the two. This is similar to when an electron is shared between two quantum dots. This is the first reported observation of such a coupling effect between pairs of DBs.

The DBs which were previously halos now appear brighter with a dark halo now containing the whole pair. The presence of the surrounding depression is a sign that the pair still remains negatively charged overall, because each DB still hosts one electron making each DB neutral but the additional electron shared between the pair gives the overall negative charge. However the DBs are brighter, like the DB^0 state, as the DB pair now has one less electron and so the amount of induced upward BB has decreased allowing for a larger tunnel current.

The position of the tunnelling electron can be controlled by introducing an asymmetry to the structure and by using electrostatic repulsion, Fig. 3.6. It has been shown that when a third DB, in the DB^- state, is created near a DB pair but not close enough for itself to couple with the pair, then the tunnelling electron will have a preference to sit on the DB site furthest away.

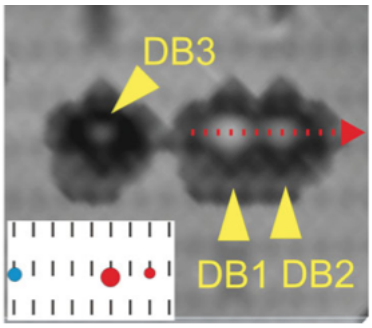

Figure 3.6: STM image (2.5 V, 100 pA, 5 nm × 5 nm) showing electrostatic influence of third DB on a tunnel-coupled DB pair. Inset is a schematic displaying DB positions. Figure reproduced from Ref. [15].

Although, we offer a different interpretation to explain the interactions between DBs.

3.1.2.2 Excited molecular state

Schofield *et al.* [2] have shown pairs of DBs, separated by distances ranging from 0.5 nm to 1.2 nm, to interact. A third, larger, and brighter protrusion has been observed to appear between the two DBs in empty-state STM imaging, Fig. 3.7, under certain tunnelling conditions.

Figure. 3.8 shows how, to explain these observations, each DB was modelled with a Pöschl-Teller potential well, with two bound states: a ground state above the valence band, and an excited state below the conduction band. Thus, two wells were required to model a DB pair, set apart by a distance equal to the DB pair separation. When the two wells overlap and interact, the ground and excited states both split, but the highest energy splitting is unbound, i.e. it lies in the conduction band. The

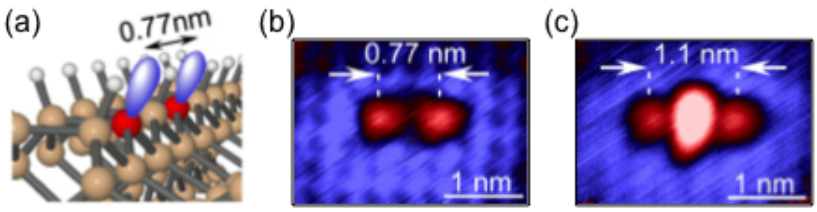

Figure 3.7: (a) Schematic of a pair of DBs on next-nearest neighbour sites. (b) Empty-state STM image of such a pair of DBs (2 V, 95 pA). (c) Low current empty-state image of the same DB pair (2 V, 5 pA), reveals a large, bright protrusion between the DBs. Figure reproduced from Ref. [2].

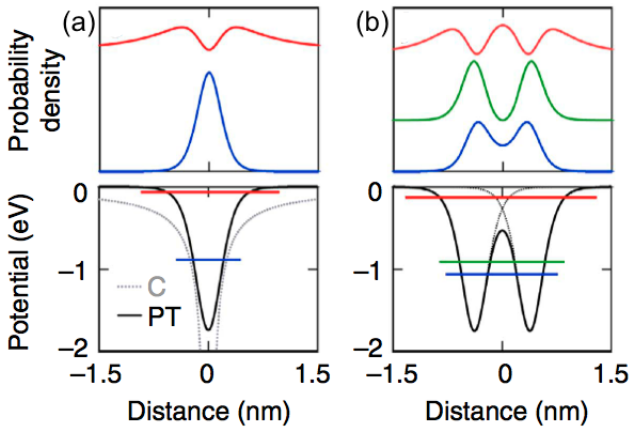

Figure 3.8: Probability densities of the bound states held by a single (a) and two overlapping (b) DB potential wells. Each DB is represented by a Pöschl-Teller potential, PT, which fits within a Coulomb potential, C. The two wells in the double well system are separated by 0.77 nm in order to represent a pair of DBs on next-nearest neighbour positions. Figure reproduced from Ref. [2].

highest energy bound state of the three has a central maximum in the probability density, this is what is observed in empty-state imaging and it is referred to as an excited molecular orbital state.

In empty-state imaging, the excited molecular state can only be observed when it is aligned with or brought below the Fermi level of the tip because the electron tunnelling, or tunnelling matrix element, is localised about this point. This alignment is achievable using the sample bias and tunnelling current parameters as gates, in particular under a high bias or a low current setting, see the energy level diagrams in Fig. 3.9. Increasing the bias raises the tip Fermi level to the excited molecular state energy, or decreasing the current, increases the tip-sample separation and in turn reduces the upward band bending, pulling the excited molecular state down to equate to the tip Fermi level.

3.1.3 DB wires

Hitosugi *et al.* [18] have investigated DB wires on H-terminated, n-type Si(100) at liquid nitrogen temperatures between 96 and 110 K. DB wires, from 2 to 15 DBs long, were created by moving the tip at a speed of 5 nm/s along a dimer row with high sample bias and tunnelling current settings, typically 2.8 V and 0.9 nA. The DB wire is subsequently imaged off the dimer row centre since it is only a single

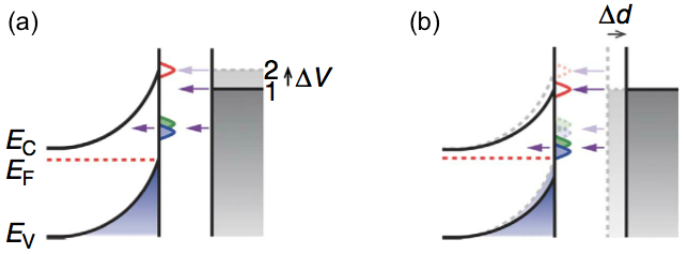

Figure 3.9: Energy level diagrams for empty-state imaging of a DB pair, whose three bound states are displayed. The tip Fermi level can be made to align with the excited molecular orbital state of the pair (red) by either (a) increasing the bias, from position 1 to 2, or (b) decreasing the tunnelling current, which increases the tip-sample separation. Figure reproduced from Ref. [2].

DB wide. The DBs formed are about 0.1 nm higher than the passivated background surface, but all the DBs do not have the same height. Unexpectedly they form an alternating pattern of bright and dim, i.e. up and down, DBs. The authors explain this surprising result using Jahn-Teller distortions.

Usually one expects the symmetric configuration to be the most stable, in this case a wire of even height DBs. However, a greater total energy reduction is sometimes achieved by the redistribution of charge; two such examples are Jahn-Teller distortion in molecules and Peierls distortion in one-dimensional metals. To create this alternating pattern, the height of the first layer Si atoms changes, alternating from high to low, due to charge redistribution or Jahn-Teller distortions, while the second layer Si atoms are displaced laterally, much like a Peierls lattice distortion, alternating from left to right displacements so the atoms pair up. Peierls distortions consist of a periodic lattice distortion and a resulting periodic charge redistribution.

These results are summarised in Fig. 3.10. In a DB wire, charge is transferred from down DBs to neighbouring up DBs and the height difference between the up and down DBs is between 0.01 and 0.02 nm. A down DB is a p-like orbital and its Si host atom forms sp^2-like bonds with its neighbours, while an up DB is an s-like orbital and its host Si atom forms p^3-like bonds. If a DB in a wire is imaged as a protrusion (or up) in the filled-states then it will appear down in the empty-states, so the alternating pattern changes from up-down-up to down-up-down (see Fig. 3.10 (b)).

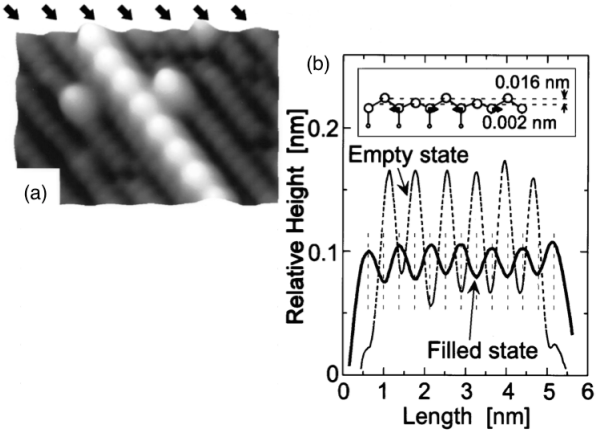

Figure 3.10: (a) 3D rendered STM image of a wire of single DBs on Si(100):H, 96 K, 7 nm $\times$ 4 nm. (b) Line profiles of a 13 DB wire in empty-states (2 V) and filled-states (-2 V). Inset shows predicted atom displacements for a DB wire. Figure reproduced from Ref. [18].

In the filled-states, the edge DBs, the first and last DBs of the wire, are always up and this 'edge effect' is responsible for making the DB wire more stable, with respect to temperature. If there are an odd number of DBs in the wire, all second layer Si atoms involved pair up but with an even number of DBs, there is a lone second layer Si atom that does not have a partner. Thus, an even length DB wire has two possible configurations, as the lone second layer Si atom can be at either end of the wire, therefore the wire is constantly flipping between the two configurations. Even a two DB wire will undergo a charge redistribution, essentially like a Si dimer, but when imaged both DBs appear to have the same height because of repeated switching between the two possible buckled structures; up-down and down-up, similar to when imaging clean Si(001) at room temperature.

Bird *et al.* [71] conducted a theoretical study of DB wires. The results produced show that finite length DB wires are Jahn-Teller distorted, thus agreeing with Ref. [18]. However, they concentrate on wires with an even number of DBs, since their Tight-Binding model does not work for odd length DB wires. This is due to their treatment of odd length wires as even length wires with an additional, height unadjusted DB.

Ye *et al.* [19] have created DB wires on p-type (B-doped) Si(100):H at room temperature. In contrast to the work by Hitosugi *et al.* [18] the DB wires were made

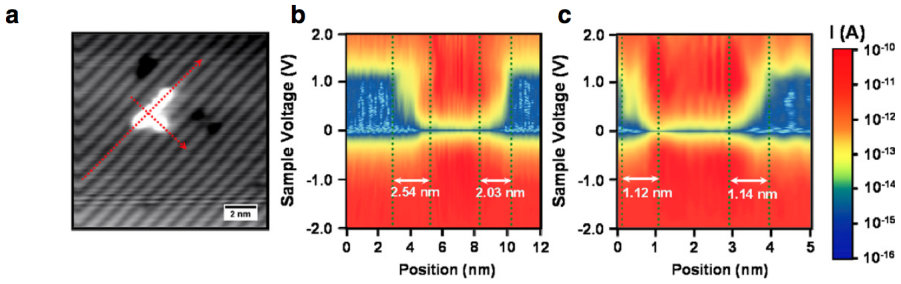

Figure 3.11: (a) STM image of a wire of single DBs along a dimer row, −2 V, 50 pA. Log IV spectra as a function of position for (b) along the dimer row and (c) across the dimer rows. Figure reproduced from Ref. [19].

step-by-step, in other words one DB at a time. Fig. 3.11 displays position dependent STS, a current-voltage (I-V) spectrum taken for every point or pixel along a line, of these DB wires. The spectroscopy for a DB wire, seven DBs long, displays metallic behaviour as there is no band gap in the I-V curves so the wire is essentially behaving like a one-dimensional metal.

The band gap does re-emerge in the spectroscopy after a distance of 2.54 nm along the dimer row and 1.14 nm across the dimer rows. The former distance is greater because in this direction the Si atoms are closer together and have stronger interactions compared to the direction across the dimer rows. These ‘decay’ lengths are in agreement with density functional theory calculations.

3.2 Electron confinement

3.2.1 One-dimension

Over the past two decades, much work has been done using the STM to create and arrange point defects in linear formations on surfaces. Constructing such one-dimensional architectures can provide electrostatic potential wells for the use of electron confinement. These atomic-scale quantum dots hold discrete, quantised bound states, the number of which typically depends on the length of the dot. By increasing the energy, or the sample bias setting, bound states with higher energies can be observed. This behaviour is reminiscent of standing waves on a string fixed at both ends.

Different systems exhibiting 1D electron confinement have been created by a

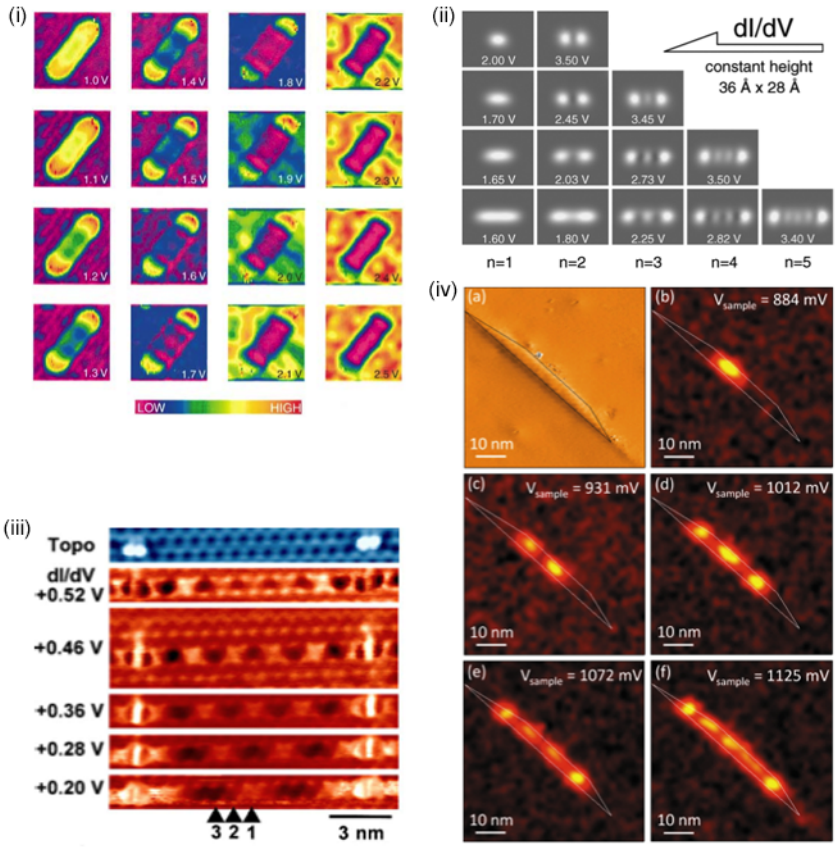

Figure 3.12: (i) Conductance maps of an 11 Au atom chain on NiAl(110), taken at increasing biases from 1.0 to 2.5 V. To reduce edge effects, each map is an average of a forward and backward scan. Figure reproduced from Ref. [20]. (ii) Conductance maps, regulated at 1 V and 1 nA, of Cu chains on Cu(111). The number on the right refers to the number of Cu atoms in the chain and n is the ordering of the states in increasing energy. Figure reproduced from Ref. [21]. (iii) Topography and conductance maps of the single Si(100) dimer row region confined between two W dot barriers. One of the maps is of a wider area for proof of its dimensionality. Figure reproduced from Ref. [22]. (iv) Topography and conductance maps of a parallelogram shaped InAsP quantum dot on InP. Figure reproduced from Ref. [23].

number of groups [20, 21, 22, 23]. Their results and findings are summarised in Fig. 3.12.

T. M. Wallis *et al.* created chains of Au atoms on NiAl(110) [20], see Fig. 3.12 (i), ranging in length from 2 to 20 atoms, by manipulating the position of each adsorbed Au atom. A single Au atom was found, using point spectroscopy, to have a state 2 eV above the Fermi energy. The combination of these individual states give the chain its electron density. S. Fölsch *et al.* fabricated chains of Cu

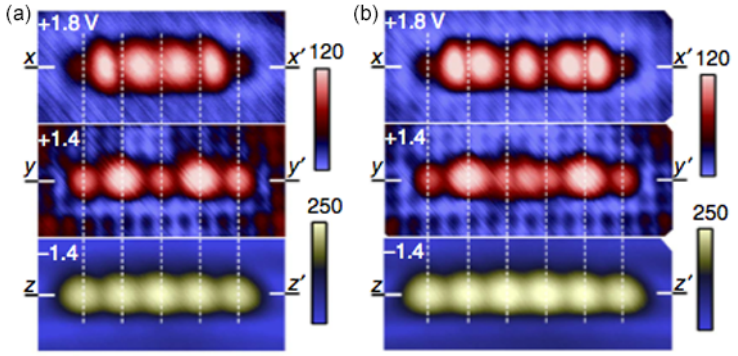

Figure 3.13: STM images of (a) a five DB chain, other image settings are 15 pA and 4.5×2 nm^2, and (b) a six DB chain, other settings are 15 pA and 5.3×2 nm^2, on Si(001):H. Figure reproduced from Ref. [2].

atoms on Cu(111) by atomic manipulation [21], see Fig. 3.12 (ii). The Cu adatoms were formed by poking the STM tip into the surface. Quantised electronic states appeared in the empty-states bias region, across the gap-like feature of the bare Cu surface, for the chains. An increasing number of states was found for longer length chains. K. Sagisaka and D. Fujita deposited two W dots along a single dimer row on Si(100) [22], by contacting the W tip with the surface, see Fig. 3.12 (iii). The dots had the width of the dimer row and in the region between them, surface state electrons were confined — leading to the quantisation of the $\pi^\star$ states. B. Fain *et al.* used cross-sectional STM and STS to study cleaved InAsP quantum dots on InP(001) [23], grown by chemical vapour deposition, see Fig. 3.12 (iv). These quantum dot have a parallelogram shaped appearance. The smaller dots behave like atoms, holding five discrete states appearing within the gap of the InP surface.

In contrast, the linear chains of DBs created, on next-nearest neighbour sites along a dimer row of H-terminated Si(001), by S. R. Schofield *et al.* [2], differ in the sense that each DB is considered to have its own potential well. The DB chain is therefore a series of overlapping wells where each individual bound state is split, the number of splittings corresponding to the number of constituent DBs. Resonances observed in STM imaging of these chains (Fig. 3.13) are an energy-weighted linear combination of these split states, with the image bias controlling the energy range of the involved states.

More recently, Fölsch *et al.* [24] have created quantum dots by arranging In^+

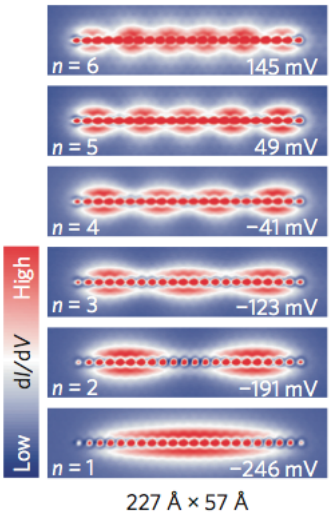

Figure 3.14: Conductance, or density of states, mapping of a 22 In adatom chain on InAs(111)*A* displays quantised states, for principal quantum numbers n from 1 to 6, as a sequence of resonances. Figure reproduced from Ref. [24].

ions into chains, varying in length from 6 to 25 adatoms, on an InAs(111)*A* surface. A small concentration of native In adatoms are already present. Each of these chains confine electrons of In surface states in 1D, not In adatom states, see Fig. 3.14. By making use of the (2×2) surface reconstruction, to accurately position In^{+} adatoms over the vacancy sites, it guarantees that chains of the same length will be identical quantum dots with the same properties.

3.2.2 Two-dimensions

The literature reviewed in the previous section on 1D electron confinement has all followed from the seminal paper on the quantum corral, by M. F. Crommie *et al.* [25], displayed in Fig. 3.15.

The positions of individual Fe adatoms on Cu(111) were manipulated, at a temperature of 4 K, to create a corral structure consisting of 48 Fe atoms. Electrons belonging to Cu surface states were confined to the circular area enclosed by the structure, in a 2D cylindrical potential well. Fe adatoms are capable of forming hard barriers because they strongly scatter surface electrons, and the interference between incident and reflected electrons results in standing waves as seen outside the corral. The peaks or resonances in the spectroscopy measurements signalled the quantisation of states, a lateral variation in the angular momentum was found as

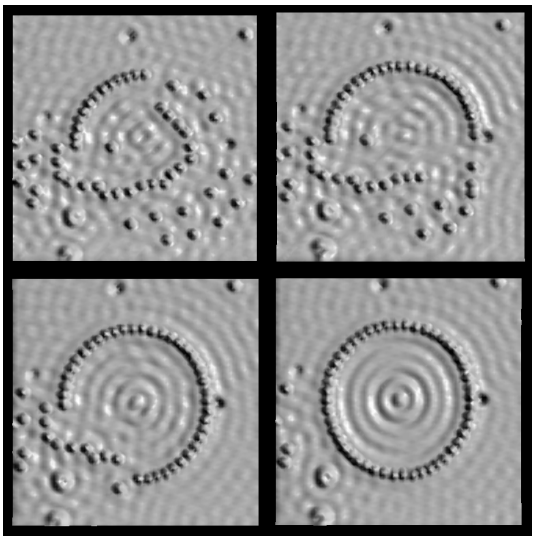

Figure 3.15: STM images showing the creation of the quantum corral: a ring of 48 Fe adatoms, radius 7.13 nm, on the Cu(111) surface, with the final image clearly showing the a periodicity in the electronic states within the corral. Image settings: 10 mV and 1 nA. Figure reproduced from Ref. [25].

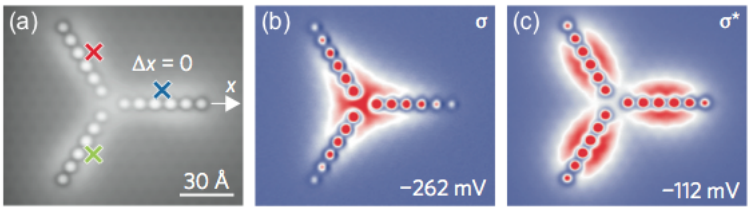

Figure 3.16: (a) STM image of three In chains, each is six adatoms long, arranged in a trimer-like formation (0.1 V, 100 pA, 5 K). Spectroscopy measurements taken exhibit a ground state (b) and an excited state (c) in the spatial density of state maps, in actual fact (c) is two degenerate excited states. Figure reproduced from Ref. [24].

well. This proved to be an experimental verification of the particle in a box, or in this case a circular area.

Moreover, Fölsch *et al.* have continued their work on chains of In adatoms on InAs(111)*A* to exhibit 2D electron confinement [24]. When two of these In chains or quantum dots are positioned close together, they couple and split the bound states into symmetric and anti-symmetric, or bonding and anti-bonding, combinations. Bringing the two chains closer together increases the splitting, as one would expect. Using three chains they are able to produce 2D-extended quantised states, see the triple quantum dot arrangement in Fig. 3.16. For this triple quantum dot, the degen-

eracy of the two excited states proves to be very strong, not affected by bringing an extra single In adatom close by, and only broken by introducing an asymmetry to the structure — for example, shifting the position of one of the chains.

3.3 Proximity effects in STM

In the way that Fölsch *et al.* studied the effects of varying the separation between two coupled atomic-scale quantum dots, how it influences the wavefunction overlap between the two, and the resulting energy splitting [24], other STM proximity effects have also been investigated and published. These results are summarised in this section. These experiments controllably change the local potential landscape by using the STM to rearrange atoms or molecules.

3.3.1 Controlling dangling bond charge states

J. L. Pitters, I. A. Dogel *et al.* [26] (Fig. 3.17) were able to control the charge state of DBs on the surface of H-terminated Si(100), via their proximity to titanium silicide ($TiSi_2$) nano-islands.

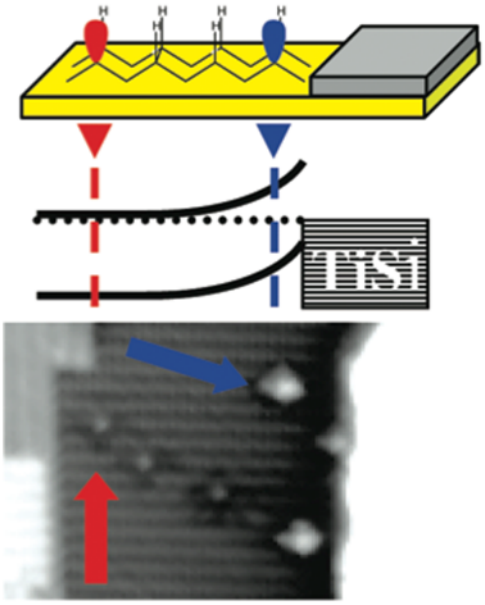

Figure 3.17: The upper part is a diagram illustrating the upward band bending induced by a $TiSi_2$ island on H-terminated Si(100). Below this is a room-temperature STM image, in line with the above diagram, where the red arrow signals a charged DB and the blue arrow an uncharged DB — the region close to the $TiSi_2$ is intrinsic-like. Figure reproduced from Ref. [26].

The nano-islands of $TiSi_2$ were created by depositing Ti on the Si(100) surface and heating to 900 °C, and after H termination, the islands remained. The $TiSi_2$ nano-islands act as metal contacts and this metal-semiconductor junction induces localised, upward band bending, and a depletion of electrons from the surface, evidenced by the surrounding depression in empty-state STM imaging. The H termination process passivates the surface states, unpinning the Fermi level and allowing band bending to occur.

On this surface, DBs were doubly occupied and negatively charged, appearing as point depressions, because the DB state or energy level is in the band gap and below the Fermi level of this highly doped n-type sample. But closer to the $TiSi_2$ contacts, within a distance of 40 nm, this was not the case. In this region, DBs were singly occupied and neutral in charge, appearing as a bright feature, since the greater upward band bending had lifted the DB state above the Fermi level of the sample. The band bending local to the $TiSi_2$ was verified by corresponding shifts in point spectra, the onset of the conduction band began at greater positive biases closer to the $TiSi_2$ islands.

3.3.2 Controlling hydrogen transfer in porphycene

T. Kumagai *et al.* [27] (Fig. 3.18) have controlled the rate of H transfer within the cavity of a porphycene molecule on the Cu(110) surface, by the precise positioning of a nearby single Cu adatom. These experiments were conducted at a temperature of 5 K.

There are four N atoms surrounding the cavity of porphycene and two H atoms. In STM imaging, only the *cis*-1 configuration of the molecule was found, appearing as a crescent- or sickle-shaped feature, with the long axis along the Cu(110) row direction. In this configuration, both the H atoms are on one side, either the left or right, of the cavity. Both *cis*-1 configurations were observed, which are mirror reflections of each other. DFT calculations agreed this is the energetically preferred arrangement of H atoms, because this way the two N atoms, without the H, align with the Cu(110) row below.

In low bias STM images, the molecule remained stable, but in high bias im-

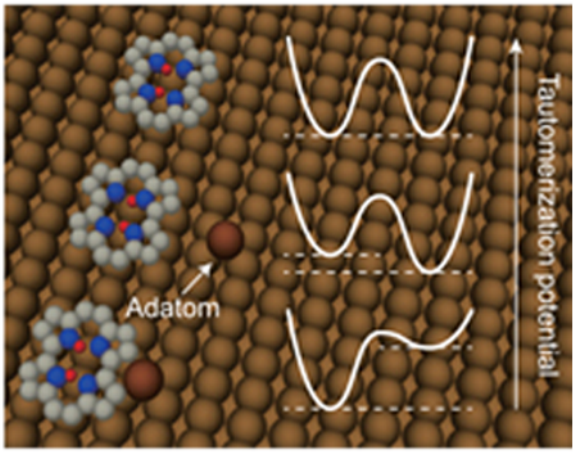

Figure 3.18: Each of the wells in the schematic potential energy graph represents a *cis* arrangement where the two H atoms either lie on the left or right of the porphycene molecule's cavity, respectively. The *cis* tautomer is more stable because of the alignment with the Cu atoms below. The location of the Cu adatom, with respect to the molecule, breaks the degeneracy and has a van der Waals influence on the energy difference between the two well minima. Figure reproduced from Ref. [27].

ages, above 150 mV, the two H atoms alternated from one side of the cavity to the other, i.e. from one *cis*-1 state to its mirror equivalent. This H transfer, or tautomerisation, is due to the STM tip, and it could be induced via the presence of a close by Cu adatom. If the tip was not to be considered and without a Cu adatom, then the two *cis*-1 states would have equal probability of occupation. This is supported by total energy calculations which considered the molecule, adatom, and surface, but not the tip. When the calculations were run without an adatom, the two states were found to be degenerate and their representative potential wells had minima equal in energy. Experimentally, the ratio between the two *cis*-1 states only changed when an adatom was brought to within 0.9 nm of the molecule, now the two H atoms would sit on the side of the cavity closest to the adatom. However, when the adatom was as close as possible, adjacent to the molecule, the molecule was permanently fixed in the state where the two H atoms are on the side furthest from the adatom. Calculations show the energy difference between the minima of the two wells, to be negative for the former, showing an attraction between the adatom and H atoms, and positive for the latter, showing a repulsion between the adatom and H atoms. Interestingly, the effect was removed when a second Cu adatom was placed in an

identical, symmetrical position on the other side of the molecule.

The energy difference between the two minima was calculated and plotted as a function of molecule centre to adatom distance. The plot resembled a Lennard-Jones potential, suggesting a van der Waals interaction between the porphycene and Cu adatom. This seems a reasonable explanation because the interaction takes place over large distances, between two neutral bodies, and changes from attraction to repulsion as the two bodies are brought together.

3.3.3 Controlling binding energies of manganese acceptors

D. H. Lee and J. A. Gupta [28] (Fig. 3.19) studied the electrostatic effect of precisely shifting an As vacancy closer to a Mn acceptor, on a *p*-type GaAs(110) surface at 7.3 K.

In filled-state STM imaging, the Mn acceptor had a dumbbell shape appearance, as the two adjacent As atoms appeared brighter. The As vacancy appeared as a point depression due to its positive charge. Positive voltage pulses of about 1.7 V were used to change the position of the As vacancy, and a smaller pulse of

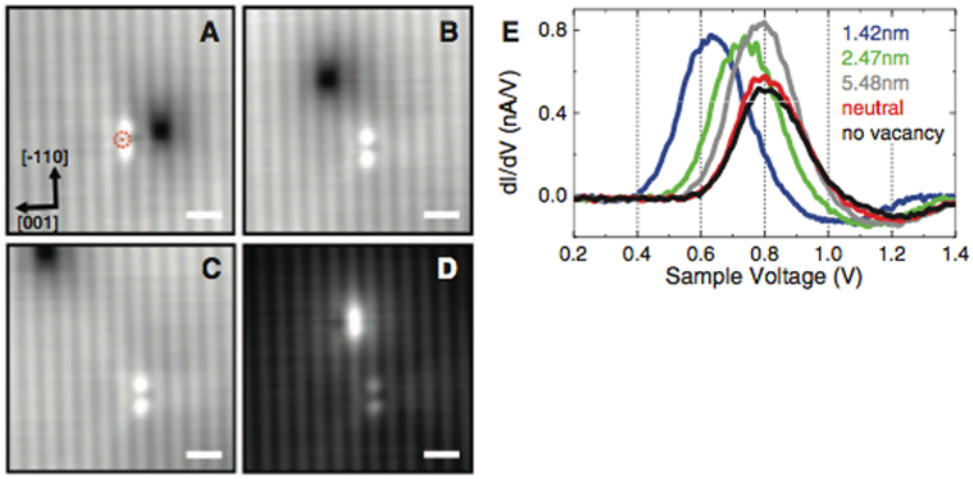

Figure 3.19: Series of STM images (−1.3 V, 500 pA, 1 nm scale bar) as an As vacancy is moved away from a Mn acceptor, dumbbell shaped, on GaAs(110). In **A**-**C**, the vacancy is positively charged, appearing dark, but in **D** it is neutral and bright. **E** has point conductance spectra taken on the acceptor for each image configuration. The peak or acceptor state is increasingly shifted to lower biases as the positive vacancy is brought closer. Figure reproduced from Ref. [28].

about 1.3 V, changed the charge state of the vacancy to neutral and its appearance to a bright protrusion. In differential conductance spectroscopy of the Mn acceptor, the peak within the GaAs bandgap, corresponding to the acceptor state crossing the Fermi level of the sample, moved to lower sample biases as the As vacancy was moved closer. A neutral vacancy had no effect, the peak remained in its original position.

Downward band bending is present in filled-state imaging and the positively charged As vacancy induces additional downward band bending, therefore the acceptor state is moved further down from the sample Fermi level and the spectroscopy peak is expected to move to higher biases. Varying the tip-induced band bending conditions in experiment, by using tips made from different metals, thus tips with different work functions, had no effect on the position of the Mn peak in spectroscopy. Moreover, spectroscopy taken of a surface Mn acceptor and subsurface Zn acceptor for different current setpoints showed that for increasing current, which decreased distance between tip and sample, and increased band bending, did not change the Mn peak position but the Zn peak moved to higher biases. This ruled out band bending as an explanation to the observed peak shift for Mn.

Instead the peak position of about 0.8 V corresponds to the binding energy of the hole to the acceptor. This is much greater than the bulk value of 0.11 eV, but expected for a surface dopant. The binding energy between the Mn acceptor and its hole was reduced due to the increasing Coulomb repulsion between the As vacancy and hole, in other words moving the vacancy finely modified the local electric field felt by the acceptor. This is supported by a plot of Mn peak position against distance between Mn acceptor and As vacancy, which could be fitted to a Coulomb function of $\frac{1}{r}$.

Rather than moving the As vacancy closer, the same effect of the Mn peak moving to lower biases could be achieved by increasing the number of As vacancies in the vicinity or using a Ga adatom which is positively charged. For the former case, the electrostatic effect felt by Mn acceptor is the sum of the individual Coulomb potentials from each As vacancy.

3.4 Transition-metal dichalcogenides

3.4.1 Bulk to monolayer; indirect to direct bandgap

Some semiconducting transition metal dichalcogenides, including MoS_2 [29, 30] and $MoSe_2$ [72], are known to transform from an indirect bandgap semiconductor to one with a direct bandgap when thinned from the bulk to the monolayer limit. This has proven to be an important discovery regarding the usefulness of atomically thin layers in optical, electronic, and spin applications, for the following reasons: the direct gap is preferred for its superior optical properties, the higher carrier mobilities, and the asymmetry of the single layer means spin-orbit splitting is still present. The higher carrier mobilities are present because the electrons become confined to a smaller vertical space, as the material is thinned from bulk to single layer.

The electronic band structure of bulk MoS_2 is displayed in Figure 3.20. The indirect gap is between the Σ, the midpoint between Γ and K, and Γ points of the Brillouin zone and it has a magnitude of 1.23 eV [73], whereas the direct gap lies at the K critical points and has a magnitude of 1.8 eV [29]. As the material is thinned towards the monolayer limit however, the indirect gap increases by over 0.7 eV [29] while the direct gap remains approximately the same.

The electronic states at K, and therefore the direct gap, do not vary so much

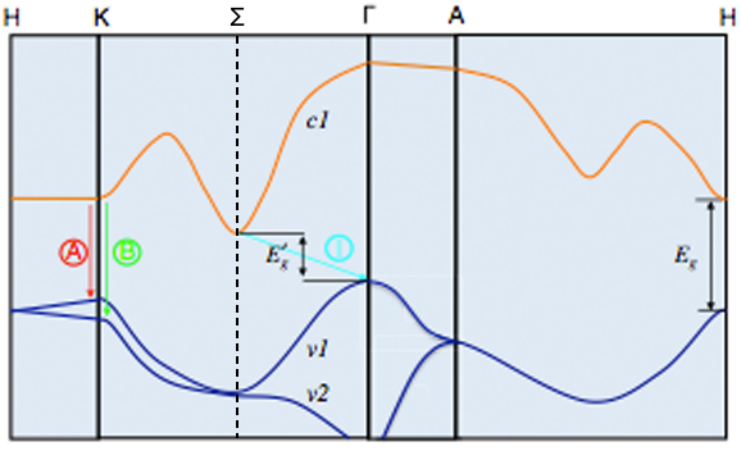

Figure 3.20: Band structure of bulk MoS_2, where E_g' is the indirect, bulk bandgap and E_g is the direct, monolayer bandgap. A and B are the transitions that occur across the direct gap and I is the indirect transition. Figure is reproduced from Reference [29].

when the number of layers are changed because they are related to the valence band and Mo orbitals and are more in-plane orientated. This is not the same for states near the Γ point, which are more sensitive to the number of layers, since they are related to the conduction band and S orbitals and are orientated out-of-plane. This explains why the indirect gap is greatly affected by the reduction in layers.

K. F. Mak *et al.* [29] exfoliate monolayers of MoS_2 from bulk using Scotch tape and use a number of optical spectroscopy techniques, including absorption, photoluminescence and photoconductivity measurements, to monitor the changes in band structure. A direct bandgap of 1.88 eV is measured for the monolayer. Plus, a monolayer is observed to appear bright in optical imaging, with the brightness dramatically disappearing with additional layers.

T. Eknapakul *et al.* [30] intercalate potassium between the first and second layers of a bulk MoS_2 sample, simultaneously increasing the size of the van der Waals gap, and donating electrons to the conduction band, thereby making the first, top layer, a quasi-monolayer. The intercalation is confirmed by X-ray photoemission spectroscopy and density functional theory calculations suggest the ratio c/a increases by about 25%, for the definition of a and c see Figure 2.16. Angle-resolved photoemission spectroscopy (ARPES) taken before and after the intercalation, see Figure 3.21, reveal the band structure changes; the conduction band minimum falls

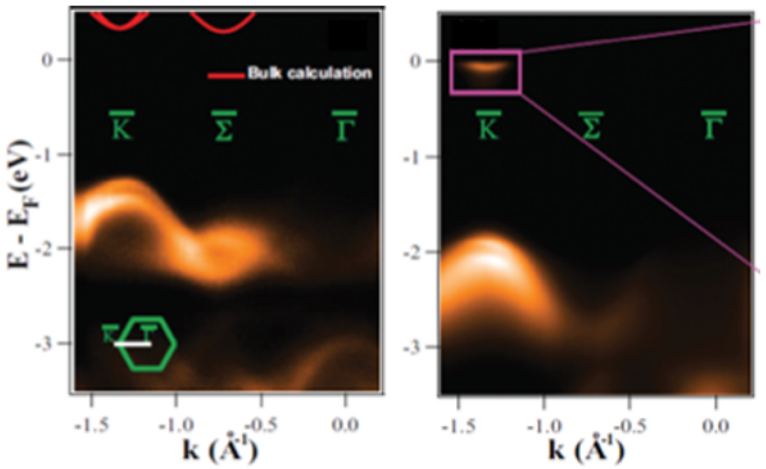

Figure 3.21: ARPES measured band structure of MoS_2 before (left) and after (right) K-intercalation, essentially a measurement of bulk and quasi-monolayer MoS_2, respectively. Figure is reproduced from Reference [30].

below the Fermi level at the K point to give a direct gap of 1.86 eV, whereas without intercalated K atoms, the conduction band minimum is at the Σ point.

A. J. Bradley *et al.* [72] have studied the electronic band structure of monolayer, bilayer and trilayer $MoSe_2$, using complementary experimental, scanning tunnelling spectroscopy, and theoretical, *ab initio* GW calculations, techniques. The layers lie on a graphene buffer layer above a SiC substrate. The same trend is observed, where the (indirect) band gap increases by almost an electronvolt from the trilayer to the monolayer, from 1.32 to 2.18 eV.

3.4.2 Charge density waves on layered materials

In order to provide background for the charge density wave (CDW) observations on K-intercalated MoS_2 that I present in Chapter 6, here, different STM case studies of the CDW phase of several layered materials are discussed. The materials examined include transition metal dichalcogenides, both in bulk and single layer form, and graphene doped via intercalation. The CDW is characterised by giving evidence for the following points:

- A periodic modulation in the surface charge density.
- The periodicity of the modulation does not change with bias; it is dispersionless.
- The opening of a small gap at the Fermi energy in the density of states.
- The filled- and empty-state imaged modulations are anti-phase.

This evidence will simultaneously exclude other possible causes, for instance Moiré patterns and quasi-particle interference effects.

In the following subsections, I will give brief accounts of five examples where STM and STS has been used to investigate CDW modulations. These are the CDW of bulk niobium diselenide ($NbSe_2$), the CDW of a single layer of $NbSe_2$, the CDW of titanium diselenide ($TiSe_2$) and its interplay with defects, the one-dimensional CDW along line defects on molybdenum diselenide ($MoSe_2$), and the one-dimensional CDW of calcium intercalated graphene (CaC_6). I will summarise the important information gained from these studies, after presenting the brief ac-

counts, and also point out areas of agreement and disagreement among these papers and how they relate to the new results I present in Chapter 6.

3.4.2.1 Bulk Niobium diselenide

C. J. Arguello *et al.* have observed charge density waves on the transition metal dichalcogenide 2*H*-$NbSe_2$ using STM [31]. They have, in particular, studied the transition from the normal metal phase to the CDW phase and the effect of surface defects. At high temperatures around 100 K, where charge ordering is not expected, CDW regions of nanometre dimensions appear localised around defects on the surface, see Figure 3.22. Thus, these defects seem to help stabilise the CDW phase. As the temperature is decreased, the CDW coverage increases until the CDW covers the entire surface, which is achieved below the transition temperature of 33.7 K.

The STM images the top Se layer and the defects, which as appear as a dark point depressions, are Se vacancies. The CDW has a commensurate $3a \times 3a$ periodicity, meaning it has a period exactly three times the surface Se atom spacing. The CDW transition temperature of 33.7 K was determined from transport measurements of sheet resistance as a function of temperature, and detected by the sudden

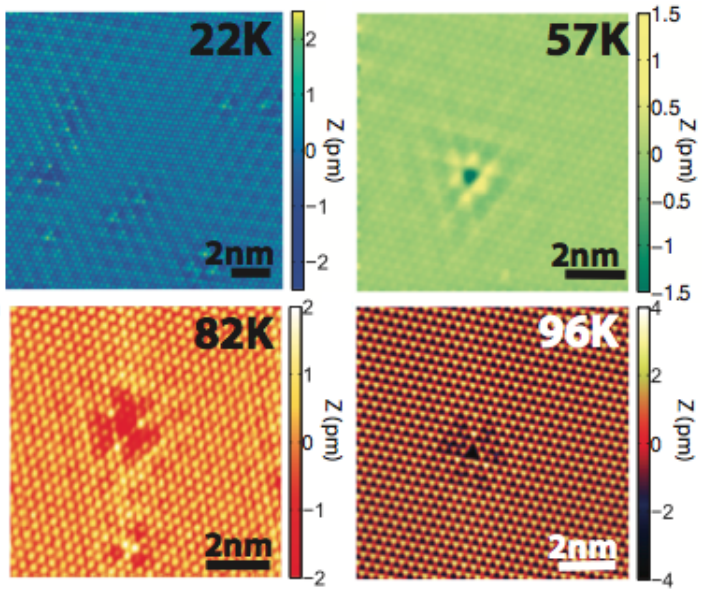

Figure 3.22: STM images of Se vacancies on different areas of $NbSe_2$ taken at different temperatures. Imaging conditions for 22 K image: −44 mV, 150 pA; for 57 K: −200 mV, 40 pA: for 82 K: −90 mV, 50 pA; and for 96 K: −230 mV, 20 pA. Figure is reproduced from Reference [31].

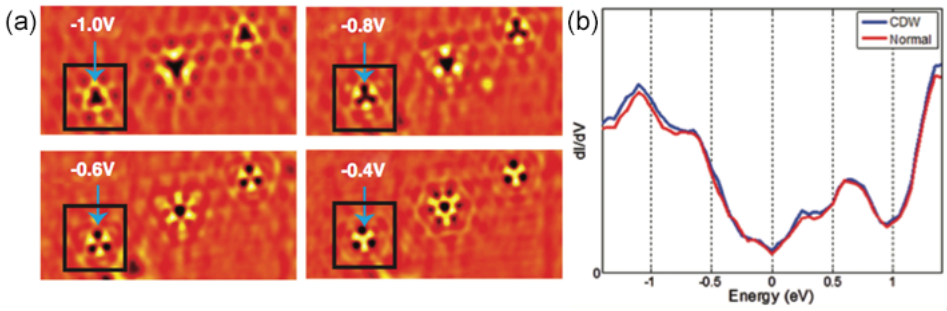

Figure 3.23: (a) STM images of a CDW on $NbSe_2$ at different biases, taken at 57 K. Images have been Fourier filtered to only keep the CDW spots. (b) Differential conductance curves taken experimentally on and off a CDW region at 57 K. Figure is reproduced from Reference [31].

increase in the gradient. Since having many separated CDW regions offers a greater resistance, because then there are regions hosting different correlated electron states, compared to a full coverage. Therefore, entering the CDW phase is accompanied by a large drop in resistance with respect to temperature.

Fourier transforms of temperature-dependent STM imaging reveals a CDW spot, whose wavevector remains constant but intensity increases as temperature decreases. The STS measurements and conductance maps display CDWs at all sample biases but with varying intensity and phase, and the corresponding Fourier transforms reveal the CDW wavevector to be bias or energy independent. This is an expected feature for a CDW, simultaneously ruling out Friedel oscillations as a possible explanation, which may have been expected for defects on a metal surface. In both cases, the CDW wavevector is a third of the atomic Bragg wavevector, corresponding to a 3×3 lattice.

STM images and differential conductance maps, which have been Fourier filtered to only keep the CDW contribution, display a phase change in the CDW pattern between -0.4 V and -1.0 V, see Figure 3.23 (a). This suggests that a CDW gap lies somewhere around -0.7 eV. Since the gap is not centred around the Fermi level it rules out a Peierls distortion as the cause but instead points to electron-phonon coupling. This is supported by density functional theory (DFT) calculated density of states, which displays a dip in the electronic states around the CDW wavevector and a gap opening around -0.6 eV. However, this expected gap does not appear

in point spectroscopy, shown in Figure 3.23 (b), which they explain is because this spectra is not a measurement at just the CDW wavevector but across an average of all wavevectors.

3.4.2.2 Single layer Niobium diselenide

M. M. Ugeda *et al.* used low temperature STM to study the ordered electronic ground states of a single layer of $NbSe_2$, including the CDW and superconductivity states and the interaction between them [32], whereas Arguello *et al.* studied bulk $NbSe_2$ [31].

The single layer of $NbSe_2$ was grown, by means of molecular beam epitaxy, on bilayer graphene on a 6H-SiC(0001) substrate. Temperature dependent STM imaging reveals the CDW remains at the single layer limit with the same 3×3 periodicity. The CDW regions expand, as the temperature is lowered, until the CDW covers the whole surface, see Figure 3.24 (a). Since the $NbSe_2$ layer sits on a graphene buffer layer, a Moiré pattern has to be ruled out as the cause for this 3×3 lattice. Firstly, the CDW lattice is invariant under rotation of the $NbSe_2$ layer with respect to the graphene, and secondly, the two layers do not have similar lattice constants, 0.344 nm for $NbSe_2$ and 0.250 nm for graphene, thus it cannot be a Moiré pattern. They state that their high quality samples have few defects, with

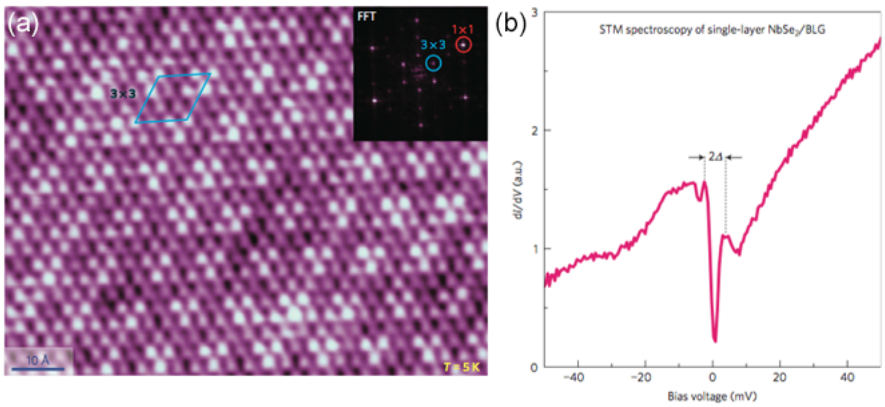

Figure 3.24: (a) STM image of single layer $NbSe_2$ in full CDW phase (image settings: -4 mV and 50 pA). Fourier transform of image is shown inset. (b) STS of single layer $NbSe_2$ displays a gap as indicated (spectroscopy settings: 5 K, 871 Hz, 100 pA and root-mean-square 0.6 mV). Figure is reproduced from Reference [32].

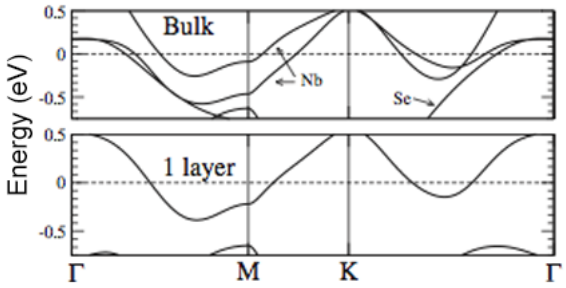

Figure 3.25: Calculated electronic band structure of bulk and single layer $NbSe_2$. Figure is reproduced from Reference [33].

no mention of a defect dependency as the CDW coverage increases.

Measurements of resistance through the single layer as a function of temperature were conducted using a four point probe system. Revealing a broadened superconducting transition beginning at 1.9 K, which is lower than the bulk critical temperature of 7.2 K. Although this is somewhat expected for a thinner sample because of its greater resistance. The transport measurements display no sign of a CDW transition. STM images taken at 25 K have a CDW coverage resembling that of the bulk around its CDW transition temperature. Suggesting the transition temperature has decreased from 33 K to about 25 K for the single layer.

Ugeda *et al.* refer to DFT calculated electronic structures of bulk and single layer $NbSe_2$, shown in Figure 3.25. These calculations were conducted by Calandra, Mazin and Mauri [33]. The calculated features and band gap in the single layer case match the experimental results, including those from differential conductance and angle-resolved photoemission spectroscopy measurements. For the bulk there are three bands crossing the Fermi level, whereas for the single layer there is just the one band. This suggests this one remaining Nb anti-bonding band is responsible for the CDW phase while the other, Nb and Se bands are important for the superconducting phase, which supports the findings that the CDW remains, but superconductivity is onset at lower temperatures, the critical temperature has decreased, for the single layer.

The narrow bias range conductance spectrum in Figure 3.24 (b), taken at 5 K, reveals a small CDW gap of (8 ± 2) meV centred at the Fermi level. This is a much smaller value compared to previous bulk studies, for example Soumyanarayanan *et*

al. measured a gap of 24 meV using STS [74]. A small gap suggests a weakly coupled CDW, formed as a result of the opening of a gap on the Fermi surface, known as Fermi surface nesting, but this is countered by the fact that the CDW pattern remains at higher biases. The gap is now measurable due to the more simple electronic structure, i.e. only one band crosses the Fermi level, but it was not predicted by DFT. Conductance maps of the surface taken at biases outside and inside the gap, show and do not show the CDW modulations, respectively. Plotting the Fourier intensity of the CDW spot, from Fourier transforms of a range of conductance maps, as a function of bias reproduces a gap. This is presented as proof the gap is a CDW gap. Interestingly, the point conductance spectra of Arguello *et al.* (Figure 3.23 (b)) do show a dip around zero bias.

3.4.2.3 Titanium diselenide

A. M. Novello *et al.* have investigated if and how the CDW phase of 1*T*-$TiSe_2$ is influenced by point defects, using STM imaging and DFT [34]. Defects can have a great effect on the CDW state, as discussed earlier, defects on $NbSe_2$ make the CDW partially appear at temperatures far higher than the transition temperature [31], and understanding this relationship can allow us to learn more about the CDW.

The 1*T*-$TiSe_2$ crystals used were grown by the iodine vapour transport method and were cleaved in vacuum. At a temperature of about 202 K, 1*T*-$TiSe_2$ undergoes a transition to a commensurate CDW phase. The STM experiments were conducted at a temperature of 4.7 K, well below the CDW transition temperature. In STM imaging of cleaved 1*T*-$TiSe_2$, Figure 3.26, a CDW with a 2×2 lattice is observed on the top Se layer, as well as four types of defects. From a previous study these four defects were determined to be: Se vacancies on the surface (type A), I substituted for Se in the bottom Se layer of the first $TiSe_2$ layer (type B), O substituted for Se in the bottom Se layer (type C) and self-intercalating Ti sitting in the van der Waals gap between the first and second $TiSe_2$ layers (type D). There are however two inequivalent sites for each defect, depending on whether the defect lines up with a bright Se atom of the CDW or not. For the vacancy defect, Figure 3.27 (a,b), the missing atom can be a bright Se atom or not, whereas the other three defects,

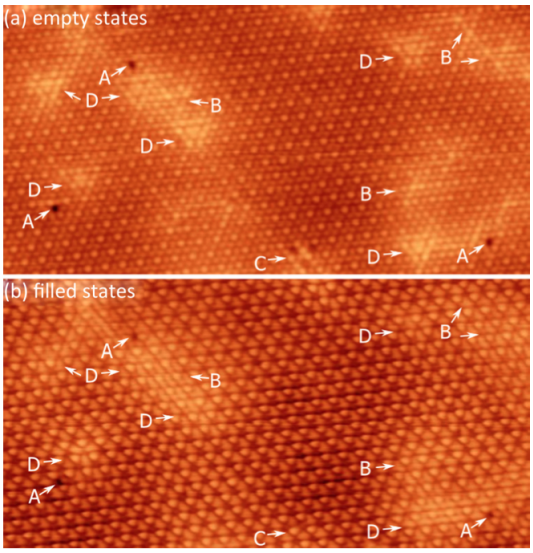

Figure 3.26: (a) Empty-state (0.15 V) and (b) Filled-state (−0.15 V) STM image of 1*T*-$TiSe_2$ (image settings: 0.2 nA tunnel current and 22.2 nm × 11.4 nm in size). Four types of defects are observed A,...,D. Figure is reproduced from Reference [34].

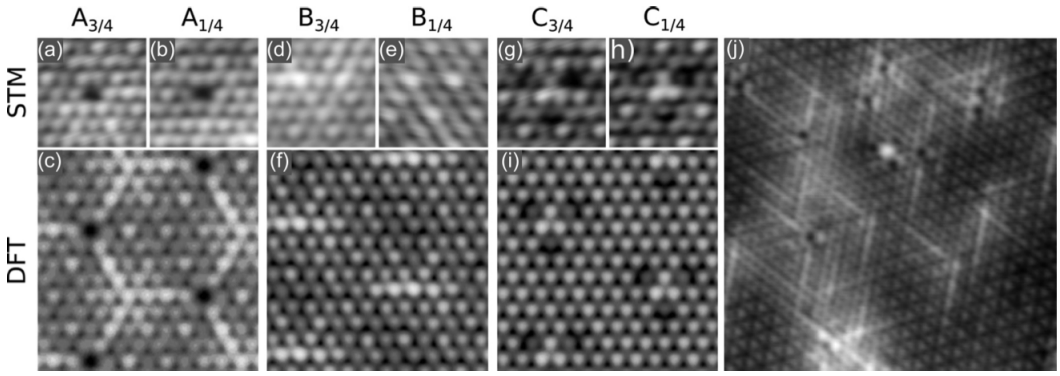

Figure 3.27: STM images of Se vacancies (a,b), I substitutions (d,e) and O substitutions (g,h) at a 3/4 and 1/4 site, respectively. (c,f,i) Simulated STM images, calculated using DFT, of the three types of defect. (j) Large scale STM image of defects A and B on a sample fabricated at a lower temperature, 575° instead of 650°, so to have fewer Ti intercalants (image settings: 150 mV, 0.2 nA and 11.5 nm × 11.5 nm). Figure is reproduced from Reference [34].

Figures 3.27 (d,e,g,h) and 3.28 (a,c,e,g), can be positioned adjacent to a bright Se atom or not. Since the CDW has 2 × 2 periodicity, there are three equivalent (3/4) and one inequivalent (1/4) sites for all defects, with the two sites producing STM images of differing appearances.

For each defect type, the distribution between 3/4 and 1/4 site versions was counted from a large scale STM image (50 nm × 50 nm) and the ratio between the

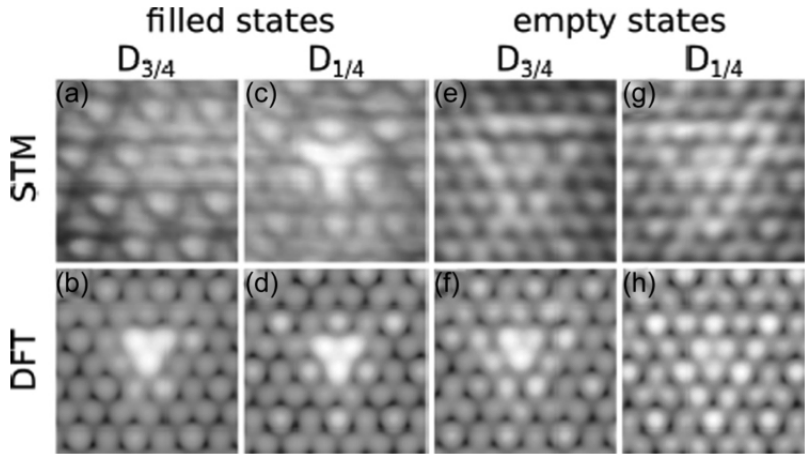

Figure 3.28: (a,c) Filled-state (−150 mV) and (e,g) empty-state (150 mV) STM images of defect D: intercalating Ti. at a 3/4 and 1/4 site, respectively. (b,d,f,h) DFT simulated STM images equivalent to (a,c,e,g). All images taken at tunnel current setting of 0.2 nA. Figure is reproduced from Reference [34].

two types was found to be three. The CDW is not observed to affect this ratio and alter it from its expected value i.e. there is no preferential site. This fact is offered as proof that the defects do not interact with the CDW state. This can also be seen in the STM imaging, since the CDW has a strong quality and is not interrupted by the presence of these defects, remaining commensurate. This, however, may not be the case for greater intercalation levels.

Se vacancies, defect type A, are easy to observe since they appear as dark sites at all biases (Figure 3.27 (a,b)). The other three defects, B, C and D, have a brighter appearance, which differs somewhat between the two inequivalent sites, and are easier to observe at unoccupied sample biases (Figures 3.27 (d,e,g,h) and 3.28 (e,g)). Defects A and B appear as bright atomic lines on the surface when in the 3/4 site, Figure 3.27 (a,d), as the vacancy and larger I atom induce strain in the lattice. In the STM imaging these atomic line features are overlaid on the CDW, proof the defect appearance is not linked to the CDW. Although the presence of self-intercalating Ti can prohibit the appearance of these chains, see Figure 3.27 (j). Defects C and D appear as triangular formations on the surface, Figures 3.27 (g,h) and 3.28 (a,c,e,g). All of these defect appearances were well matched when compared with DFT simulations, including the bright atomic lines for defects A and B and the triangular formations for C and D, as shown in Figures 3.27 (c,f,i) and 3.28 (b,d,f,h). For de-

fects A to C, the experimental images were reproduced without having to include the CDW in the DFT calculations this was not the case for defect type D.

Apart from the Se vacancies, defect A, only the intercalating Ti, defect D, is observed in occupied states imaging (Figure 3.28 (a,c)). This is said to suggest that the CDW gap lies in the direction of the occupied states. Observation of defect type D in occupied states imaging is attributed to the fact that, as an intercalant, it is a donor species and it introduces electronic states within the gap.

3.4.2.4 Molybdenum diselenide

S. Barja *et al.* have discovered a one-dimensional CDW along line defects on the surface of single layer $MoSe_2$, using STM at a temperature of 4.5 K [35]. Importantly, this is the first observation of a CDW on a semiconducting transition metal dichalcogenide. As with the work by Ugeda *et al.*, the $MoSe_2$ monolayer sits on a bilayer of graphene, above a SiC(0001) substrate.

In the STM image in Figure 3.29 (a), bright pairs of parallel lines are found on the surface of $MoSe_2$. Their brightness varies significantly with sample bias, which tells us that the brightness is not due to the height of the defect but its elec-

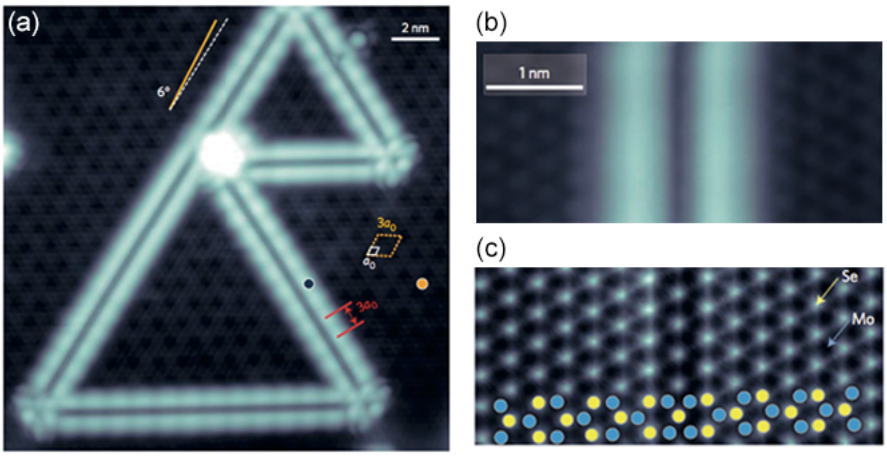

Figure 3.29: (a) STM image of mirror twin boundaries (MTB) on the surface of $MoSe_2$ (image settings: -1.3 V and 20 pA). Yellow unit cell is for the Moiré pattern on the $MoSe_2$ surface and the red arrow is the modulation for the CDW along the MTB. (b) Close-up STM image of a MTB (settings: -1.5 V and 10 pA). (c) Non-contact AFM image of the same MTB in (b), displays the atomic structure of the defect (same scale bar as (b)). Yellow circles are Se atoms and blue circles are Mo atoms. Figure is reproduced from Reference [35].

tronic states instead. The atomic structure of these line defects was resolved by non-contact atomic force microscopy, see Figure 3.29 (c), possible because electronic features do not have an influence on this imaging technique. The defect was revealed to be a line of Se atoms surrounded by a line of Mo atoms on either side, the Mo lattice is reflected across the Se atom line, hence the name mirror twin boundary (MTB), while the Se lattice is unaffected.

A 3×3 Moiré pattern is observed across the whole surface, formed between the $MoSe_2$ and underlying graphene, but a charge density modulation with a periodicity of 3 lattice constants is observed along the MTBs. The periodicity of the Moiré pattern varies from 2 to 3, whereas the CDW periodicity varies across a smaller range from 2.84 to 3.14. Rotations of up to 20° were found between the Moiré lattice and the atomic lattice or MTB directions, for example in Figure 3.29 (a), there is an angle of 6° between the two directions. Finally, MTBs hosting the CDW were observed on additional layers of $MoSe_2$, i.e. on islands and across step edges. The above three stated reasons prove the CDW is not a result of the Moiré pattern, even though their similar periodicities could lead to this conclusion. The MTBs are of finite length, which raises the possibility that the observed feature may be the bound states of a quantum well and not a CDW. But the periodicity does not change as the bias is increased and this dispersionless feature is a sign of a CDW.

Scanning tunnelling spectroscopy taken on the background $MoSe_2$ surface indicates it is a semiconductor, a band gap of 2.18 eV is measured, whereas spectroscopy taken on the MTB does not display this semiconducting band gap but instead a smaller gap is present at the Fermi level, this proves the defect is metallic and it holds a CDW. This CDW gap has average width of (100 ± 40) meV and conductance maps of the MTB taken at biases of the occupied and unoccupied coherence peaks, i.e. immediately to the left and right of the gap, display the edge states around the gap whose modulations are out of phase, see Figure 3.30. The electronic modulations in imaging, the gap in conductance spectra, and the out of phase conductance maps are all offered as proof that what is being observed is a CDW modulation.

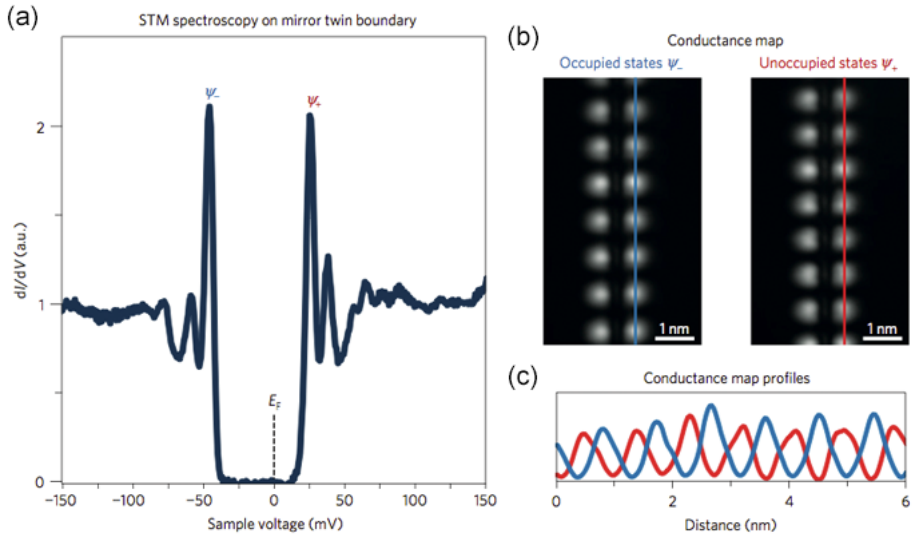

Figure 3.30: (a) Point differential conductance spectrum taken on MTB on $MoSe_2$, shows a 73 meV gap around the Fermi level. (b) Differential conductance maps of a MTB taken at biases just below and above the gap. (c) Line profiles taken along the conductance maps in (b) show the CDW in the occupied and unoccupied states are out of phase. Figure is reproduced from Reference [35].

DFT was used to model a Peierls distortion, where the atoms along the MTB are perturbed by 5 pm. This subsequently opened up a 50 meV gap in the calculated band structure, at the CDW wavevector, but 0.175 eV above the Fermi level. By taking this energy shift into account, they were able to successfully replicate the differential conductance spectrum including the CDW gap, via the calculated projected density of states. The calculated local density of states maps show the same out of phase modulations between the occupied and unoccupied states as experiment, proof this CDW is the outcome of a Peierls distortion.

3.4.2.5 Calcium intercalated Graphene

K. C. Rahnejat *et al.* were the first to discover a CDW on the surface of Ca-intercalated graphene, CaC_6, which appears in a striped formation [36]. In this sample, layers of Ca atoms are stacked between the graphene layers, within the van der Waals gap, and this high doping level gives it a metallic electronic structure and allows it to superconduct. Measurements of DC magnetisation and electrical resistance for bulk CaC_6 as a function of temperature revealed a known superconducting transition at 11.5 K and a previously unknown CDW transition around 250 K.

The discovery was made in STM experiments that were conducted at 78 K and at this temperature the sample is in its CDW phase. In STM imaging and corresponding Fourier transformations, as displayed in Figure 3.31, a hexagonal C lattice, with lattice constant $a = 0.25$ nm, of the top, imaged graphene layer and a hexagonal Ca superlattice, with lattice structure $(\sqrt{3}a \times \sqrt{3}a)R30°$, of the subsurface intercalant layer is always observed. However, sometimes, in addition to these two lattices, a third lattice is also observed at the same image settings. A commensurate one-dimensional or striped CDW modulation, of period 1.125 nm, is seen along one of the Ca superlattice vector directions, for which the lattice structure is $(3\sqrt{3}a \times \sqrt{3}a)R30°$. In the striped phase, the C and Ca lattices are still present, providing evidence that the striped phase is a CDW and not a surface reconstruction.

Line profiling along the primitive vector directions of an STM image where the C lattice is more protruding, shows the C lattice is not disturbed. But exercising the equivalent for the Ca superlattice shows the Ca lattice is disturbed. It was found that every Ca atom in the row that lies directly underneath the maximum amplitude

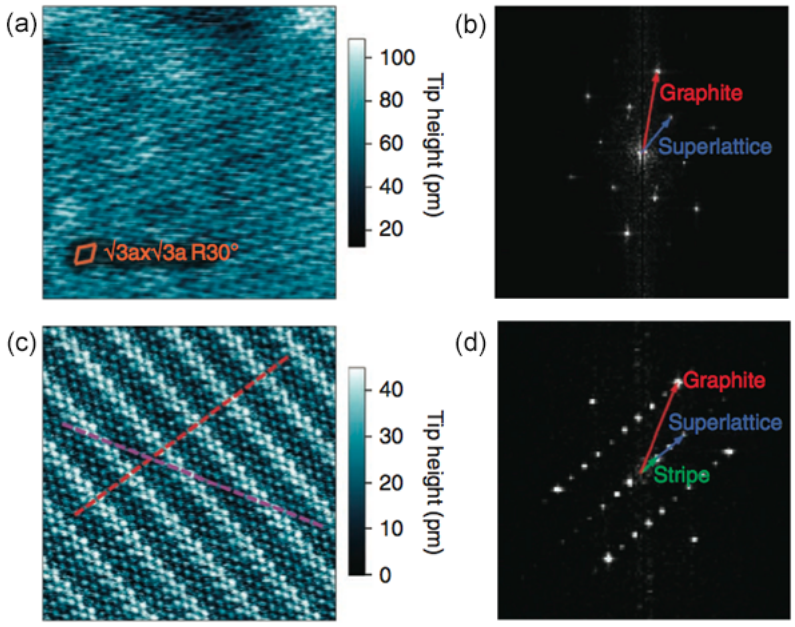

Figure 3.31: (a) STM image of CaC_6 and (b) associated Fourier transform showing a C (graphite) lattice and Ca superlattice. (c) STM image and (d) associated Fourier transform of the striped CDW lattice. The graphite lattice and superlattice are still present. Both images were taken at 300 mV and 50 pA and are 7 nm $\times$ 7 nm in size. Figure is reproduced from Reference [36].

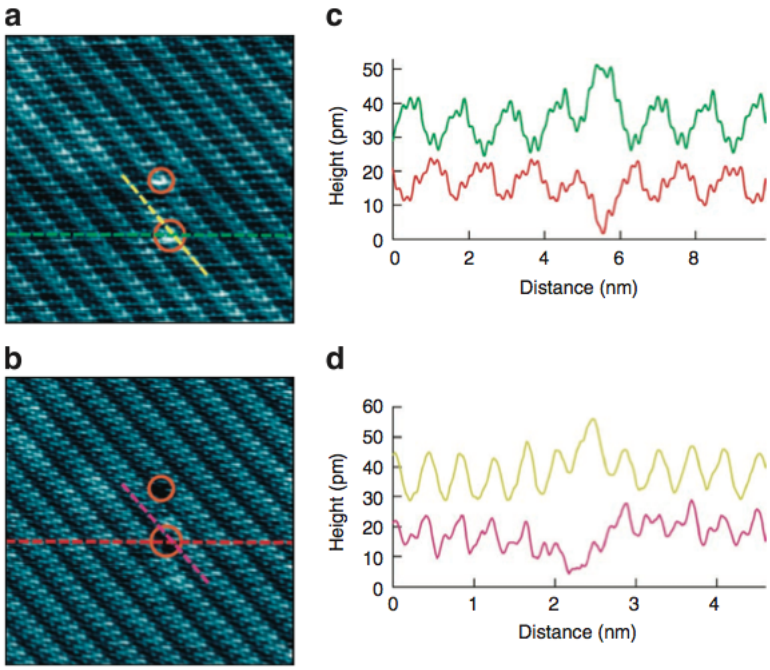

Figure 3.32: (a) Filled-states (-700 mV) and (b) empty-states (700 mV) STM image of the same striped CDW region on CaC_6. Both images were taken at 50 pA and are 10 nm $\times$ 10 nm. The circles enclose defects and the colour of the lines in (a,b) match their associated height profiles in (c,d). (c) Line profiles taken across the stripes, modulations are out of phase between filled- and empty-states. (d) Line profiles taken along a strip, Ca superlattice is unaffected by bias polarity change. Figure is reproduced from Reference [36].

of the striped modulations is moved by (0.06 ± 0.02) nm. Cooling the sample, for the STM experiments, would have made the graphene layers more flat resulting in this distorting shift of the Ca lattice, which in turn could be the cause for the striped CDW. Though this striped phase did have a finite lifetime, after which it was no longer observed for the particular surface.

Figure 3.32 shows filled- and empty-states STM imaging of the same striped region. The striped phase modulations are out of phase with one another when the bias polarity is reversed, so a peak becomes a trough and vice versa, while at the same time the Ca lattice is unaffected by the change in bias polarity. This is an indication that the striped phase is a CDW and present in the top graphene layer.

A CITS measurement of a striped phase region was used to produce a numerically differentiated conductance map as a function of position and bias. The conductance spectra for every point on the map were averaged (Figure 3.33 (a)), exhibiting

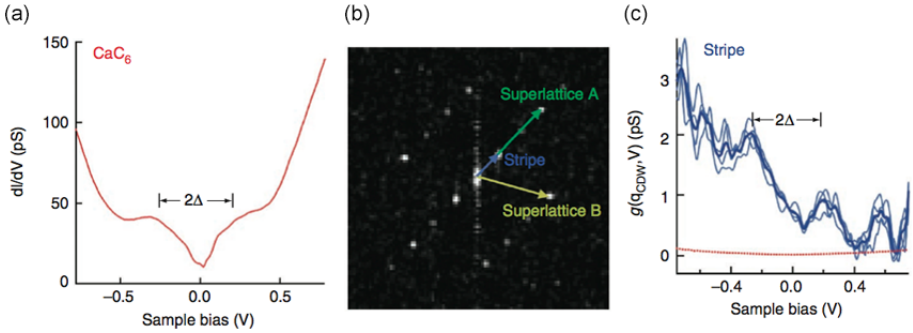

Figure 3.33: (a) Average of every differential conductance spectrum taken with the CITS measurement of CaC_6 (60000 spectra regulated at 800 mV and 50 pA). (b) Fourier transform of the zero bias differential conductance slice taken from the CITS measurement. The C, graphite lattice spots are missing and were not captured because of low resolution in the CITS measurement. (c) Fourier intensity against bias for the striped CDW spot, marked in (b) by a blue arrow, bold curve is an average of the faint curves taken from different measurements. These curves were normalised by subtracting the background equivalent, shown in red. Figure is reproduced from Reference [36].

a gap of approximate width 475 mV at the Fermi level, while at zero bias the conductance is not zero, verifying the sample's metallic character. A point to note is that the gap in the conductance spectra or density of states would not be possible for a Moiré pattern, further evidence for a CDW. Fourier transforming the conductance map gives the measurement as a function of reciprocal space. The spots, equivalent to those from Fourier transforms of STM images (Figure 3.31 (b,d)), were shown not to change with bias or energy. Since the stripe spot is dispersionless, it rules out quasi-particle interference effects, such as Friedel oscillations, as the source of the stripe feature. In the Fourier transform from Figure 3.33 (b), Superlattice A is the Ca lattice vector that crosses the stripes and Superlattice B is the Ca lattice vector that runs alongside the stripes. The spectrum in Figure 3.33 (c) is for the stripe's spot and it has a gap of around 475 mV at the Fermi level, this directly links the gap to the stripe phase, as expected for a CDW.

3.4.2.6 Summary

Findings from this literature review of CDW hosting layered materials, as well as other common examples, are summarised in Table 3.1. The TMD whose transition metal features in group IV of the periodic table (Ti–) has a CDW lattice with a pe-

Layered material	CDW Lattice	CDW gap, 2Δ (mV)	Transition temperature, T_{CDW} (K)	Critical temperature, T_c (K)
$NbSe_2$ (bulk)	3×3 [31]	24 [74]	33.7 [31]	7.2 [32]
$NbSe_2$ (single-layer)	3×3 [32]	8 [32]	~ 25 [32]	0.65 [32]
$TiSe_2$	2×2 [34]	232 [75]	202 [34]	NA
$TaSe_2$ (2*H*–)	3×3 [76]	160 [76]	122.3 [76]	0.15 [77]
TaS_2 (2*H*–)	3×3 [76]	100 [76]	75.3 [76]	0.8 [77]
$MoSe_2$	3×1 [35]	100 [35]	—	NA
CaC_6	$(3\sqrt{3} \times \sqrt{3})R30^\circ$ [36]	475 [36]	250 [36]	11.5 [36]

Table 3.1: Summary of CDW related properties of various layered materials.

riodicity of 2×2, whereas for the TMDs with group V transition metals (Nb– and Ta–) have a 3×3 CDW lattice but only in the case of the 2*H* polytype. However, 1*T*–$TaSe_2$ and 1*T*–TaS_2, the polytypes with tetragonal symmetry, host more complicated CDWs passing through phases of incommensurate to nearly commensurate to, finally, commensurate with decreasing temperature.

The CDW observed on bulk $NbSe_2$, at temperatures above the CDW transition temperature, and on $MoSe_2$ appears localised to surface defects. Se vacancy defects for the former, and line defects, known as mirror twin boundaries, for the latter. The CDWs are all observed on metallic materials, for the case of the semiconductor $MoSe_2$, the defect is shown to have properties of a metal, and for the semi-metal graphene, the intercalation of Ca has made it metallic. The investigation for the CDW on bulk $NbSe_2$ was the only one not to find an energy gap in spectroscopy measurements, although, an observed phase change, along with DFT calculations, suggests a gap is expected but not one centred around the Fermi level. Whereas the other energy gaps reported were found at the Fermi level.

We report in Chapter 6, a CDW on potassium intercalated molybdenum disulfide. The CDW appears surrounding a defect, as seen for bulk $NbSe_2$ and $MoSe_2$, but interestingly, the coverage changes with varying sample bias. The coverage was found to increase with decreasing bias magnitude. The intercalation of K made the semiconducting MoS_2 metallic. The opening of an energy gap in the density of states was observed around the Fermi level, from spectroscopy measurements and

their Fourier transforms, similar to those seen for CaC_6, $MoSe_2$, and single layer NbSe_2.

Chapter 4

Methods

4.1 Experiment

Experiments were performed using an Omicron NanoTechnology Low Temperature (LT) STM. Operated under ultra-high vacuum (UHV) conditions, where the base pressure of the chambers was typically in the 10^{-11} mbar range, maintained with the use of ion getter pumps and titanium sublimation pumps [78]. The STM system was isolated from vibrations using damping mechanisms. The STM head was suspended from a spring within the vacuum chamber and the STM table sat on active damping systems, which measure vibrations and rectify them using piezo components. The experiments on the Si(001) surface were carried out at liquid nitrogen temperatures 78 K. Experiments on the MoS_2 surface were conducted at liquid helium temperatures 5.5 K.

All the STM images presented in this thesis have been plane fitted. This fitting is required because the original data for an STM image will not be level, since the tip and sample are not orthogonal to one another. This sloped image is corrected by fitting it to a plane and subtracting this from the original data. The images obtained from experiments on Si(001) were processed in Igor Pro (Version 6.37), using a macro package written by Dr Steven R. Schofield [79], and then skew corrected in Adobe Photoshop CS6 (Version 13.0.6) to remove effects of drift and scanner calibration offsets. Images from experiments on MoS_2 were processed in SPIP: Scanning Probe Image Processor by Image Metrology (Version 4.6.3), where the unit

cell of the S lattice was iteratively corrected in the Fourier transform of the image, effectively fixing the distance of the Bragg spots to the expected value, corrections of about 3 % were required. The macros for Igor Pro were also used to process the spectroscopy results, they were particularly useful regarding the Fourier transformation of Current Imaging Tunnelling Spectroscopy (CITS) data, as discussed in Section 2.5.1.

4.1.1 Preparation of STM probe tips

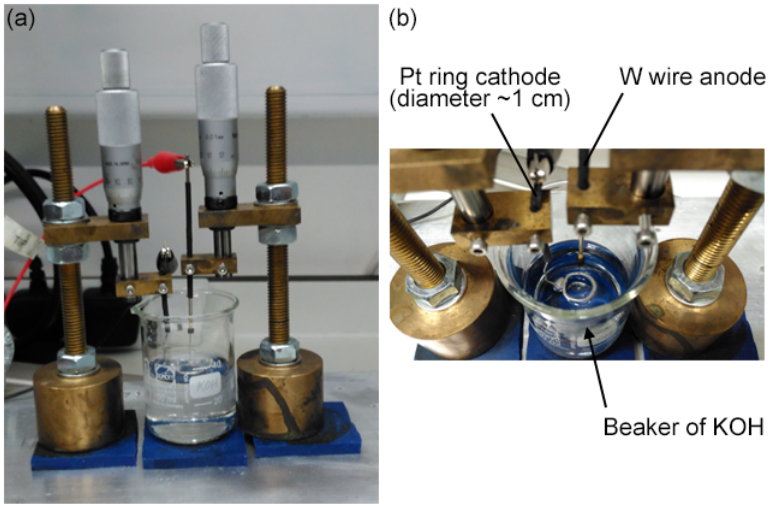

Figure 4.1: Photographs of the tip etching process being carried out in our home-built system. The W wire, which will form the tip, is the anode and it is placed at the centre of the Pt ring cathode, in this electrolysis reaction. The ring sits just below the KOH meniscus, with the wire sitting slighter deeper.

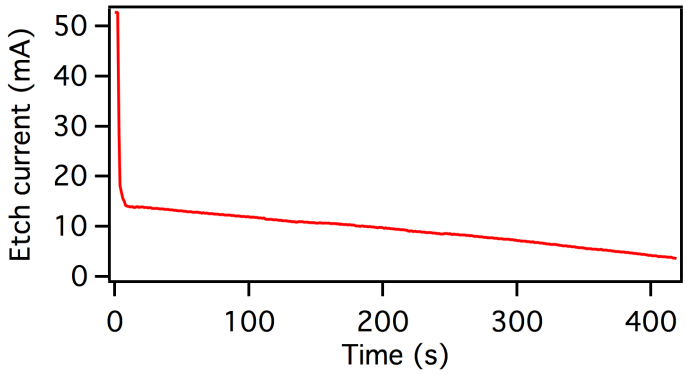

Figure 4.2: The current measured during the tip etching process, which takes about 7 minutes to run. A bias voltage of 4.5 V was being applied across the two electrodes.

The STM tips were made by electrochemically etching tungsten W wire, of diameter 0.25 mm and purity 99.9 %, in potassium hydroxide KOH, of concentration 3 Mol. The W wire was purchased from Sigma Aldrich and the etching process was carried out in a home-built system, displayed in Figure 4.1. Figure 4.2 features a typical plot of the etch current versus time, measured during the process. After etching and examination under an optical microscope, an example of which is shown in Figure 4.3, the tips were sonicated in deionised water. This sonicating resulted in a loss in sharpness, as the end is sheared off as shown in Figure 4.4, but a gain in stability. In experiments, the sonicated tips proved to be better for hydrogen lithography, giving more controlled desorption, removing single H atoms from the selected site.

Once in-vacuum, the tips were degassed overnight, by resistive heating to

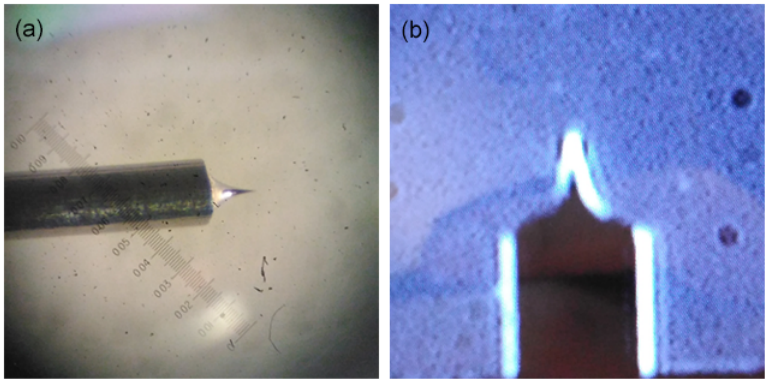

Figure 4.3: (a) A photograph taken through an optical microscope as a freshly etched tip is checked. (b) A photograph of the camera view of a tip on the STM stage. The W wire has a diameter of 0.25 mm to give an idea of the scale.

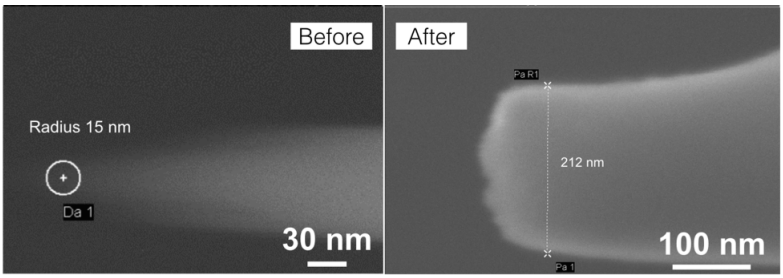

Figure 4.4: Scanning electron micrographs of a W tip before (left image) and after (right image) sonicating. The width of the tip end is 30 nm and 200 nm, respectively. The SEM images were taken by summer student Muhammad Shu'aib Kamaludin.

around 150 °C, and then a sequence of electron bombardment and field emission was used to remove the tungsten oxide layer.

Electron bombardment annealing was carried out by positively biasing the tip, to 400 V, and positioning it close to a heated W filament, a 2 mm diameter ring made of 0.25 mm diameter wire. This way electrons, thermionically emitted from the filament, are accelerated towards the tip. The filament current was controlled to set an emission current of about 40 μA and this e bombardment was carried out for five minutes.

The application of voltage sweeps to the tip, from 0 up to a high voltage of

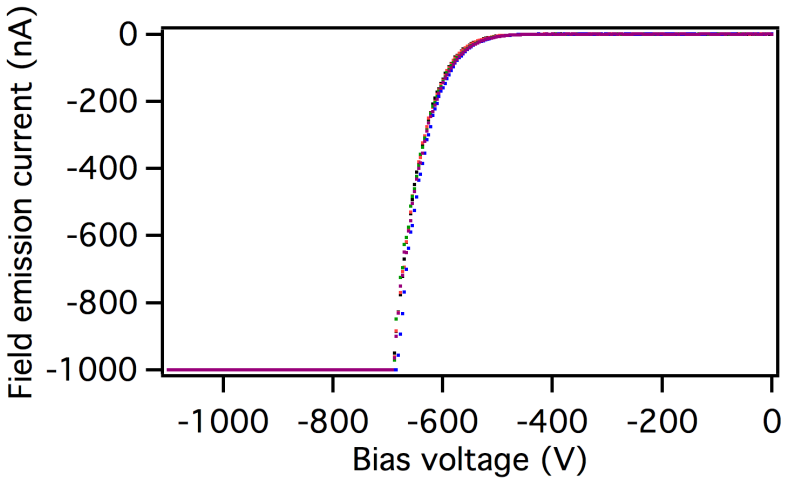

Figure 4.5: Five successive field emission curves overlap perfectly after electron bombardment annealing.

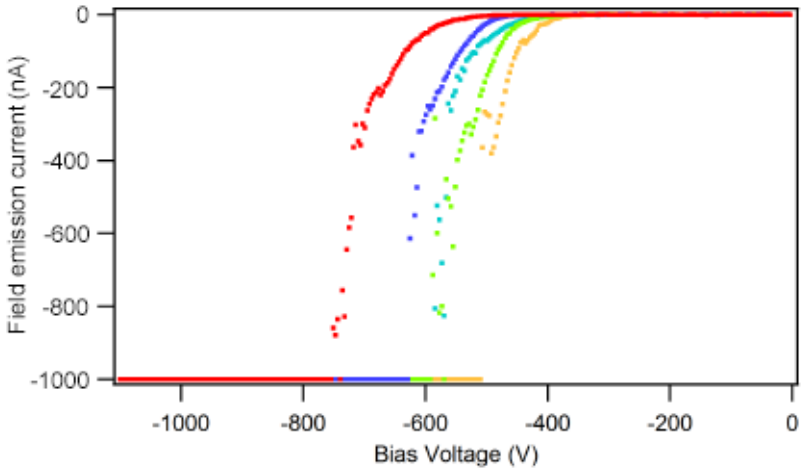

Figure 4.6: Five successive field emission curves before electron bombardment annealing.

-1.1 kV, results in electron (Fowler-Nordheim) field emission, during this part the filament was grounded. The first ten, or so, field emission (I vs V) curves may not overlap straight away as the atomic configuration of the tip is still changing, but once successive field emissions were identical (Figure 4.5) the tip was assumed to be stable and ready for use. In comparison to the field emissions in Figure 4.6, which were taken before e bombardment.

These processing steps roughly follow the procedure outlined by Ekvall *et al.* [80].

4.1.2 Preparation of H-terminated Si(001) samples

The Si(001) samples were cleaved into 12 mm by 3 mm chips from wafers, manufactured by Virginia Semiconductor Inc., degenerately doped with arsenic (n-type) giving a resistivity between 0.0015 and 0.004 Ωcm. These chips were then mounted on STM sample plates, in a direct heating configuration, see Figure 4.7. In-vacuum, the samples were degassed, by resistive heating, at approximately 500 °C overnight and then flash annealed, via direct current heating, to about 1250 °C for 10 seconds. Figure 4.8 contains more details about the Si flash process. The high temperature of 1250 °C removes oxide layers and carbon contaminants from the surface creating large, flat terraces suitable for imaging [81]. The flash annealing process includes a controlled cooling period to allow the surface to reconstruct. Such high temperature flashes are known to deplete dopants from the surface; making it more intrinsic [82].

The Si(001) surface was hydrogen terminated by exposing it to a dose of monoatomic H ($\sim 10^{-7}$ mbar) for 5 minutes, while the sample was held at a temperature just under 300 °C. A Hydrogen Atomic Beam Source, from MBE Komponenten GmbH, was used to thermally crack the molecular bonds in H_2 and produce monoatomic hydrogen. The difficulty encountered in producing a good monohydride termination was finding the right temperature to heat the sample to. If the sample was too cold, hydrogen would instead etch the surface, and if the sample was too hot, hydrogen would not bond with the silicon surface atoms.

To create dangling bonds on Si(001):H, H atoms need to be desorbed from

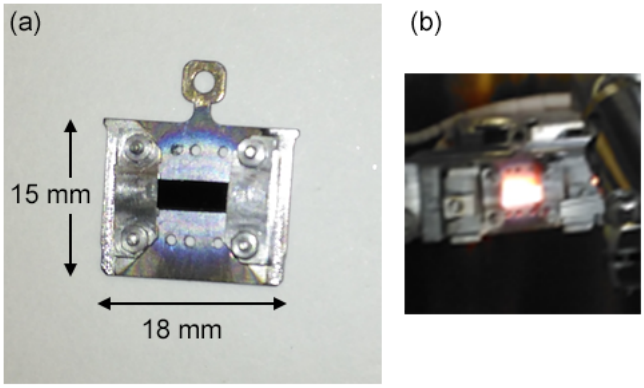

Figure 4.7: (a) A Si(001) sample mounted onto a standard Omicron molybdenum sample plate and held in position by two tantalum clamping foils. (b) A Si(001) sample glowing, in-vacuum, during a 1200 °C flash.

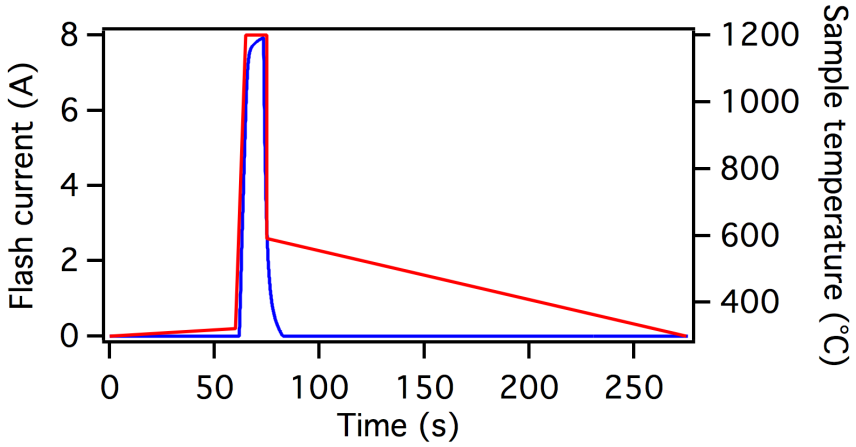

Figure 4.8: A trace of the direct current that passes through a silicon sample for the flash annealing process, along with a plot of the resultant temperature rise in the sample measured using a pyrometer from IMPAC Infrared GmbH (model IGA 50-LO plus).

the surface [1]. This was done by imaging in the empty-states, low bias and high current settings were used to bring the tip closer and give better atomic resolution (Figure 4.9); positioning the tip above the selected H atom for removal; and applying a voltage pulse of ~ 2 V for 10 ms. Slightly larger voltage pulses were required for producing additional DBs in the vicinity of the first because this area becomes depressed, i.e. depleted of electrons, due to the negative charge of the first DB.

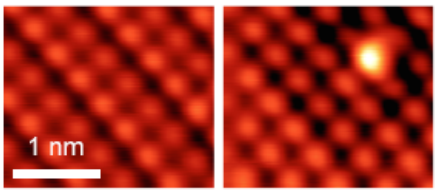

Figure 4.9: STM images showing the creation of a DB on H-terminated Si(001). The images were taken at a setting of 1 V and 300 pA.

4.1.3 Preparation of K-intercalated MoS_2 samples

The MoS_2 samples were intercalated and prepared for STM investigation by our collaborators Dr Chris Howard of University College London and his PhD student Mohammed Kashim bin Subhan. These samples are of high quality and quite unique, since there are not many research groups around the world with expertise to perform this difficult intercalation process.

Single-crystal MoS_2 was purchased from Manchester Nanomaterials Ltd. and degassed at 250°C in vacuum, within an air tight glass-metal transition tube, before use. Once degassed and the pressure has fallen below 10^{-6} mbar, it is transferred to a inert, Ar gas atmosphere glove box where the processes of intercalation and mounting to a STM sample plate takes place.

The MoS_2 was intercalated with alkali metal K via the liquid ammonia (NH_3) method [83]. The MoS_2 crystal and a stoichiometric amount of K were place in a transition tube, subsequently attached to an ammonia rig and pumped down to below 10^{-6} mbar. The tube is then immersed in a bath of isopropanol, held at a temperature of -50°C. NH_3 is then condensed into the tube, forming a blue solution with the MoS_2 and K, the colour of which is a result of the free electrons in NH_3. The tube is left in the bath until the solution has turned colourless, signalling the end of the intercalation process, and finally the remaining NH_3 is then cryogenically pumped off. The success of the intercalation is checked using x-ray diffraction, where one would expect to see the $00l$ peak shift to lower angles due to an increase in the interlayer separation d.

Flakes of K-intercalated MoS_2 were cleaved from the crystal by cutting through the c-axis, using a blade, and breaking the weak interlayer bonding be-

tween layers. For STM study, the intercalated MoS_2 was glued to a stainless steel STM sample plate, as shown in Figure 4.10. The glue used was a silver epoxy from Epotek (H21D), made by mixing ten parts of epoxy by mass to one part Ag. A small amount of glue was applied to the sample plate, before placing a cleaved piece of MoS_2 on top and baking this, at 80°C for one hour, to harden the glue and make the MoS_2 stick. An alumina rod, which would be acting as the cleave post, has the glue applied to one end and this end is then fixed on top of the MoS_2, before repeating the 80°C bake.

The mounted and intercalated MoS_2 sample was transferred from the glove box to the STM, via a transition tube holding an Ar atmosphere, before being quickly loaded into the STM vacuum chamber. Once in vacuum, the MoS_2 sample was degassed overnight, by resistively heating it to around 80°C. Just before STM use, the sample was cleaved in-situ, by knocking off the alumina rod laterally using the wobble stick to reveal a fresh, clean layer of MoS_2 (Figure 4.10 (b)). This was carried out on the purpose built cold cleave stage of the STM, cooled to 77 K using liquid nitrogen. Once cleaved, the sample was immediately placed on the STM stage, also held at 77 K.

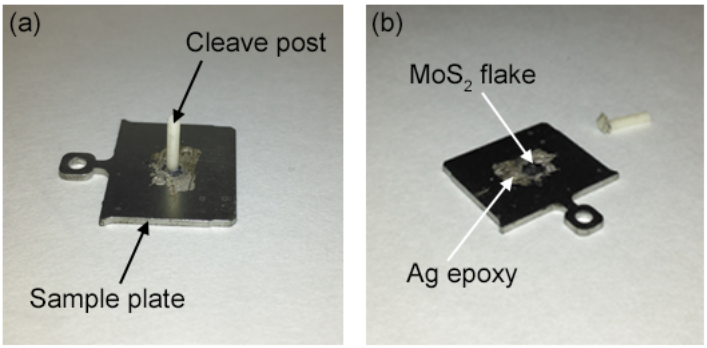

Figure 4.10: A mounted MoS_2 sample (a) pre- and (b) post-cleave. The STM sample plate is of standard size and it has the same dimensions as that of Figure 4.7. This was a test cleave done ex-situ.

4.2 Theory

4.2.1 *2dsch*: A two-dimensional Schrödinger equation solver

The modelling for the dangling bond structures was performed using a 2D Schrödinger equation solver, written by S. Janecek and E. Krotscheck, and described in more detail in Reference [84]. A three-dimensional version (*3dsch*) is also available.

A local, external potential is input to the program, in atomic units, and two-dimensionally simulated probability densities, wavefunctions and energies of low-lying bound states are output. The energies of the bound states are less than the energy of the piecewise potential, and the wavefunctions of the bound states are zero outside the piecewise potential. The computation is carried out across a boxed mesh, where the number of points should be a power of two along each axis. For the DB simulations the run time was on the order of seconds.

The program functions by applying an evolution operator e^{-tH}, containing an approximation of the Hamiltonian H, to a group of trial bound states. Several iterations of this are run until the right degree of convergence is achieved. This is then repeated for increasingly smaller imaginary time steps t, t is usually halved after each stage or repetition. The choice of a complementary time evolution operator and Hamiltonian approximation is what gives the program its speed and quick convergence time.

Increasing the total number of bound states calculated, i.e. computing more states than required with the extra states not necessarily needing to be converged, improves the accuracy for the low-lying states. If the input potential has had a small alteration, then the program can be rerun using the previously calculated bound states as a starting point for initialising the next run, this gives a quicker run time

4.2.2 SEMITIP: Tip-induced band bending calculations

The SEMITIP program was used to simulate the tip-induced band bending (TIBB) present in H-terminated Si(001) samples during STM experiments. The code for the program is written by R. M. Feenstra, it is described in more detail in Refer-

ence [48], and source files are available to download for free from the website [85].

The TIBB is calculated by solving Poisson's equation in three-dimensions, for a hyperbolic shaped tip. A finite difference method is used, whereby an approximation for Poisson's differential equation is run iteratively across a suitable grid, until the requested degree of convergence is achieved. The coordinate system of the grid matches the tip shape and has cylindrical coordinates for the sample region. Section 2.1.4 describes how Poisson's equation is solved in one-dimension, which is essentially the same method used here but in three-dimensions.

In particular, the *uniintsc2* variant of the sixth version of the program was utilised. The program, additionally, outputs the tunnel current as a function of voltage; tunnel currents were calculated using the Bardeen method [86]. This involves a numerical integration of the equation for the tunnel current (Equation 2.26) along the central axis of the tip-vacuum-sample system, where the density of tip and sample states used were those determined from TIBB calculations and the wavefunctions of the tip and sample states were determined by integrating Schrödinger's equation, see Section 2.1.3 for more details.

The computational parameters roughly fall into two categories, one is the material properties of the semiconductor being imaged, silicon in this case, this includes the band gap, dopant binding energies, electron band effective masses and dielectric constant. The other category has parameters describing the experimental set-up, including tip shape, tip-sample separation, contact potential and dopant densities.

Chapter 5

Results: Tunable quantum states of DBs on H-terminated Si(001)

5.1 Excited molecular state of interacting dangling bonds

Figure 5.1 contains a pair of dual bias STM images, i.e. an empty-state and a filled-state image, of a DB dimer on H-terminated Si(001), taken at 78 K. The dimer consists of two DBs on next nearest neighbour sites separated by a distance of 0.77 nm and, consequently, each image features two protrusions, one for each DB.

Figure 5.2 has a set of STM images of the same DB dimer from Figure 5.1. It is shown how under certain image settings and tunnelling conditions, in particular at high sample biases and low tunnelling currents, a third larger, brighter protrusion appears between the two DBs. The observation of this third protrusion or 'excited molecular state' in empty-state imaging has been reported before [2], as described

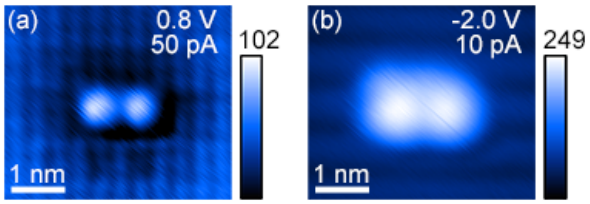

Figure 5.1: (a) Empty-state and (b) filled-state STM images of a DB dimer, a pair of DBs on next nearest neighbour sites separated by 0.77 nm, on H-terminated Si(001) taken at 78 K. Scale bars are in units of picometres.

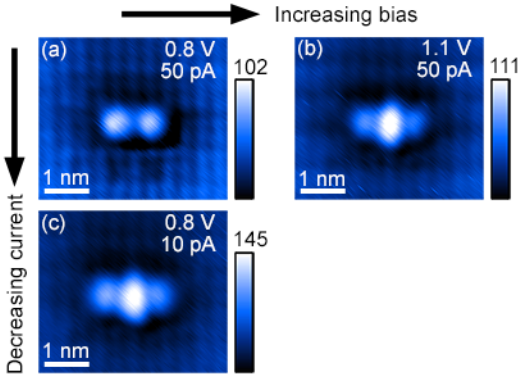

Figure 5.2: The excited molecular state, or lowest energy excited state splitting, of the DB dimer is observed in empty-state STM imaging by either increasing the sample bias, (b), or decreasing the tunnelling current, thereby increasing the tip-sample separation, (c). Scale bars are in units of picometres. These images are of the same dimer as from Figure 5.1.

in Section 3.1.2.2. In order to test the theoretical tip-induced band bending interpretation presented in Section 3.1.2.2, I investigated both the bias and current dependence of a DB dimer. Figure 5.2 contains new, unpublished data where for the first time the excited molecular state is explicitly shown to appear in both a bias and current dependence of the same, single DB dimer.

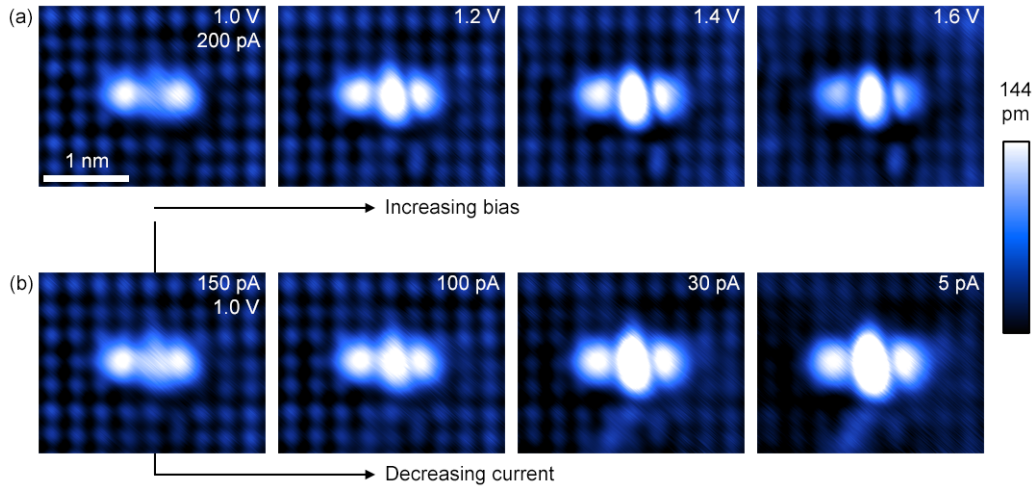

Figure 5.3: (a) A series of empty-state STM images, of increasing sample bias, of a next nearest neighbour DB dimer, DBs are separated by 0.77 nm, displaying the gradual appearance of the excited molecular state. All images were taken at the same current setpoint of 200 pA. (b) A series of empty-state images of decreasing tunnel current of the same DB dimer displays an identical trend of the excited molecular state steadily appearing. The first image of (a) begins the sequence. All images were taken at the same sample bias of 1.0 V.

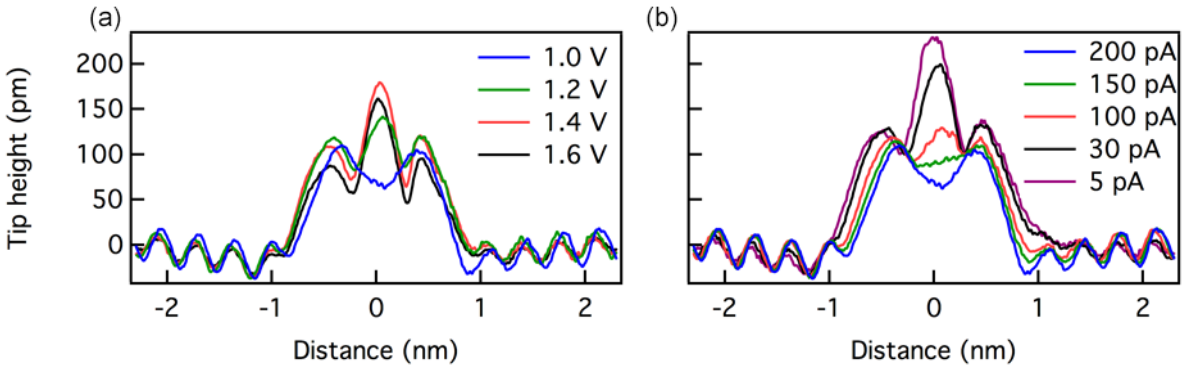

Figure 5.4: A series of topographic line profiles taken across the DB dimer in the STM images of Figure 5.3 as a function of (a) sample bias, current remains fixed at 200 pA, and (b) tunnelling current, bias is fixed at 1.0 V.

Figure 5.3 includes a range of empty-state images showing the excited molecular state of a DB dimer appear in steps for two sequences; for an increasing sample bias and a decreasing tunnelling current, whereas 5.4 has the complementary line profiles for the two sequences. The central lobe of the excited molecular state can clearly be seen to become larger, span a greater area in the images, and of greater brightness, greater height in the line profiles, for higher biases and lower currents. Although it seems that varying the current allows for greater and finer control over the appearance of the excited state, compared to changing the bias, which may offer an explanation to why the former result had been observed before. Maybe the bias should rather be increased in smaller steps of 0.1 V. The atoms on the background surface become less resolved when imaging at greater biases and smaller currents, a result of the STM tip being retracted from the surface at these imaging conditions. An additional point is that in Figure 5.3 (a), the large central protrusion remains similar in size, whereas the constituent DBs of the dimer become dimmer, as the bias is increased from 1.4 V to 1.6 V. This may suggest that the excited molecular state has peaked at a bias between 1.4 and 1.6 V, because in this bias range, the Fermi level of the tip aligns with the excited state, this will be explained later. The difference between raising the bias and lowering the current is discussed and analysed further in Section 5.3.2.

5.2 Modelling the bound states of DB structures

Here, for the first time, the excited molecular state of a DB dimer is supported by two-dimensional simulations (Figures 5.6 and 5.7) and a quantitative analysis featuring calculated energy level diagrams (Figures 5.13 and 5.14).

The potential form of DBs, and deep centre defects in general, is not known exactly, making it difficult to model. Previously, one-dimensional Pöschl-Teller potential wells have been used as approximations to the potential function of DBs [2], more details of which can be found in Section 3.1.2.2. A Pöschl-Teller potential well takes the form of

$$\frac{-\hbar^2\lambda(\lambda-1)}{2m\alpha^2\cosh^2(r/\alpha)}, \tag{5.1}$$

where $\hbar$ is the reduced Planck's constant and m is the electronic mass. The shape of the well is defined by two constants: α, which controls the width, and λ, which controls the depth and hence number of bound states.

To establish a new, two-dimensional model of DBs, the fitting parameters, α and λ, had to be recalculated, ensuring the potential well would continue to hold two bound states close to the electron band edges and within the silicon band gap. The parameters were decided to be 0.3 nm and 3, respectively. To model a DB dimer, or another DB structure, each DB was represented in the relevant position with a circularly symmetric, two-dimensional Pöschl-Teller potential well. An example of this isotropic well is plotted in Figure 5.5.

The Schrödinger equation was solved for the potential wells using the method described in the Section 4.2.1, and individual quantum bound states of the DB struc-

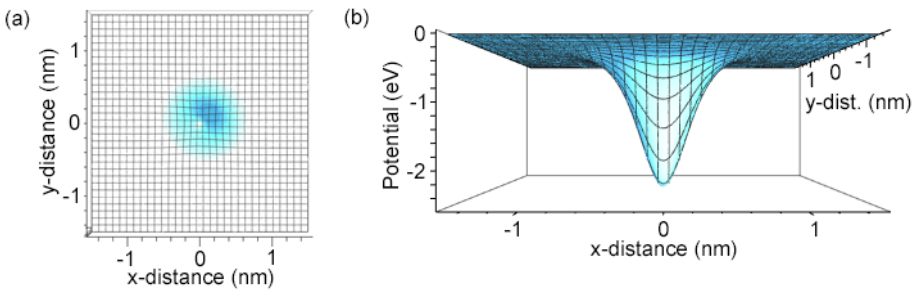

Figure 5.5: (a) Top view and (b) side view of a circularly symmetric, isotropic Pöschl-Teller potential well, used to model a single dangling bond.

ture were output. Two-dimensional simulations have the advantage that they, or a combination of them, can be used to simulate STM images for a direct comparison with experimental data, rather than comparing topographic line profiles, as one would do for a one-dimensional model.

5.2.1 Simulating the bound states of a dimer

The model used to simulate the dimer, shown in Figure 5.6, has a two-dimensional, isotropic Pöschl-Teller potential well with three bound states; a ground state above the valence band and two degenerate excited state below the conduction band, representing each DB. When the two wells overlap and interact the ground state is split into a symmetric and anti-symmetric set. While the excited states are split into four, of which the two lowest energy splittings remain bound, i.e. the other two lie above

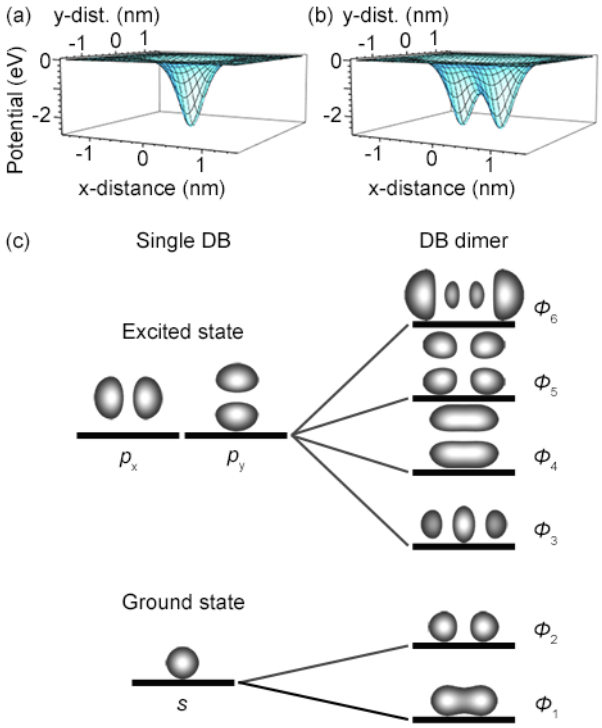

Figure 5.6: Three-dimensional plots of (a) one and (b) two circularly isotropic Pöschl-Teller potential wells ($\alpha = 0.3$ nm and $\lambda = 3.0$), latter is separated by 0.77 nm. Each well is used to model a single DB, therefore the two well system is used to model a DB dimer, see main text for more details. The energy splittings of the two overlapping wells are shown in (c), in order of increasing energy from bottom to top. For the simulated bound state probably densities in (c), λ was taken to be 3.4 to ensure all six states of the dimer remained bound.

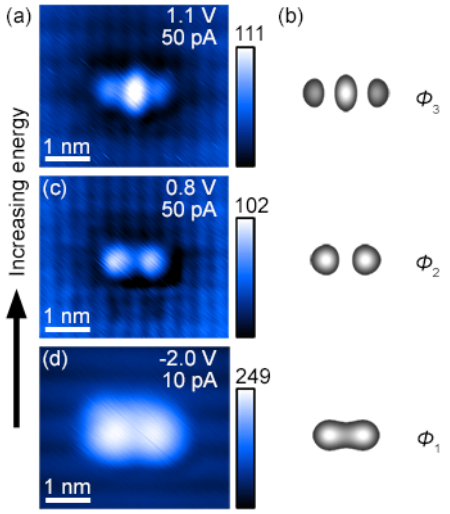

Figure 5.7: (a) STM images of the DB dimer in order of increasing sample bias or energy from bottom to top (scale bars are in units of picometres). (b) Corresponding simulations of the individual bound state probability densities being imaged, taken from Figure 5.6 (c). The three lowest energy bound states of the dimer are observed.

the ionisation potential. It is the lowest energy splitting of the excited state which has a central bright protrusion and we refer to as the excited molecular state.

In Figure 5.7, a comparison is made between the experimental STM images of a DB dimer and the simulated bound states of a dimer. However, they do not map directly one to one, which can be seen in terms of the lateral distance between the protrusions. A weighted linear combination of the individual bound states is required to create a direct simulation of the STM images, and an investigation of this appears in a later section (Section 5.4).

5.3 Quantitative analysis of the excited molecular state appearance

Simulated band bending data is required to draw realistic, calculated energy level diagrams. This will provide better, stronger support to the experimental results presented, rather than the usual sketched band diagrams.

5.3.1 Estimating the input parameters for SEMITIP

In order to be able to calculate the amount of tip-induced band bending present, and its variation with the depth of the semiconductor sample, to produce quantitative energy level diagrams, values for all the parameters have to be found.

Values used for the material properties of the semiconductor sample (silicon) are displayed in Table 5.1 and were found in standard literature sources, for example Sze and Ng [57].

Band gap (at 77 K)	1.166 eV
Donor (As) binding energy	0.054 eV
Acceptor binding energy	0.045 eV
Conduction band effective mass	1.08
Heavy hole effective mass	0.49
Light hole effective mass	0.16
Split-off hole effective mass	0.29
Spin-orbit splitting	0.044 eV
Dielectric constant	11.9

Table 5.1: Properties of silicon used to calculate band bending. The effective masses m^* are units of electron mass m_0. This conduction band effective mass differs from the value used in Section 2.3 because this is the value used for density of state calculations while that value is for conductivity calculations [37].

Whereas values for the parameters describing the experimental set-up are not known exactly, yet they have a greater influence on the TIBB, i.e. their variation causes larger changes in band bending [87]. Estimates were found for these unknown input parameters.

The STM tip shape is defined by two parameters: a tip radius R and a shank opening angle θ, taken to be 50 nm and 90°, respectively. These estimates were based on scanning electron microscope (SEM) images of many tips, created using the method described in Section 4.1.1, several examples of which are shown in Figure 5.8. The SEM images were taken by a summer project student, Muhammad Shu'aib Kamaludin, who I supervised. The average radius of the tips in Figure 5.8 was 46 nm, justifying the choice of 50 nm as the input parameter value.

We can thus estimate realistic values for the experimental parameters (tip-sample separation, contact potential, and donor density) but in order to match our

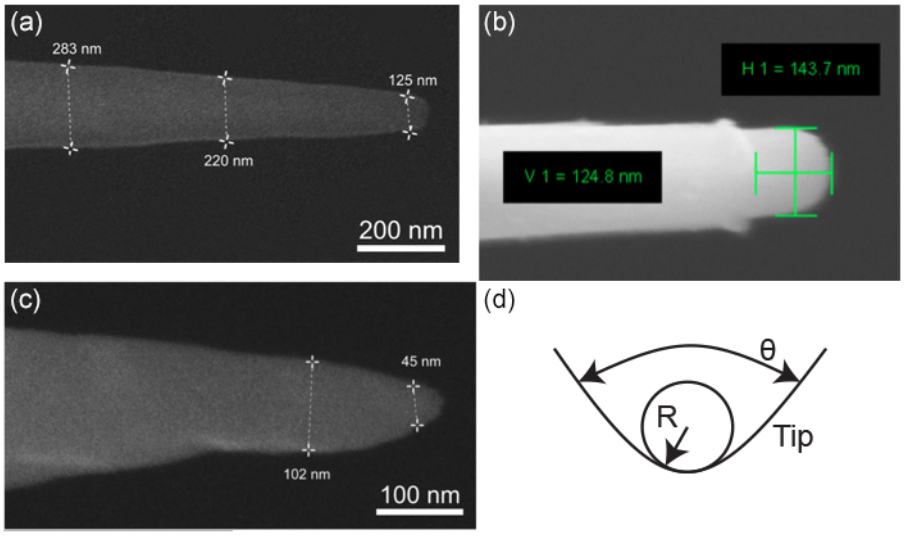

Figure 5.8: (a–c) Scanning electron micrographs of a selection of W tips created using the method described in Section 4.1.1. The tip radii were 55 nm, 67 nm, and 15 nm, respectively. The SEM images were taken by summer student Muhammad Shu'aib Kamaludin. (d) A schematic diagram showing how the tip radius R and shank opening angle θ define the tip shape.

simulations with experiment we have performed fitting between the experimental and theoretical tunnelling currents.

The contact potential ϕ_{CP} is the difference between the work function of the metal tip and the equivalent of the semiconductor sample, each is illustrated in Figure 5.9, and it is given by the following equation:

$$\phi_{CP} = \phi_W - (\chi_{Si} + (\mathrm{CBM} - \mathrm{E_F})),$$

where ϕ_W is the work function of W (4.80 eV), χ_{Si} is the electron affinity of Si (4.05 eV), CBM is the conduction band minimum energy and $\mathrm{E_F}$ is the Fermi energy. $\mathrm{CBM} - \mathrm{E_F}$ can be assumed to be almost zero, since we are dealing with a highly doped n-type semiconductor, this gives an expected contact potential of 0.75 eV.

I ran many calculations to investigate changing the tip-sample separation, contact potential and donor density parameters affected and varied the spectroscopy simulations, graphs of current versus voltage, output from SEMITIP. The results of which are displayed in Figure 5.10.

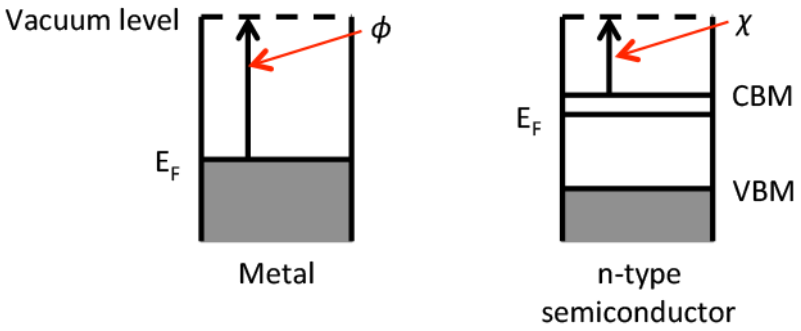

Figure 5.9: Schematic energy level diagrams illustrating the work function ϕ of a metal (left), the minimum energy required to remove an electron, and the equivalent of an n-type semiconductor (right). χ refers to the electron affinity, E_F is the Fermi level, CBM is the conduction band minimum and VBM is the valence band maximum.

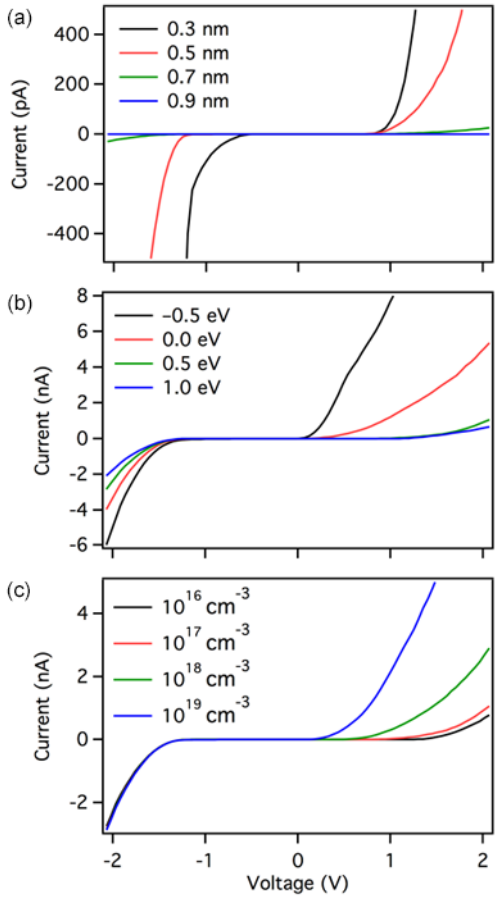

Figure 5.10: Plots of tunnel current against voltage, output from SEMITIP, for varying tip-sample separation (a), contact potential (b) and donor density (c). In the black curve of plot (b), there is some structure, or more specifically a kink, and the reason behind this is given in the main text.

In Figure 5.10 (a), I show the calculated tunnel current for different tip-sample separations. We see that increasing the tip-sample separation decreases the tunnel current, giving a flatter current-voltage curve. The rise in current for the electronic bands is less steep. The changes are drastic due to the current's exponential dependence on the tip-sample separation.

In Figure 5.10 (b), I show the calculated tunnel current for different contact potentials. We see that increasing the contact potential increases the amount of upward band bending present when the Fermi level of the tip becomes aligned with the Fermi level of the sample. This is the situation that occurs for a positive contact potential, see Figure 5.11 (a), where the tip Fermi level falls below the sample Fermi level, and as a result the onset of tunnelling into the conduction band now appears at a higher voltage. In other words the tip Fermi level has to be raised to a higher energy to achieve elastic tunnelling into the conduction band. For the negative contact potential case, see Figure 5.11 (b), downward band bending is present when the two Fermi levels are aligned in the zero bias case and the resulting kink in the current-voltage plot occurs at the crossover between downward and upward TIBB. The kink occurs at the bias for the flat band condition, where no band bending is present.

In Figure 5.10 (c), I show the calculated tunnel current for different donor densities. We see that increasing the donor density decreases the rate of upward TIBB and the appearance of the conduction band is brought on at lower voltages, but unsurprisingly it has no effect on the valence band. The former statement is proven by considering the equations for the charge density of a semiconductor (Equation 2.30) and the electric field at the surface (Equation 2.34), found in Section 2.1.4. We see that a higher donor density increases the charge density which, in turn, increases the electric field. Equation 2.35 shows that for a greater electric field, and the same tip potential, less TIBB would be present.

Following this investigation, estimates were found for the tip-sample separation (0.5 nm), contact potential (0.5 eV) and donor density (10^{17} cm^{-3}) in our experiment by fitting tunnel current against voltage graphs to scanning tunnelling

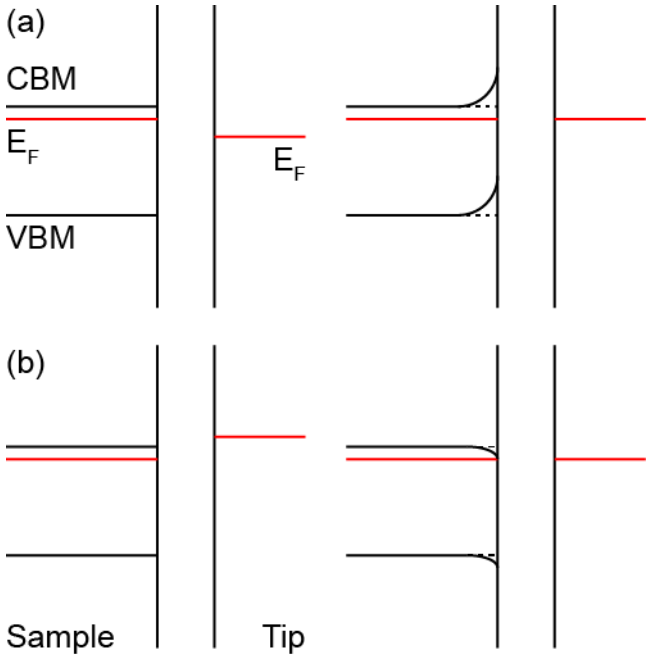

Figure 5.11: Energy level diagrams displaying the band bending induced by (a) a positive contact potential and (b) a negative contact potential. CBM refers to the conduction band minimum of the semiconductor sample, VBM to the valence band maximum, and the red lines represent the Fermi levels (E_F) of the sample and tip.

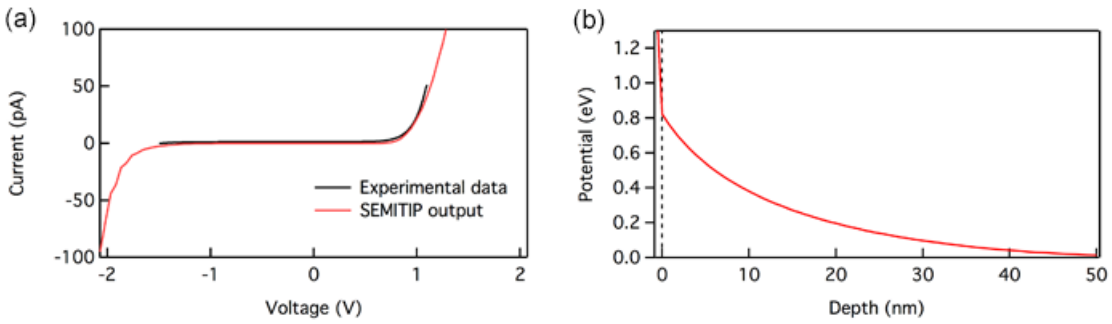

Figure 5.12: (a) The current versus voltage graph output from SEMITIP is found to match experimental spectroscopy data for a combination of $s = 0.5$ nm, $\phi_{CP} = 0.5$ eV and $n = 10^{17}\text{cm}^{-3}$. The experimental curve has a limited voltage range because higher bias voltages lead to unwanted H-desorption. (b) Using these estimates, SEMITIP was run to give the potential as a function of depth for a sample bias of 0.8 V. The sharp potential drop occurs across vacuum gap between the tip and sample and the dashed $x = 0$ line is the sample surface.

spectroscopy data — see Figure 5.12 (a).

Relative changes in tip height when changing bias or current settings during imaging were measured from the resultant changes in line profiling of the topogra-

phy, and subsequently taken into consideration.

This combination of three parameters values may be different from our initial predictions but these values are acceptable, as explained next.

This contact potential of 0.5 eV differs from our initial, expected value of 0.75 eV, predicted earlier. However, it is not unusual for the contact potential to be different because the work function of W changes with the shape and crystal face of the tip [43], and it can vary from 4.32 to 5.22 eV [88]. Correspondingly, the contact potential falls in the range from 0.27 to 1.17 eV.

The resistivity r of the Si wafer is given by the manufacturer (0.00275 Ωcm), using this value the donor concentration n was determined;

$$n = \frac{1}{e\mu r} = 2.82 \times 10^{19}\text{cm}^{-3},$$

where e is electron charge and μ is mobility (80.4 $\text{cm}^2(\text{Vs})^{-1}$). However, surface preparation processes, in particular the high temperature flash anneal (see Section 4.1.2), reduces n by several orders of magnitude [82]. The high temperature preparation causes donors to diffuse out of the surface, or at least build up at the surface, and repeated flashing removes the top layers thereby reducing n. Therefore, a donor density of 10^{17} cm^{-3} seems reasonable.

The tip-sample separation of 0.5 nm is within range for semiconductor measurements [89, 43].

We use these parameters to calculate the potential or TIBB as a function of depth, a plot of which is shown in Figure 5.12 (b). The potential drop within semiconductor sample ($x \geq 0$) gives the curvature of the electronic bands and it was used to produce the quantitative energy level diagrams in Figures 5.13.

5.3.2 The gating effect of the bias & current variables

All subsequent energy level diagrams in this chapter are calculated results based on simulated band bending results, produced using the method described in the previous section. Examples of which follow in Figures 5.13 and 5.14, and they are used to explain the appearance of the DB dimer's excited molecular state.

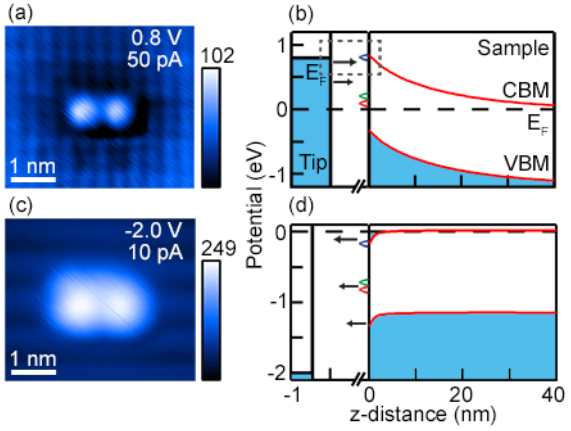

Figure 5.13: Energy level diagrams (b,d) corresponding to dual-bias imaging (a,c) of the dimer, where the tip-induced band bending has been calculated using SEMITIP and the dimer's bound states have been schematically represented. The colour scale bars of the images are in units of picometres. CBM refers to the conduction band minimum, VBM is the valence band maximum, and E_F is the Fermi level. The red, green, and blue bound states refer to ϕ_1, ϕ_2, and ϕ_3, respectively, as defined in Figure 5.6 (c).

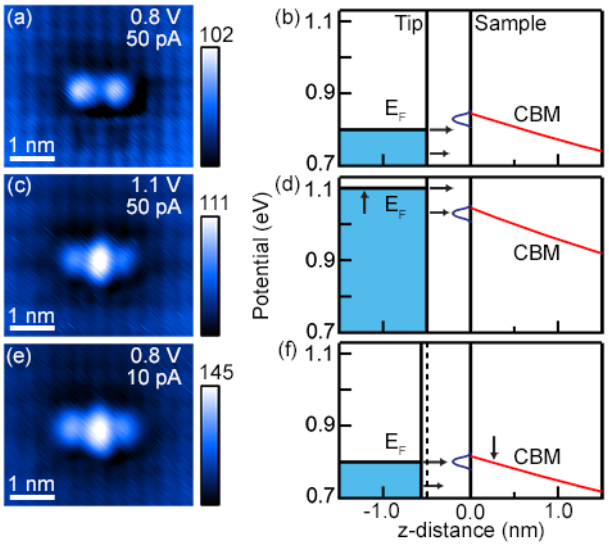

Figure 5.14: (b,d,f) Energy level diagrams zoomed in on the region around the excited molecular state, depicted in blue, which sits approximately just below the CBM. Indicated by a grey dashed box in Figure 5.13 (b). This excited state is observed when it is made to align with or brought below the tip Fermi level by either increasing bias, (d) and image (c), or by decreasing the current, (f) and image (e). The colour scale bars of the images are in units of picometres.

In empty-state imaging, the excited molecular state, which is the lowest energy splitting of the excited state with the large protrusion between the DBs, can only be observed when it is aligned with or brought below the Fermi level of the tip. Due to

the fact the electron tunnelling, or tunnelling matrix element, is at its greatest about this point and more prominent for states close to and below the Fermi level, refer to Section 2.1.2 for more details.

Figure 5.13 contains calculated energy level diagrams showing upward band bending for the empty-state image and downward band bending for the filled-states image, as expected. In the empty-states case (Fig. 5.13 (a,b)), the excited state remains above the tip Fermi level and, thus, it is not observed in the STM image. In the filled-states case (Fig. 5.13 (c,d)), there is much less band bending since the conduction band is crossing the Fermi level of the sample. Tunnelling occurs from the sample to the tip, therefore tunnelling is greatest for states at the sample Fermi level, such as the excited state, but it is not observed in the image because it is obscured by tunnelling from the many occupied valence band states.

Figure 5.14 shows this alignment between excited molecular state and tip Fermi level is achievable, in the empty-states, using the experimental parameters of sample bias and tunnel current as gates, in particular under a high bias or a low current setting.

Increasing the bias raises the tip Fermi level above the excited molecular state, which is located just below the conduction band minimum (Fig. 5.14 (d)). Allowing electrons to resonantly tunnel from the tip to the excited state and allowing it to be observed in STM imaging (Fig. 5.14 (c)).

Alternatively, decreasing the current, which increases the tip-sample separation and in turn reduces the upward tip-induced band bending, lowers the bound states of the DB dimer. This way the excited molecular state can be brought below the tip Fermi level (Fig. 5.14 (f)) and it is observed in STM imaging (Fig. 5.14 (e)). It can be seen from the energy level diagrams in Figure 5.14 that adjusting the position of the excited molecular state by decreasing the current, gives more subtle changes, allowing the excited molecular state and the tip Fermi level to become exactly aligned and giving a stronger appearance in imaging.

This can also be used to explain the data from Figures 5.3 and 5.4, which have been obtained for another dimer, where the excited molecular state appears stronger

when the current is varied rather than the bias and the excited state has already started to diminish for the greater biases as the tip Fermi level passes the excited state.

5.4 Two-dimensional dangling bond structures & symmetry effects

Two-dimensional DB structures containing three and four DBs, 'trimers' (see Figures 5.16 to 5.18), and 'tetramers' (see Figures 5.21 to 5.27), respectively, have been created and studied.

The Methods Section 4.1.2 describes how these structures were fabricated, one DB at a time, in a controlled fashion. Figures 5.15 and 5.20 contain a sequence of images showing the step-by-step creation of a DB trimer and tetramer, respectively.

The reason behind the investigation of two-dimensional DB structures was to see how this change would influence the excited states of the structure; if the excited molecular state would remain and if it too would extend to two-dimensions. Also of interest was how the excited molecular states would behave in response to covering more of the silicon surface and how the dimer reconstruction would affect the appearance. Naturally, the next step progressing from DB dimers would be to make structures with 3 DBs, and then 4 DBs. The DB trimer presented here has been made across two dimer rows, more importantly across a trough region. The two

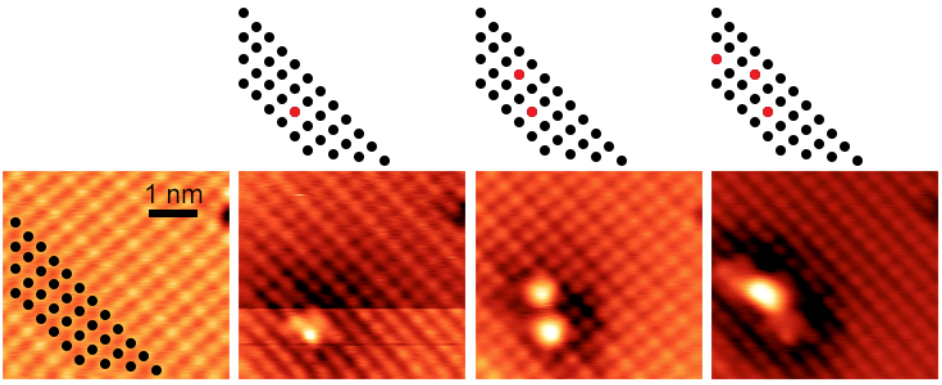

Figure 5.15: A sequence of STM images showing the step-by-step creation of a DB trimer structure on H-terminated Si(001). All the images were taken at a setting of 1 V and 300 pA.

tetramers presented here differ in length, but additionally in rotation with respect to the silicon surface, to investigate the effects of symmetry.

Many difficulties were encountered in relation to constructing the DB structures. Common problems faced included the wrong hydrogen atom being removed, resulting in the DB being in the wrong position, and more than one hydrogen atom being removed, resulting in a unwanted cluster of DBs. Such mistakes were typically due to a double tip and could not be reversed, therefore a new structure would have to be built on another clean, passivated surface region.

Similar issues can be observed in Figure 5.15, where the continuous voltage pulsing to create the DBs has resulted in a loss of image quality or the formation of a double tip. Signalled by the varying appearances of the DBs. Such strong tip changes mean that the voltage or duration of the pulse required to remove a DB would be different. In the case of the trimer, the tip was improved very carefully with small voltage pulses in a region some distance away from the DB structure to avoid any damage to the structure, before taking the images in Figure 5.16.

These structures also exhibit bright protrusions between DBs, or excited molecular states, as observed and discussed before for dimers. These two-dimensionally extended excited states were seen for the first time and, interestingly, they appear in a more complex form since they are a combination of several individual bound states.

Complementing DB dimers, the bias and current variables of the STM act as gates controlling tunnel access to higher energy, excited bound states and thus which states contribute to the image. In this section we prove that the excited molecular orbitals of these 2D DB structures are observed at high biases and low currents, consistent with dimers.

5.4.1 Trimers

I will now go on to describe the properties of the DB trimer shown in Figure 5.15. Figure 5.16 shows bias dependent STM images of this trimer.

In the STM images of Figure 5.16, the ground state of the trimer is observed in the filled-states image and the empty-states images taken at 1.0 V and 300 pA. For

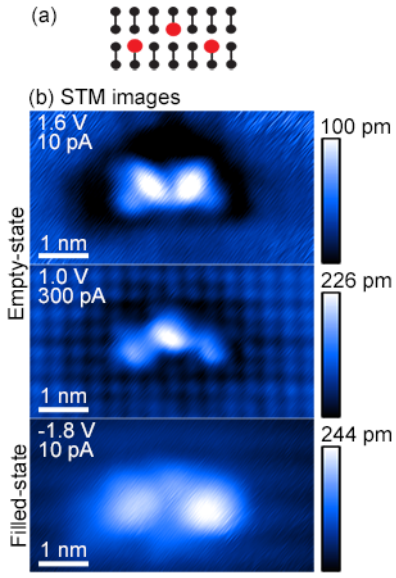

Figure 5.16: (a) Schematic diagram of a DB trimer. The red circles denote DBs and the black circles denote H-terminated Si atoms. (b) STM images of the trimer. In the filled-state image, the central DB has a dimmer, smaller appearance than the other two, making it difficult to observe. Figure 5.15 displays the fabrication of this trimer.

the former image, the DBs appear in a bright–dim–bright pattern, and in the latter, they appear in the opposite dim–bright–dim pattern. The high bias, low current empty-state image, taken at 1.6 V and 10 pA, reveals the excited state of the trimer. Two bright protrusions have appeared between the DBs; there are two protrusions since there are three DBs. The central DB is still present, but the view of it is obscured by the the presence of the two protrusions.

There is a slight asymmetry regarding the STM images of the ground state of the trimer, the right/left DB appears brighter in the filled-/empty-states, because of defects, dangling bonds and tungsten deposits, in the surrounding vicinity (about 8 nm away). The defects were unintentionally created when voltage pulsing to improve tip quality.

Figure 5.17 contains two-dimensional simulated individual bound states and associated energies, output by the Schrödinger equation solver, for the DB trimer. A Pöschl-Teller potential well was used to model each DB of the trimer, as described for the dimer in Section 5.2. Five bound states were output, the first three being ground state splittings and the latter two being excited state splittings.

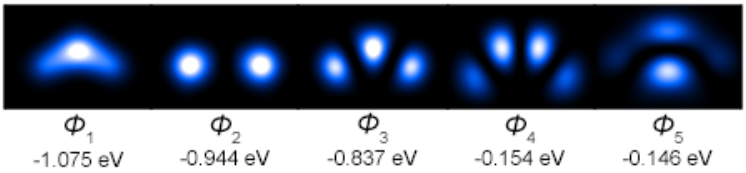

Figure 5.17: Images of two-dimensional simulated individual bound state probability densities for three isotropic Pöschl-Teller potential wells in the appropriate positions to model the trimer. The first three bound states, equal to the number of DBs, are ground state splittings and the latter two are excited state splittings, the third excited state splitting is not bound.

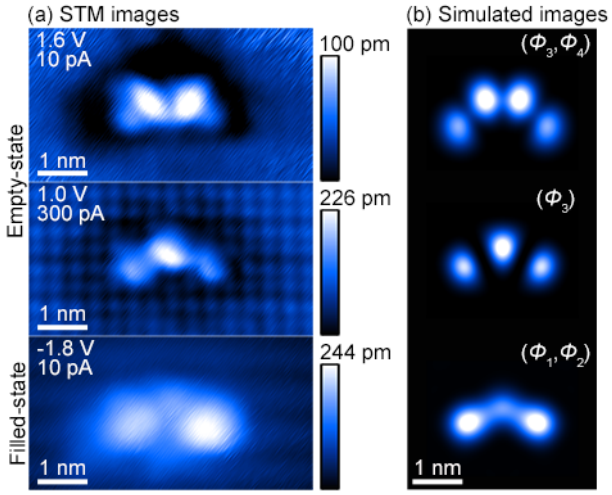

Figure 5.18: (a) STM images of the trimer. (b) Simulated STM images of the trimer. Linear combinations of the bound states were used to create the simulated images. Bottom simulation(ϕ_1, ϕ_2), centre simulation(ϕ_3), and top simulation(ϕ_3, ϕ_4).

Linearly combining certain individual bound states, using an approximation for the tunnelling matrix element, gave the ability to replicate the STM images. The trimer was successfully simulated this way, and a comparison is made between the experimental and simulated images in Figure 5.18.

The bound states ϕ_n were linearly combined using the expression

$$\frac{\Sigma_n c_n |\phi_n|^2}{\Sigma_n c_n},$$

with the coefficients given by $c_n = \exp(kE_n)$, where E_n is the energy value associated with the bound state and $k = 1.4$. This weighting function, that is used to give the coefficients, is plotted in Figure 5.19 and it is a suitable approxima-

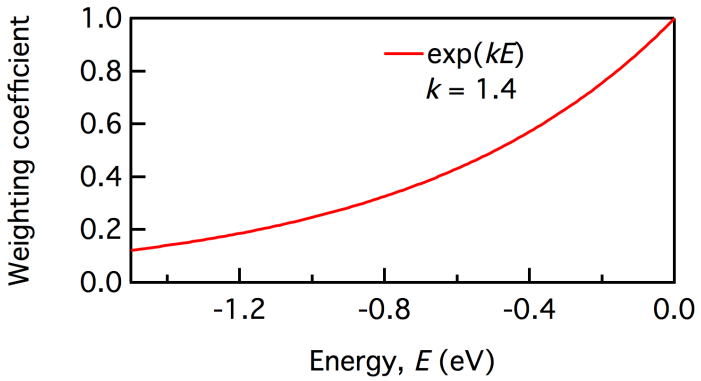

Figure 5.19: A plot of the weighting function, used as an approximation of the tunnelling matrix element when combining the individual bound state probability densities to create the simulated STM images.

tion for the tunnelling matrix element. That is because firstly, it is an exponential like Equation 2.23 and it gives a larger coefficient, and thus greater weighting, to the higher energy individual bound states because electron tunnelling is greater for states closer to the Fermi level, refer to Section 2.1.2 for more details. The value of k was chosen to ensure the ground state splittings would receive an appreciable weighting and have a worthy inclusion in the linear combinations. The same function is used to simulate empty- and filled-state images, since in both cases the tunnelling is prominent for the higher-energy bound states, closer to the tip and sample Fermi levels, respectively. Moreover, the same weighting function is used throughout this chapter to simulate the STM images for all the 2D DB structures.

Haider *et al.* [15] and Hitosugi *et al.* [18] have made similar observations to the ground state of the trimer in their work on coupled DBs (Figure 3.6 in Section 3.1.2) and DB wires (Figure 3.10 in Section 3.1.3), respectively, in the sense that adjacent DBs alternate between bright and dim. Hitosugi, in particular, has additionally seen the appearance of a DB change from bright to dim, or vice versa, when switching between empty- and filled-states imaging. Whereas they explain their results with a changing in the DB electron occupation or Jahn-Teller distortions, respectively, our model of including the tunnelling matrix element when combining bound states has successfully reproduced these ground state patterns and proven the existence of the excited state.

5.4.2 Tetramers

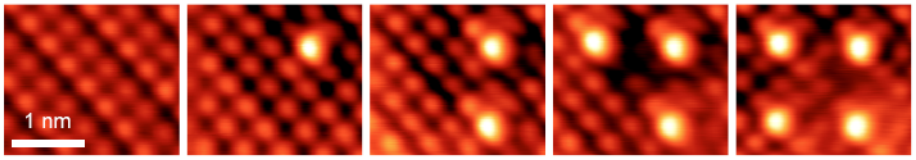

Figure 5.20: A sequence of STM images showing the step-by-step creation of a DB tetramer structure on H-terminated Si(001). All the images were taken at a setting of 1 V and 300 pA.

Tetramers were investigated to study how the symmetry, or rotation, of the DB structure, with respect to the background surface reconstruction, could control the ordering of the bound quantum states. Figure 5.20 displays the creation of one of the tetramers studied.

Figures 5.21 and 5.22 contain empty-state STM images of two DB tetramer structures. Tetramer I (Fig. 5.21) has a side length of 0.77 nm and it runs parallel to the dimer rows, whereas tetramer II (Fig. 5.22) has a side length of 1.089 nm and it is rotated 45° with respect to the dimer row direction. For tetramer I, the excited molecular state is observed at a low tunnel current setting, and for tetramer II, the

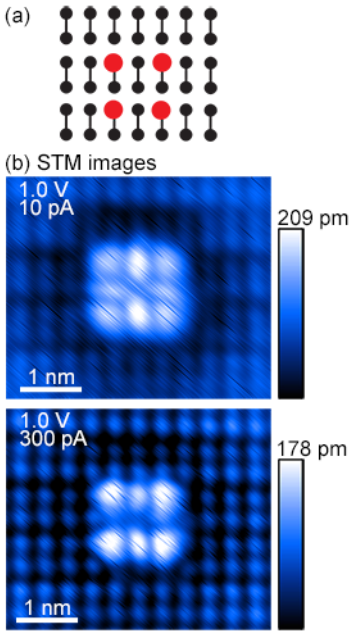

Figure 5.21: (a) Schematic diagram of a DB tetramer: tetramer I. The red circles denote DBs and the black circles denote H-terminated Si atoms. (b) STM images of tetramer I, which has a side length of 0.77 nm.

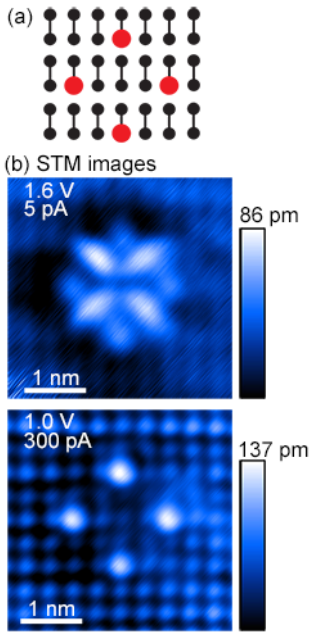

Figure 5.22: (a) Schematic diagram of a second DB tetramer: tetramer II. The red circles denote DBs and the black circles denote H-terminated Si atoms. (b) STM images of tetramer II, of side length 1.089 nm. Figure 5.20 displays the fabrication of this tetramer.

excited state is observed at high sample bias and low tunnel current settings.

Figures 5.23 and 5.24 contain the simulated individual bound states, with their energies, for tetramers I and II, respectively. The simulations, run using the Schrödinger equation solver, produced eight bound states ϕ_1 to ϕ_8 for both tetramers, the first four associated with the ground state and the latter four associated with the first excited state.

However, the individual bound states of the tetramers were not observed experimentally to appear in the order shown in Figures 5.23 and 5.24. ϕ_5 was the only

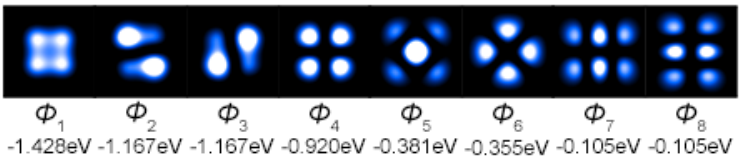

Figure 5.23: Two-dimensional simulated individual bound state probability densities for four isotropic Pöschl-Teller wells, each one representing a DB, in the appropriate positions to model tetramer I. The first four states, equal to the number of DBs, are ground state splittings and the latter four are splittings of the first excited state.

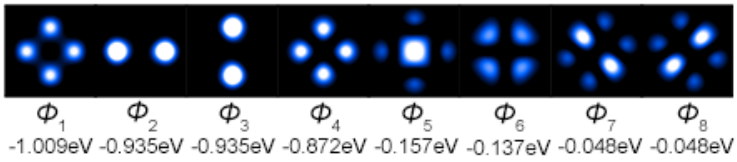

Figure 5.24: Two-dimensional simulated individual bound state probability densities for four isotropic Pöschl-Teller wells, each one representing a DB, in the appropriate positions to model tetramer II. The first four states, equal to the number of DBs, are ground state splittings and the latter four are splittings of the first excited state.

state never seen under STM imaging, for either tetramer, suggesting it should be the highest energy bound state, and for tetramer I, the state ϕ_7 was imaged before ϕ_6. Therefore, the order is incorrect and the model, i.e. the potential wells representing the DBs, have to be adjusted.

The ordering of the individual bound states displayed in Figure 5.23 and 5.24 is only true if the potential wells are in free space, but this is not the case because the (2×1) surface reconstruction of the Si(001):H surface, and the presence of dimer rows, applies a background potential.

In this case, another, more suitable representation was needed for each DB; one which also reflects the asymmetry of the substrate surface. The anisotropic well chosen was cross-shaped and extended along the x-direction, the dimer row direction. The well is displayed in Figure 5.25. It serves to be a truer reflection of the dimer rows and the (2×1) surface reconstruction of the Si(001) surface.

Using the anisotropic wells instead changed the order of the individual bound states to agree with experiment. For tetramer I, the degeneracy between ϕ_7 and ϕ_8 is broken and the excited state splittings are reordered ϕ_7, ϕ_6, ϕ_8, and ϕ_5. This correct ordering was obtained when the modelling was run with anisotropic wells, which had a cross-shaped cross-section extended along the dimer row direction, see Figure 5.25 (c). In addition, ϕ_5 was never observed in experiment but ϕ_7, ϕ_6, and ϕ_8 all were. For tetramer II, ϕ_5 was again considered to be the highest energy bound state. However this time the degeneracy between ϕ_7 and ϕ_8 was not broken since this tetramer is more symmetrical, in the sense that all four side lengths go across a trough and dimer region.

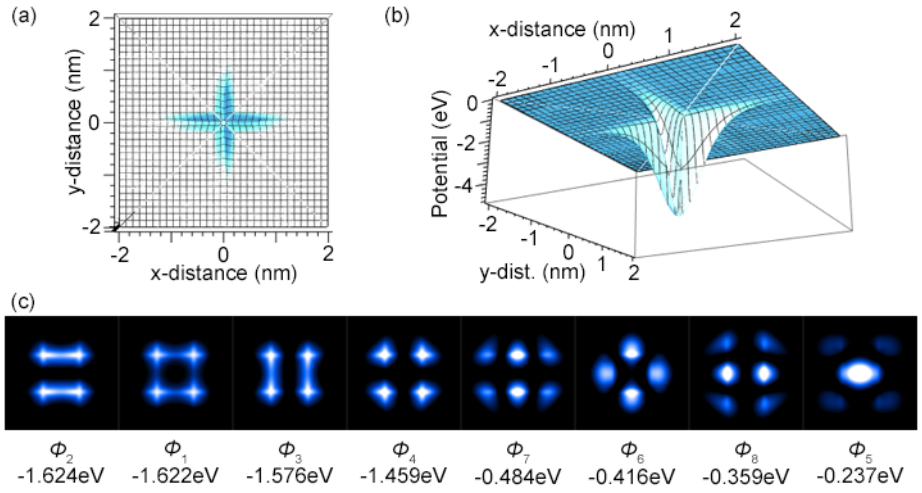

Figure 5.25: Simulation run for four anisotropic potential wells in the formation of a square with a side length of 1.089 nm. (a) Top view and (b) side view of a three-dimensional plot of one of these anisotropic Pöschl-Teller potential wells, displaying the cross shape of the well, which is slightly extended in the x-direction. (c) The individual bound state probability densities, with associated energy eigenvalues, output for the four anisotropic well structure.

The anisotropic well used is plotted in Figure 5.25 (a,b). It was constructed by the summation of two Pöschl-Teller potential wells, each described by Equation 5.1. The two constants α and λ were chosen to be 0.471 nm and 5.8, respectively, for both wells. In two-dimensions, r takes the following form:

$$r^2 = (A \times x)^2 + (B \times y)^2.$$

The constants A and B were taken to be 0.89 and 6, respectively, for one well and 6 and 1, respectively, for the other well. The values for α, λ, A, and B were chosen to make sure the anisotropic potential well retained the same number of bound states at the same energies, as that of the isotropic well. The values of A and B were intentionally different for the two individual wells, to create the anisotropy and ensure that the cross-section of the well was indeed a cross shape, but extended in the x-direction.

The symmetric, isotropic potential wells bring out the basic underlying physics and are used to simulate all the STM images in Figures 5.26 and 5.27. Perhaps a more sophisticated theory is needed to really take into account the substrate asym-

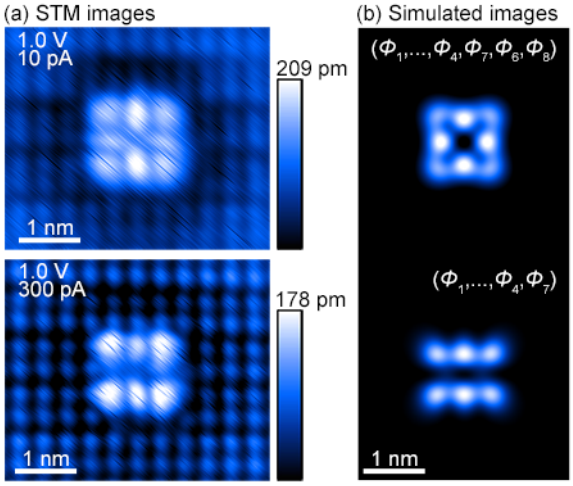

Figure 5.26: (a) STM images of tetramer I, which has a side length of 0.77 nm. (b) Simulated STM images of tetramer I. Bottom simulation$(\phi_1,\phi_2,\phi_3,\phi_4,\phi_7)$ and top simulation$(\phi_1,\phi_2,\phi_3,\phi_4,\phi_7,\phi_6,\phi_8)$, created using the individual bound states from Figure 5.23.

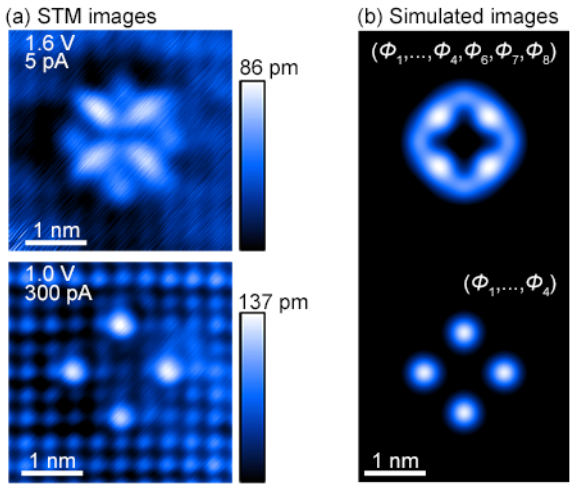

Figure 5.27: (a) STM images of tetramer II, of side length 1.089 nm. (b) Simulated STM images of tetramer II. Bottom simulation$(\phi_1,\phi_2,\phi_3,\phi_4)$ and top simulation$(\phi_1,\phi_2,\phi_3,\phi_4,\phi_6,\phi_7,\phi_8)$, created using the individual bound states from Figure 5.24.

metry.

The individual bound states produced from symmetric, isotropic potential wells in Figures 5.23 and 5.24 were linearly combined, using an approximation for the tunnelling matrix element, to simulate the STM images, as done for the trimer in the previous section.

With regards to the excited molecular state of tetramer I, displayed in the top

STM image of Figure 5.21 (b), the four bright protrusions between the DBs are not of equal intensity. The two protrusions in the direction across the dimer rows are slightly dimmer, since they sit directly above a trough region. This could not be replicated in the simulations since only local potentials can be input into the Schrödinger equation solver, and not the potential of the surface reconstruction. This is another reason why it would be advantageous to be using anisotropic potential wells to represent DBs, it would just require an additional layer of asymmetry. Whereas for the second tetramer, the four bright protrusions in the excited molecular state are all of equal intensity since the side lengths are more identical i.e. they all span a dimer and trough region.

5.5 Using a proximity effect

In Figure 5.28, the appearance of the excited molecular state of two identical DB trimers, in Fig. 5.28 (a,b), varies significantly, due to one of the trimers, in Fig. 5.28 (b,d), having a defect located nearby. The defect appears as a bright feature in the top left corner of the STM image in Fig. 5.28 (d). The exact nature of the defect is unknown but its bright, protruding appearance suggests tungsten deposits or more dangling bonds, created while voltage pulsing, but if it is the latter it may

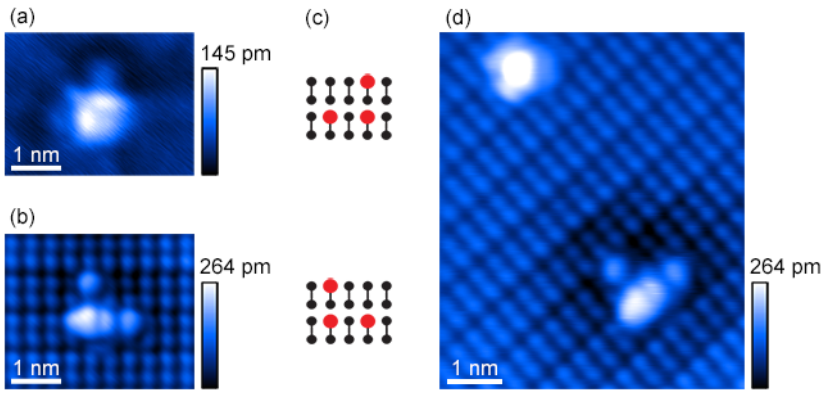

Figure 5.28: (a,b) STM images displaying the excited molecular state of two DB trimers (image settings: (a) 1.6 V, 2 pA and (b) 1.0 V, 500 pA). (c) Schematic diagram of the two trimers. The red circles denote DBs and the black circles denote H-terminated Si atoms. The two trimers are identical structures aside from being mirror images, however their excited states appear vastly different. This is explained by (d) the larger scale STM image of (b), where a nearby defect seems to have perturbed the potential landscape ((d) 1.0 V, 100 pA).

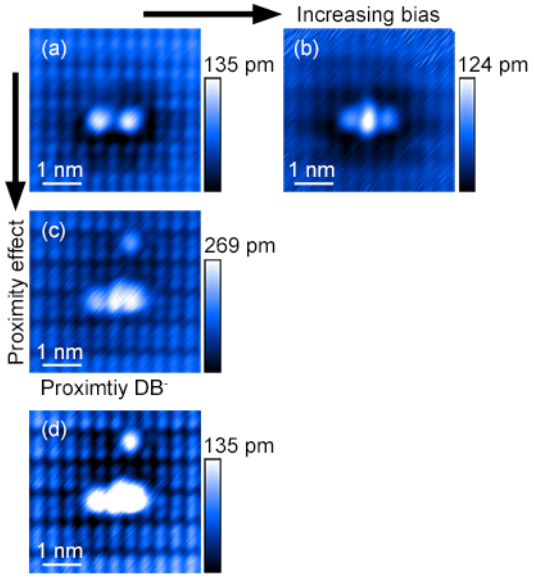

Figure 5.29: (a) STM image of a DB dimer, a pair of DBs on next nearest neighbour sites separated by 0.77 nm (image settings: 1.0 V, 10 pA). (b) The excited molecular state of the dimer is observed at a higher sample bias setting (1.6 V, 10 pA). (c) The appearance of the excited molecular state is also induced by the creation of an additional DB in close proximity, rather than having to change the bias or current (same settings as (a): 1.0 V, 10 pA). (d) Identical to (c) but its colour scale bar and z-range matches that of (a), this is to clarify that the dimer and proximity DB sit within the same depression. Therefore the proximity DB is close enough to be considered negatively charged while the tip scans over the dimer.

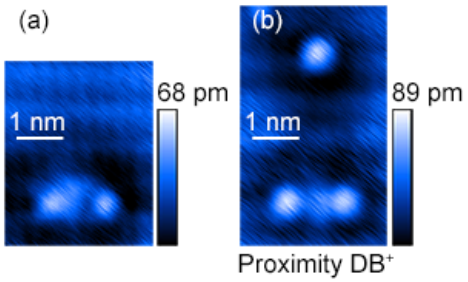

Figure 5.30: (a) STM imaging of a DB dimer with a larger separation distance of 1.155 nm, it has two Si-H sites in between (1.6 V, 5 pA). (b) The excited molecular state appears when another DB is made nearby and image settings remain the same (1.6 V, 5 pA). But this time the proximity DB is far enough from the dimer to be positively charged, it has its own surrounding depression which does not overlap with the depression of the dimer.

already have been present from an incomplete H-termination.

It was investigated how the excited molecular orbital of a DB dimer is influenced by the addition of an single DB in close proximity. Figures 5.29 and 5.30

give two more examples where a 'proximity' DB has altered the appearance of a small DB cluster, while the bias and current settings have remained constant.

In part (a) and (b) of Figure 5.29, the excited molecular state of a DB dimer is observed to appear as the sample bias is increased. This trend is in agreement with earlier bias dependence work on dimers in Section 5.1. This trend occurs because increasing the bias raises the Fermi level of the tip above the excited molecular state, and, thus, electrons can tunnel into the excited state and it is observed in STM imaging. See Fig. 5.14 for more details. However, in part (c) of Figure 5.29, the excited molecular state has appeared without changing the bias, or current, settings. Therefore, the presence of the proximity DB has allowed electron tunnelling into the excited molecular state without the need for raising the tip Fermi level. This suggests this proximity effect is lowering the dimer's bound states in energy, enabling the excited state to become aligned with or brought below the tip Fermi level.

Initially this was surprising, because it is known that DBs are negatively charged, while the STM tip is passing over, whether it be in empty- or filled-states mode [2]. Therefore, based on band bending considerations, one would predict the opposite, the dimer's states being pulled up due to additional upward band bending induced by the negatively charged proximity DB. Hence, the proximity DB is not having an electrostatic effect on the dimer. This disagreement between experiment and band bending predictions was the same situation faced by Lee and Gupta [28], see Section 3.3.

However, looking in more detail into the position of the proximity DB with respect to the dimer, we find two different cases. In Figure 5.29, the proximity DB and dimer sit within the same depression, whereas in Figure 5.30, the proximity DB is far enough to have a separate depression to the dimer.

In Section 2.3.2, it is described how a negatively charged defect will appear with a surrounding dark depression in empty-state STM imaging, because the defect has induced additional, localised upward band bending. This decreases the number of sample states for electrons to tunnel into, thus the tunnel current decreases and the surface appears at a lower height. Therefore, in Figure 5.29, the proximity DB

is negatively charged while the tip scans over the dimer.

In Figure 5.30, the proximity DB is considered positive as the tip passes over the dimer, because when the tip is in this region, the upward tip-induced band bending has raised the proximity DB state above the sample Fermi level and it becomes unoccupied. But the band bending is not great enough to isolate charge on the DB, which is the scenario for the first proximity case. The two different charge states are a consequence of the double barrier tunnel junction present in empty-state imaging [16, 2], visit Section 3.1.1 for more information.

In conclusion, the proximity effect occurs regardless of the proximity DB's charge state; for that reason it can not be explained by Coulombic or band bending effects. Referring to Section 3.3, this disagrees with the interpretations presented by Lee and Gupta [28], and Pitters *et al.* [26]. Additionally, the interpretation of Kumagai *et al.* [27] will not work here, because the much weaker van der Waals interaction is not expected to play a part between two charged defects. This leaves us to consider the explanation presented by Fölsch *et al.* [24].

Comparing tetramer II to tetramer I, Figure 5.24 to Figure 5.23, we see that as the DBs of the structure are brought closer together the energy eigenvalues of the individual simulated bound states decrease to a larger negative magnitude. The energy of the observed excited state splittings, ϕ_6, ϕ_7, and ϕ_8, decreases from -0.137 eV and -0.048 eV to -0.355 eV and -0.105 eV. Only two energy values are given because the latter two states of ϕ_7 and ϕ_8 are degenerate. This is a consequence of greater wavefunction overlap between the DB potential wells, as the DBs are brought nearer or extra DBs are created, giving greater energy splitting [24]. This is what is occurring in the proximity effect. The proximity DB lowers the excited molecular state of the dimer, enabling it to be imaged at the same bias and current settings, and raises the anti-symmetric ground state, the constituent DBs appear brighter. In support for the latter statement, the difference in energy between the highest ground state splitting, ϕ_4, and the lowest excited state splitting, ϕ_5, for tetramer II is $-0.872-(-0.157)=-0.715$ eV and for tetramer I it is $-0.920-(-0.381)=-0.539$ eV. Therefore for tetramer I, which has smaller

dimensions, the ground states are closer to the excited states in energy.

Although in some cases, the proximity DB has an effect on a dimer even though the proximity DB is a large distance away from the dimer, in Figure 5.30 the two are separated by four dimer rows and in Figure 5.28 the defect and trimer are also separated by four dimer rows. This suggests the potential wells of the DBs have a longer range than previously imagined.

5.6 Conclusions

I have proved the earlier suggestion that controlling the Fermi level of the tip and the tip-sample separation via the sample bias and tunnel current parameters of the STM, respectively, gives the ability to controllably access and observe the excited molecular states of DB structures on H-terminated Si(001). Specifically, it is a high bias or a low current setting in the empty-states imaging mode, which leads to the appearance of excited molecular states. I was the first to investigate the effect of bias and current in a single situation of a DB dimer.

By numerically solving Poisson's equation for the tunnel junction set-up of the STM, I simulated the tip-induced band bending as a function of semiconductor depth. Using this data I produced calculated energy level diagrams which showed that at high biases, the Fermi level of the tip is raised above the excited molecular state of the DB dimer, and at low currents, the excited molecular state is brought below the tip Fermi level. This way electrons can tunnel into the excited state and it is observed in STM imaging.

I have presented the first investigation of 2D fabricated structures for DBs, including structures containing three and four DBs, i.e. trimers and tetramers. In agreement with DB dimers, the excited molecular states of the 2D structures were observed at high biases and low currents. Two DB tetramers were created that differed in terms of the rotation of their square shape with respect to the dimer row direction of the Si(001) surface. This surface reconstruction had an influence on the appearance of the two-dimensionally extended excited molecular states of the tetramers.

I modelled the structures by numerically solving the Schrödinger equation for a variety of 2D potentials chosen to reproduce our DB arrangements. By combining simulated individual quantum bound states, the STM images of the 2D structures have been well replicated. The modelling was successful once having applied a greater weighting to the higher energy bound states, in an approximation of the tunnelling matrix element, and taking into account how the ordering of the individual bound states is altered by the symmetry of the structure with respect to the surface reconstruction.

In addition to this, the excited molecular orbitals of DB dimers have been revealed with use of a proximity effect, the creation of an additional DB in the vicinity, without the need to change the bias and current. The proximity DB was having the effect of lowering the excited molecular state of the dimer, regardless of the charge of the proximity DB. This suggests the potential well of a DB is more long range than previously imagined, thus the greater overlap between wells gives a greater splitting of the states, lowering the excited molecular state.

Chapter 6

Results: Characterisation of the CDW of K-intercalated MoS_2

In this results chapter, scanning tunnelling microscopy of potassium intercalated MoS_2 is presented and discussed. The STM data has been acquired at liquid helium temperatures of 5 K. The dataset includes the discovery of a charge density wave, making the first observation of a CDW phase on MoS_2.

We begin with describing STM images of the Bragg or atomic lattice of the bare MoS_2 surface. Followed by a description of the different defects encountered on the surface. Succeeding this is an investigation of the interesting modulations observed on the surface, including a superlattice and what we perceive to be a charge density wave, and how the CDW modulations are associated with one type of defect.

6.1 Identifying the different lattices on the surface

6.1.1 The surface of MoS_2

Figure 6.1 (a) includes an STM image of a freshly cleaved $2H$-$K_{0.25}MoS_2$ sample. The left hand edge of the image appears brighter. This is most likely due to a tip effect, whereby the tip is dragging the top layer of the sample as it ends a line scan. This image is a forward scan and the corresponding backward scan has the bright edge on the right hand side. It was confirmed to be a tip effect because it remained the same after changing scanning parameters, including the tip scan speed and image size. This tip effect does not appear in the other STM images presented

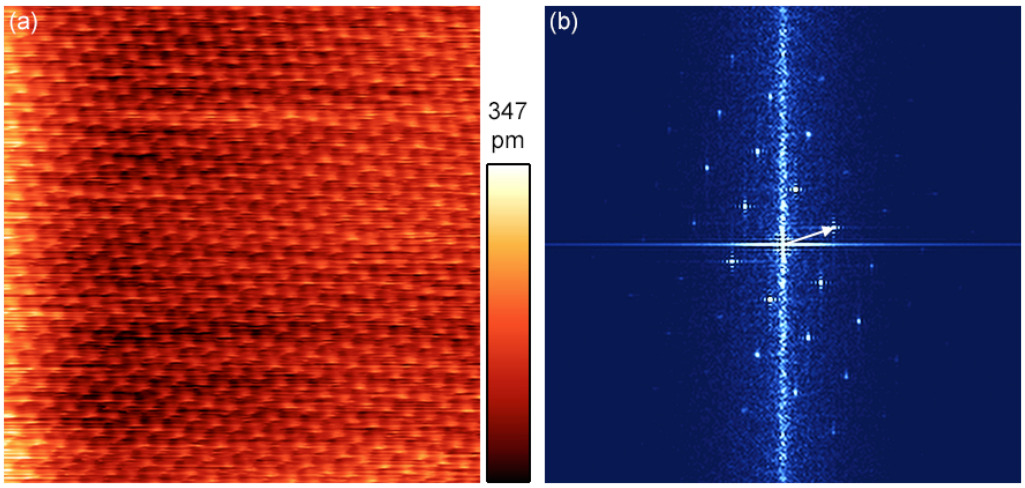

Figure 6.1: (a) STM image of the bare, exposed $2H$-$K_{0.25}MoS_2$ surface. Image settings are a sample bias of -50 mV, a tunnel current of 30 pA, 7 nm $\times$ 7 nm in size and a temperature of 5.5 K. (b) The Fourier transform (FT) of the STM image in (a). The white arrow marks one of the six spots for the surface lattice.

in this results chapter. Figure 6.1 (b) includes the Fourier transform of the image in (a). A Fourier analysis is required to accurately determine the periodicity of the surface lattice. The FT reveals the surface has a hexagonal lattice, the spots are arranged in an hexagon, with an average wavevector of 3.70 nm^{-1}. Thus, a lattice constant of 0.312 nm is determined from the wavevector using Equation 2.46, with an associated uncertainty of 0.020 nm, compared to the expected S lattice parameter of 0.320 nm [12]. Therefore it is the top, hexagonal S layer of the first exposed MoS_2 layer that is observed.

No adatoms were seen on the surface, suggesting no ammonia remains from the intercalation process and the intercalating K atoms, that sit above the exposed MoS_2 layer, most likely disperse and are lost in the vacuum, immediately after cleaving.

6.1.2 Defects on the surface

While coarse moving the tip across the MoS_2 surface, different defects were discovered and observed in scans of the surface. The defect at the bottom of the STM images in Figure 6.2, appearing as a completely dark patch in both bias polarities, is an intrinsic surface defect. The lack of atoms within the defect suggests it is a

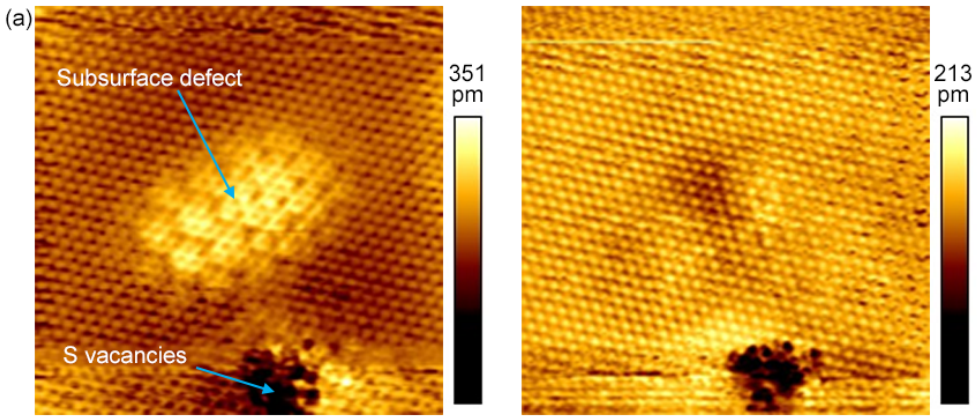

Figure 6.2: (a) A filled-state (-50 mV) and (b) an empty-state (50 mV) STM image of defects on the surface of $2H$-$K_{0.25}MoS_2$, taken at 5.5 K. The STM images are 10 nm $\times$ 10 nm in size and were taken at a current setpoint of 50 pA.

cluster of vacancies in the top S layer. Similar to the Se vacancy defects that have been found on the surface of other transition-metal dichalcogenides, $NbSe_2$ [31] and $TiSe_2$ [34], which are described in further detail in Section 3.4.2.

The other defect, at the centre of the STM images in Figure 6.2, appears as a bright, protruding region, of approximate radius 2.5 nm, with some modulations in the filled-states and a slight depression in the empty-states. This suggests the defect is negatively charged due to the additional upward band bending being induced, giving a region of a greater tunnel current in the filled states and a smaller current in the empty-states. Section 2.3.2 contains a more detailed explanation on defect-induced band bending. This defect is, however, not one associated with the imaged, top S layer, as it remains unbroken and undisturbed. Thus, it is believed to be a subsurface defect, the most probable cause a change in the level of K intercalation below. Therefore, the most feasible idea is that more K atoms are present below that particular surface region, meaning more electrons have been donated, giving the region a greater negative charge. Moreover, this doped sample is metallic, as it can be imaged at low biases, in the millivolts range, hence it seems likely more K atoms would be present.

In the bias-dependent imaging of Figure 6.3, which is the same surface area from Figure 6.2, charge density modulations can clearly be seen but of two different periodicities, one with more of a striped appearance while the other has a more

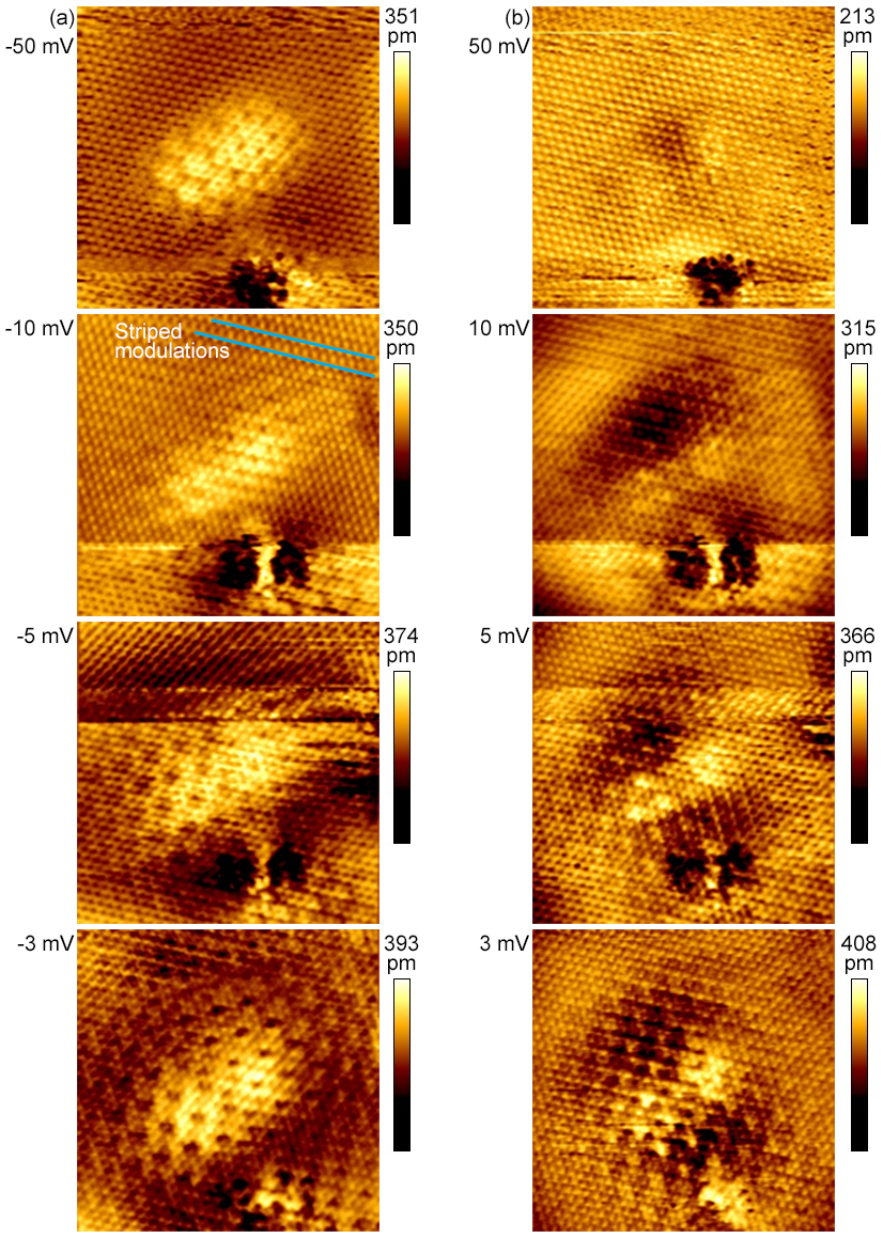

Figure 6.3: (a) Filled-state and (b) empty-state STM images of a defect region on the surface of $2H$-$K_{0.25}MoS_2$, taken at 5.5 K. For each image, the sample bias and z-range is indicated on the left and right, respectively. A charge density wave is observed localised to the defect area and its coverage increases as the bias magnitude is decreased, for the both the filled- and empty-states. All STM images are 10 nm $\times$ 10 nm in size and were taken using a tunnel current setpoint of 50 pA.

hexagonal appearance. The $\pm$10 mV images show the striped modulations already cover the whole surface in all directions, whereas the hexagonal modulations remain localised to the defect in the centre of the images. However, as the bias magnitude

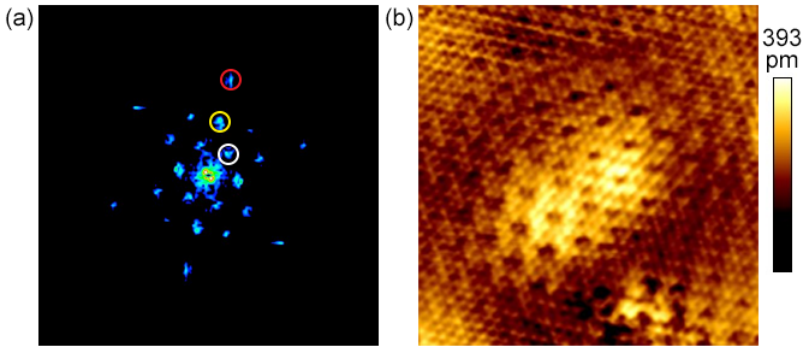

Figure 6.4: (a) Fourier transform of the STM image in (b). This is the same image from Figure 6.3 (a) and its settings are as follows: bias -3 mV, current 50 pA and size 10 nm $\times$ 10 nm. The FT reveals three different periodicities or lattices; the red circle encloses the Bragg spot for the top S layer, the yellow circle encloses the K superlattice spot and the white circle encloses the charge density wave spot.

is decreased, for both the filled- and empty-states, the coverage of the hexagonal modulations increases and in the -3 mV image they can be seen to cover the entire surface area imaged, including the regions away from the defect, and now overlaid with the striped modulations. The fact that at high bias magnitudes (-50 and ± 10 mV), the hexagonal modulations only appeared in patches suggests it is not a Moiré pattern, which would be expected to cover the whole surface.

To accurately determine the periodicities of the different charge density modulations on display, the STM images were Fourier transformed (FT) and one of these FTs is shown in Figure 6.4. The FTs revealed three different periodicities or lattices, corresponding to the Bragg lattice of the top S layer (see Figure 6.1), the K super-

	Wavevector (nm^{-1})	Lattice constant (nm)	Ratio	Lattice
Bragg (S atoms)	3.603 ± 0.033	0.320 ± 0.003	1	1×1
K superlattice	1.933 ± 0.074	0.597 ± 0.023	1.864	2×2
Charge density wave	1.106 ± 0.085	1.044 ± 0.080	3.258 $= 1.881\sqrt{3}$	$(2\sqrt{3} \times 2\sqrt{3})R30^\circ$

Table 6.1: Lattice constants, in real and reciprocal space, for the three different lattices revealed in the Fourier transforms. The associated uncertainties are one standard deviation of the values obtained from measuring all six spots for each lattice. The uncertainty for the Bragg, S lattice is so low because its unit cell has been corrected.

lattice of the intercalate layer and a newly discovered charge density wave (CDW). Evidence will be put forward and discussed later in this results chapter in support of the idea that this third lattice is a CDW. The wavevector of each of the three lattice FT spots was measured and these measurements are on display in Table 6.1, the conjugate, real space lattice constant was then calculated using Equation 2.46. In relation to the Bragg (S) lattice, it was determined the K superlattice has a 2×2 structure, matching the 2×2 peaks observed in x-ray diffraction patterns of the sample, and the CDW has a $2\sqrt{3} \times 2\sqrt{3}$ structure but rotated by 30° ($R30°$) with respect to the other two lattices. The ratios and lattice values in Table 6.1 do not quite match because of effects of thermal drift and piezoelectric scanner calibration offsets that remain even after correcting the S lattice, as detailed in Section 4.1. One comment is that if the CDW can co-exist with the other two lattices then it cannot be a surface reconstruction.

6.1.3 The superlattice modulation

In Figure 6.5, the STM image was taken for a region on the MoS_2 surface where the K superlattice can clearly be seen but the CDW cannot. The absence of the CDW was expected because there are no bright, protruding regions corresponding to a subsurface defect and the image was taken at a high sample bias of -100 mV. This image was included to give a direct view of how the superlattice appears in real space topographic imaging, without any interruptions from the CDW. The periodicity of the superlattice fits the level of K intercalation in this sample, because the distribution of K atoms between the MoS_2 layers has a 2×2 structure, see Figure 2.16. However, we are not observing the actual K atoms but rather the effect of their electron doping, which produces a modulation in the conduction band, imaged as a 2×2 superlattice in the top S layer. We will discuss this in more detail in Section 6.4, with experimental evidence from current imaging tunnelling spectroscopy measurements. The schematic diagram of the top S layer, in Figure 6.5 (b), presents the unit cell of the superlattice and in the FT, in Figure 6.5 (c) of the image in (a), the 2×2 superlattice spots are strikingly visible whereas the CDW spots are not.

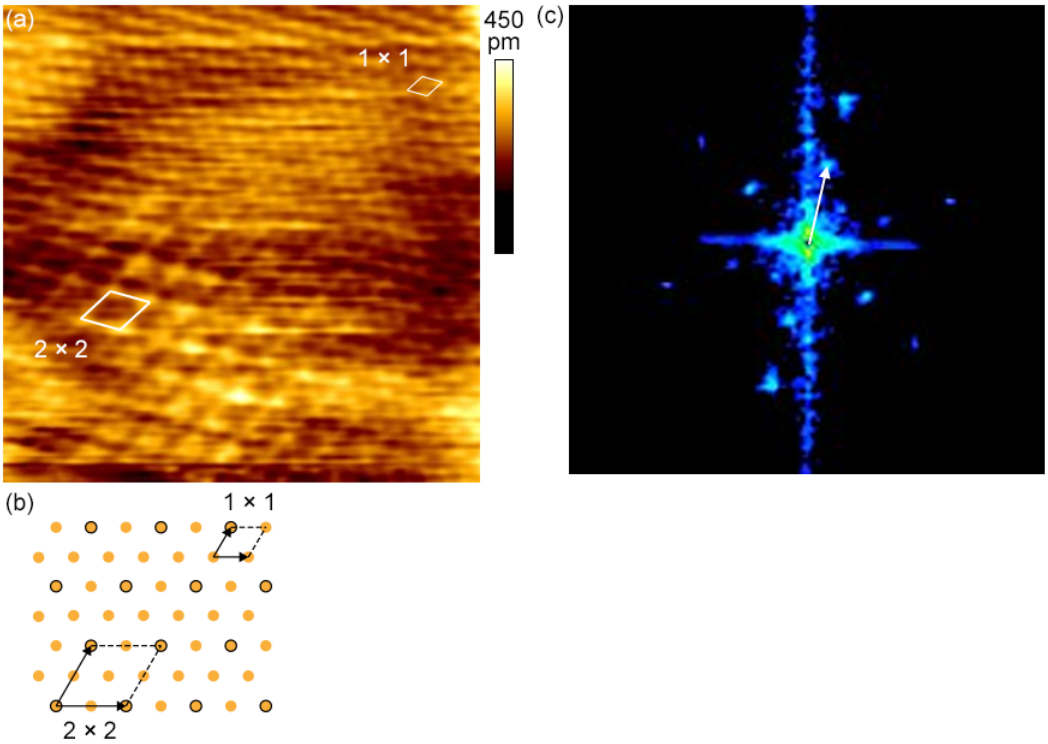

Figure 6.5: (a) STM image displaying the 2×2 superlattice on the $K_{0.25}MoS_2$ surface (image settings: -100 mV, 30 pA and 7.5 nm $\times$ 7.5 nm). (b) Schematic diagram displaying the unit cell of the superlattice on the top S layer which is imaged, unit cell is also highlighted in (a). (c) Fourier transform of (a), where the 2×2 spots have a particularly strong appearance. The white arrow marks one of the six spots for the superlattice.

6.1.4 The charge density wave modulation

In a somewhat similar fashion to Figure 6.5, the STM image in Figure 6.6 (a) exhibits the CDW localised to two bright, defect patches on the surface, without the superlattice, giving a definite indication to its appearance. Not seeing the superlattice in this -100 mV STM image is not unusual because it is not observed in the ± 50 mV images of Fig. 6.3 but it is observed in the -100 mV image of Fig. 6.5. The level of K intercalation is not constant throughout the sample. In the FT of this image, Figure 6.6 (c), the $(2\sqrt{3} \times 2\sqrt{3})R30^\circ$ CDW spots are visible and the superlattice spots are not, as expected from the image. The unit cell of the $(2\sqrt{3} \times 2\sqrt{3})R30^\circ$ CDW lattice is presented by the schematic in Figure 6.6 (b), and it fits the periodicity of the two CDW patches in the image, as conveyed. The CDW modulation is strongest, and most clearly visible, in the direction going from bottom

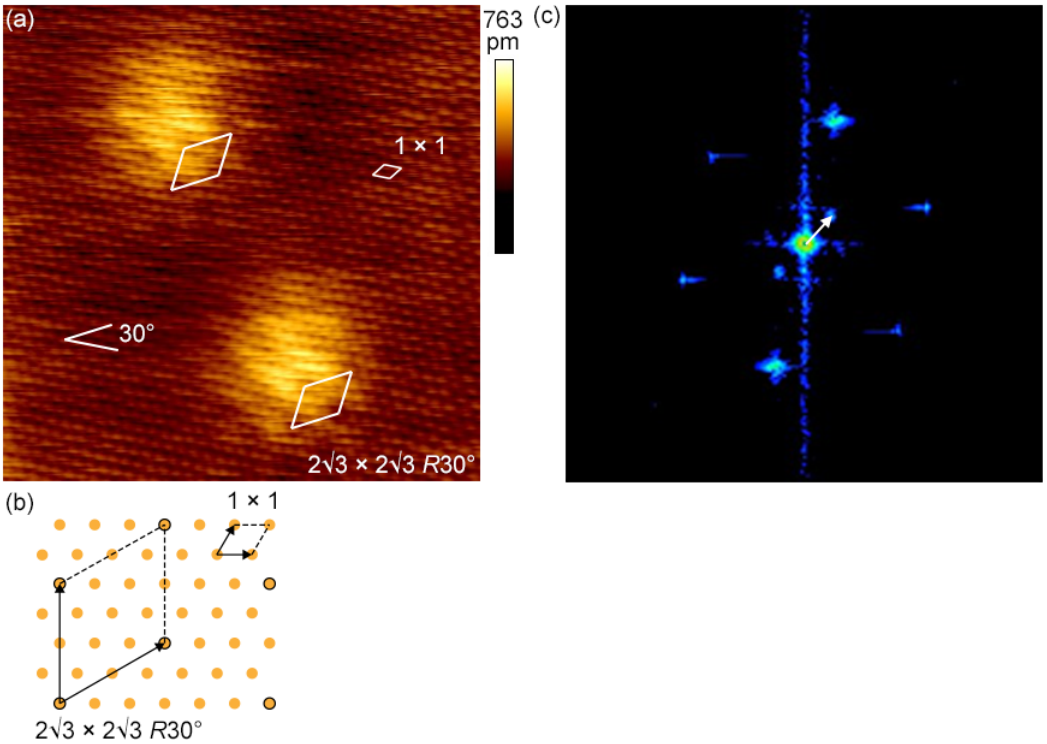

Figure 6.6: (a) STM image displaying the $(2\sqrt{3}\times 2\sqrt{3})R30°$ charge density wave localised to two defects on the $K_{0.25}MoS_2$ surface (image settings: -100 mV, 30 pA and 11.5 nm $\times$ 11.5 nm). (b) Schematic diagram displaying the unit cell of the CDW lattice on the top S layer which is imaged, unit cell is also highlighted in (a). (c) Fourier transform of (a), where the $(2\sqrt{3}\times 2\sqrt{3})R30°$ spots have a particularly strong appearance. The white arrow marks one of the six spots for the CDW.

left to top right of the image. This is also seen in the FT, where those corresponding spots appear brightest.

An important point to make is that while the coverage or lateral size of these two CDW regions increases for biases low in magnitude, as previously stated, they begin to overlap. However the modulations are not in phase or aligned with one another, see Figure 6.7, even though both the CDW patches have the same periodicity, making the CDW appear incommensurate like in some of the images in Figure 6.3. Though this seems reasonable after considering they do not have the same source.

The CDW of each individual source, or subsurface defect, would be able to cover the whole surface on their own, at biases of small magnitude. However, with two sources, and two separate CDW modulations, they can each cover the whole surface, but they may be out of phase when they overlap.

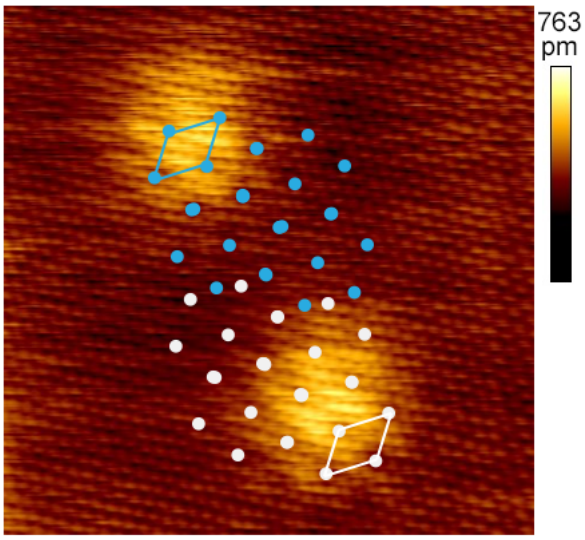

Figure 6.7: STM image displaying the charge density wave localised to two defects on the MoS_2 surface (image settings: -100 mV, 30 pA and 11.5 nm $\times$ 11.5 nm). This is the same image from Figure 6.6 (a). Overlaid on the image is the CDW lattice, and unit cell, for the two defects and they are shown to be out of phase when they overlap.

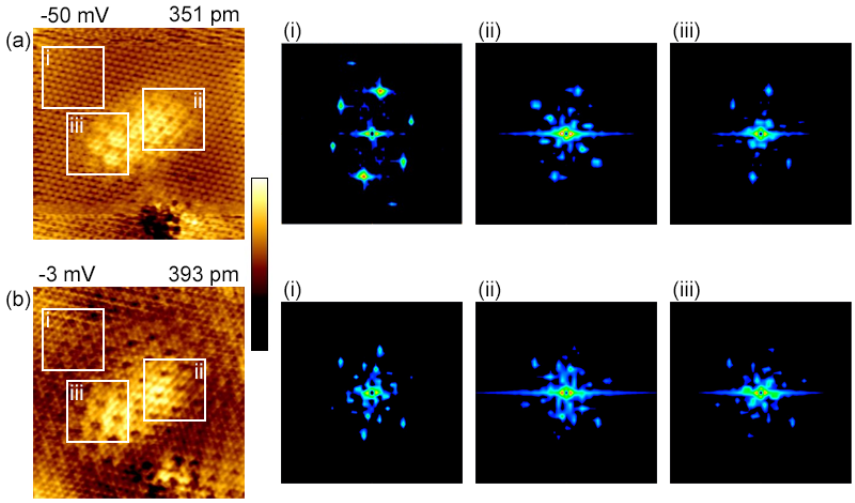

Figure 6.8: (a) A high magnitude bias and (b) a low magnitude bias STM image of the same defect region from Figure 6.3. The sample bias and z-range is indicated on the left and right, respectively, the tunnel current is 50 pA and the images are 10 nm $\times$ 10 nm in size. For each image, a Fourier transform was taken of a 3 nm $\times$ 3 nm area for a region of (i) 1×1 S atoms, (ii) 2×2 superlattice and (iii) $(2\sqrt{3} \times 2\sqrt{3})R30^\circ$ CDW. As the bias magnitude is decreased, the CDW coverage increases and as a result the partial FTs for (b) contain the spots for all three lattices.

Partial areas of the STM image in Figure 6.8 (a) were Fourier transformed separately, in order to relate the particular charge density modulations in the image

to the spots it produces in the FT. Panel (i) of the STM image in Figure 6.8 (a) just includes the S atoms of the bare surface, this produces the 1×1 spots in the FT of the image, like in Figure 6.1. Panel (ii) contains the striped modulations overlaid on the surface and this produces the 2×2 and 1×1 spots in the corresponding FT, as in Figure 6.5. Panel (iii) contains the hexagonal modulations overlaid on the surface and this produces the $(2\sqrt{3} \times 2\sqrt{3})R30^\circ$ and 1×1 spots in the FT, as in Figure 6.6.

To highlight how the CDW coverage increases as the bias magnitude decreases, this partial FT technique was repeated for a low magnitude bias image of the same area, Figure 6.8 (b). The partial FTs were taken of the same regions as in (a) and now each of the three partial FTs contain all three lattice spots, which is expected because the modulations cover the whole image.

Hence, three lattices have been identified on the surface of $K_{0.25}MoS_2$: a Bragg lattice for the top S layer, a superlattice due to the intercalation, and a charge density wave. The CDW appeared, in STM imaging, localised to a subsurface defect, which we believe to be caused by a greater number of intercalating K atoms in the van der Waals gap between MoS_2 layers. The coverage of the CDW increased as the magnitude of the sample bias was decreased. In the next section, we discuss proof to confirm it is indeed a CDW that has been discovered.

6.2 Proof & discussion of a charge density wave

Three pieces of evidence are presented to prove that the $(2\sqrt{3} \times 2\sqrt{3})R30^\circ$ lattice on the surface of K-intercalated MoS_2 is a CDW. These are the wavevector of the CDW does not vary with sample bias, a gap in the density of states at the Fermi level, and the modulations of the CDW are out of phase when contrasting filled- and empty-states imaging, and they will be elaborated below.

Figure 6.9 features line profiles taken across the Fourier transform of an STM image of the CDW, thus the profiles are a plot of Fourier intensity as a function of reciprocal distance. These Fourier intensity profiles were taken along two directions, one across the superlattice and Bragg spots (Fig. 6.9 (c)) and the other across the CDW spot (Fig. 6.9 (d)). The two directions are separated by an angle of 30°.

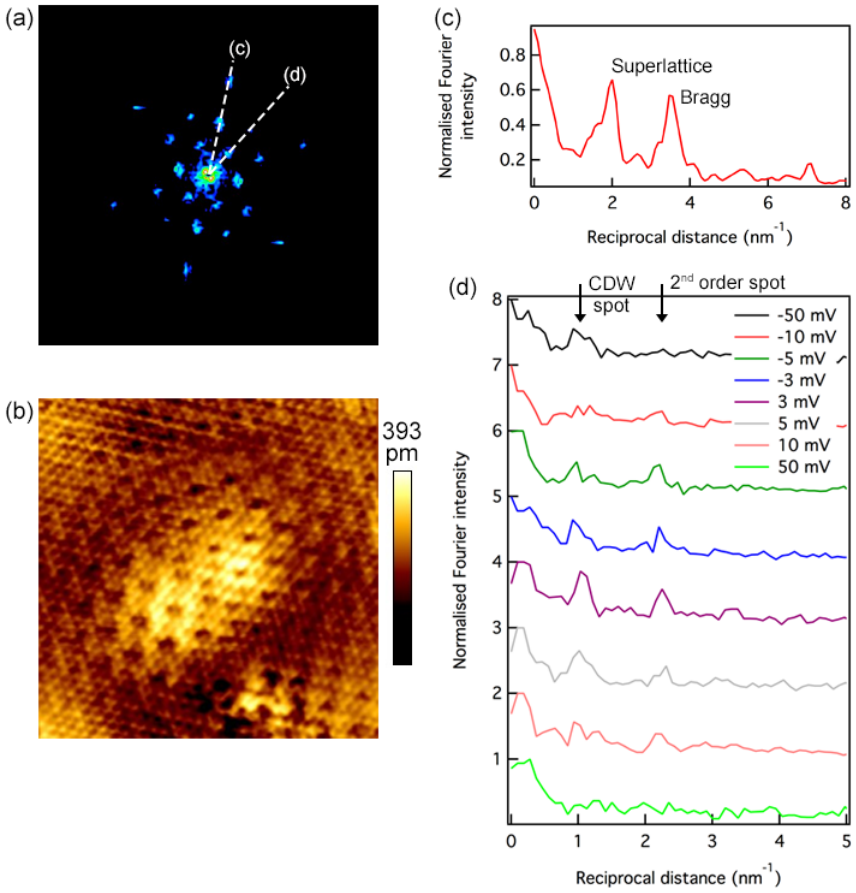

Figure 6.9: Line profiles taken along two directions, indicated by dashes white lines, on the Fourier transform (a) of an STM image (b) of the CDW on MoS_2. The settings for the STM image are: bias -3 mV, current 50 pA and size 10 nm $\times$ 10 nm. This FT and image set is identical to the one displayed in Figure 6.4. (c) The second order spot of the superlattice coincides with the Bragg (S) spot, proving that the two lattices are commensurate. This particular profile was given a Binomial smoothing. (d) The wavevector of the charge density wave does not change with sample bias, proving that it is dispersionless. The Fourier intensity was normalised by dividing through by the maximum of the peak at the centre of the FT.

For panel (d), the Fourier intensity profiles were taken across the same line for the FTs of STM images captured over a range of sample biases. Panel (d) shows the CDW spot in the Fourier transform to remain fixed as a function of energy or sample bias and, hence, the CDW lattice wavevector has no energy dependence. This dispersionless feature is a known characteristic of a CDW. Furthermore, it simultaneously rules out quasi-particle interference effects, such as Friedel oscillations, and bound states of a quantum well, two phenomena that exhibit dispersion, as pos-

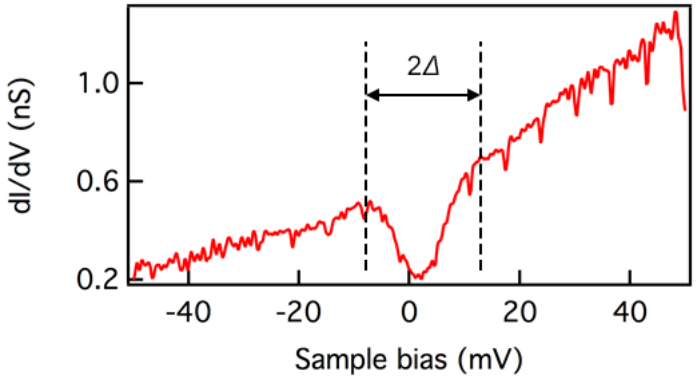

Figure 6.10: Scanning tunnelling spectroscopy taken on $K_{0.25}MoS_2$ shows the opening of a CDW gap around the Fermi level. The gap (2Δ) was measured between the dashed lines, which mark the centre position of the coherence peaks, and was found to be (23 ± 1) mV. The centre of the coherence peaks was determined by fitting a Gaussian curve to the peak. This numerically differentiated conductance plot is an average of 360 point spectra, regulated at -100 mV and 30 pA, and a binomial smoothing of factor 3 was applied. The associated uncertainty is the sum of the standard deviation related to fitting the two Gaussian curves.

sible explanations. The plots in panel (d) display a peak for the CDW spot, as has been explained, and a second peak of lower intensity at a reciprocal distance which is double the CDW wavevector. Successive peaks of lesser intensity are expected for a FT spot, at multiples of the spot's wavevector. In panel (c) of Figure 6.9, the second order peak for the K superlattice coincides with the first S Bragg spot, demonstrating the commensurate nature of the superlattice. From Table 6.1, the ratio of the superlattice, with respect to the Bragg lattice, was calculated to be 1.864, compared to the expected value of 2, but almost identical to 1.881, which is the coefficient of $\sqrt{3}$ in the ratio for the CDW lattice. For this reason the CDW must also be commensurate with the Bragg lattice.

The opening of a small gap is measured at the Fermi level in scanning tunnelling spectroscopy results of MoS_2, shown in Figure 6.10, and the value of the gap was found to be (23 ± 1) mV. The gap was determined by fitting a Gaussian curve to the peaks either side of the gap and measuring the energy difference between the centre of the two Gaussian curves. The uncertainty with the gap measurement was taken to be the sum of the standard deviations associated with the fitting of the two Gaussian curves. In addition, the different conductance does not

fall to zero in the gap, and thus the non-zero conductance at zero bias verifies the metallic character of the sample, as predicted from its high level of intercalation. Whereas, point spectroscopy results taken at liquid nitrogen temperatures of 78 K, an example is shown in Figure 6.11 (a), do not display a gap because the greater thermal broadening masks the gap.

The energy gaps of superconductors have similarly been detected in scanning tunnelling spectroscopy measurements [70]. A superconducting gap 2Δ at absolute zero is roughly related to the critical temperature T_c, the temperature where the transition from normal conducting to superconducting phase occurs, via the following approximation,

$$2\Delta \approx 3.5 k_B T_c, \tag{6.1}$$

where k_B is Boltzmann constant ($1.38 \times 10^{-23}\mathrm{JK}^{-1}$) [70]. Using Equation 6.1 for our K-intercalated MoS_2 sample, which has a critical temperature of 6.9 K [83, 4], the superconducting gap is estimated to be 2.1 meV. At experimental temperatures of 5.7 K, the thermal broadening ($k_B T$) is 0.5 meV, roughly a quarter of this gap value, and this temperature may be too close to the critical temperature, as Equation 6.1 is valid at absolute zero, making it unlikely for us to observe the superconducting gap in STS measurements. Furthermore, this rules out superconductivity as the cause for the much larger energy gap of 23 meV detected in STS. Applying this theory to our scenario of a CDW gap, an estimation of 77 K was calculated for the transition temperature for entering the CDW phase. Using this Bardeen-Cooper-Schrieffer (BCS) factor of 3.5 assumes a weaker electron-phonon coupling, compared to other TMD-CDW systems. This prediction seems reasonable, since it is very close to the temperature where the CDW was imaged in liquid nitrogen conditions, suggesting the CDW transition temperature lies just above liquid nitrogen temperatures. Equation 6.1 is valid for a gap measured at 0 K but our measurement is obtained at a temperature of 5.7 K which is much less than the estimate transition temperature or the temperature of liquid nitrogen, their ratio (T/T_c) is almost zero, making the approximation still relevant to our case.

Wide bias range spectroscopy data collected, shown in parts (b) and (c) of Fig-

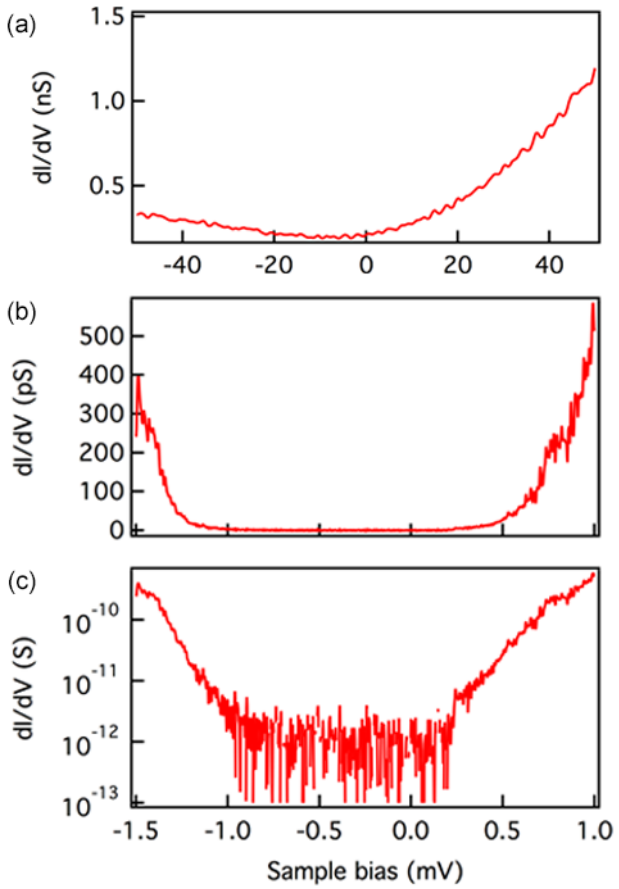

Figure 6.11: (a) Scanning tunnelling spectroscopy taken on $K_{0.25}MoS_2$ at a temperature of 78.3 K. (b) Representative wide bias range spectroscopy taken at 5.6 K. Both are numerically differentiated conductance plots and have been binomially smoothed using a smoothing factor of 3. (a) is an average of 60 point spectra, regulation settings were −100 mV and 30 pA, and (b) is an average of 100 point spectra, regulation settings were −1.5 V and 50 pA. (c) is a log plot of (b), making it easier to identify the band gap.

ure 6.11, share some similarities and resemblance with spectroscopy of single layer MoS_2 islands on Au(111) taken by A. Bruix *et al.* [90]. It exhibits a semiconducting band gap of 1.26 eV, measured from the log plot in Figure 6.11 (c), very close to the 1.23 eV band gap for bulk MoS_2 [73]. However, in comparison to Figure 6.10, the wide bias range spectroscopy does not display a CDW gap. The reason for this is the much greater sample bias of the regulation settings means the tip is further away from the surface and smaller currents are being measured, and, additionally, the number of data points has to cover a wider bias range giving a lower energy resolution.

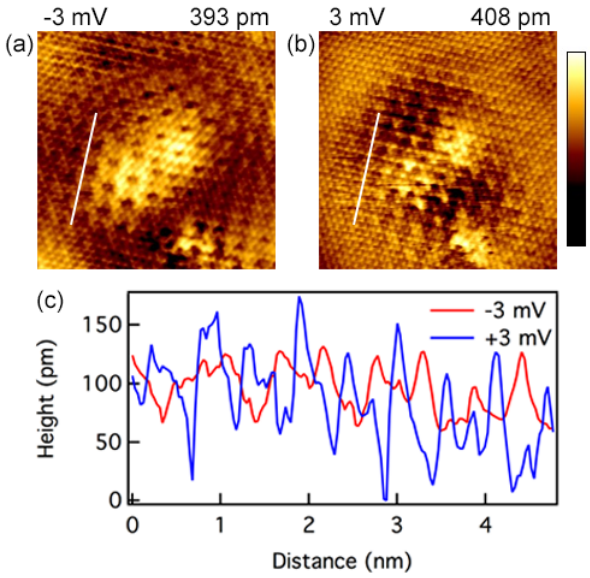

Figure 6.12: Height profiles taken along the same region, across the white lines, in (a) a filled-state and (b) an empty-state STM image are shown in (c). They prove that the charge density modulations are out of phase when the bias polarity is switched. The sample bias and z-range is indicated on the top-left and -right, respectively, of each image. Both STM images are 10 nm $\times$ 10 nm in size and a current setpoint of 50 pA was used. This is the same area of MoS_2 as from Figure 6.3.

In Figure 6.12, a topographic line profile is taken across the same section of a dual bias image set, (a) and (b), of a CDW region on K-intercalated MoS_2. The modulations of the $(2\sqrt{3} \times 2\sqrt{3})R30^\circ$ CDW lattice were established to be out of phase when comparing the line profiles of the filled- and empty-states imaging. In panel (c) of Figure 6.12, a peak in the filled-states line profile (red curve) coincides with a trough in the empty-states (blue curve), and vice versa. This specific part of the STM images was used to compare the phase because here the $(2\sqrt{3} \times 2\sqrt{3})R30^\circ$ lattice is more prominent and clear with a flat topography, whereas in the other regions it is obscured by presence of the 2×2 superlattice.

6.3 Temperature-dependent imaging

All the data presented in this results chapter has been obtained at liquid helium temperatures of 5.5 K, furthermore Figure 6.13 includes STM data acquired at two additional temperatures. The CDW on K-intercalated MoS_2 has been imaged at 10.0 K (Figure 6.13 (b)), by counter heating from 5.5 K, and at 78.4K (Figure 6.13 (c)),

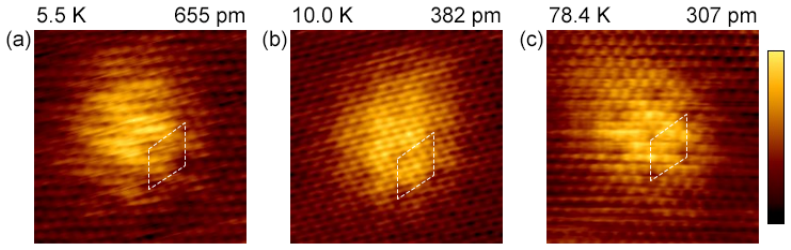

Figure 6.13: Charge density waves observed in STM imaging at different temperatures, ranging from liquid helium to liquid nitrogen conditions. (a) 5.5 K (other settings: -100 mV and 30 pA), (b) 10.0 K (-100 mV and 30 pA) and (c) 78.4 K (-400 mV and 50 pA). All images are 5.5 nm $\times$ 5.5 nm and the z-range is displayed on the right. Images (a) and (b) are of the same area, which is the bottom defect in Figure 6.6 (a). The unit cell for the CDW lattice is shown in each image.

liquid nitrogen temperatures. The value of 10.0 K was chosen because at 5.5 K the sample is mostly likely in its superconducting state. The reason for the uncertainty is that it is a broad transition to superconductivity for this intercalated sample, onset around 7 K [83, 4], so at 10.0 K we can be certain the sample is not superconducting. For further information visit Section 2.4. This suggests that the temperature, at which the transition from normal to CDW phase occurs, lies above 78.4 K.

Accompanying transport measurements are required for this sample, such as a temperature dependent measurement of the in-plane resistance, to accurately determine the transition temperature. These resistivity measurements have been planned in conjunction with our collaborators, C. Howard *et al.*, who prepared the samples. Once this temperature value is known then the STM, and its counter heating capabilities, can be used to image a CDW on the surface below this temperature and show the CDW disappear above the temperature, i.e. mapping the transition with topographic images as function of temperature. Searching for the transition temperature with STM is difficult because counter heating is an expensive process, in terms of the larger amounts of liquid helium being used, which would result in having to stop experiments and refill the cryostats more often, and time spent waiting for thermal drift to disappear at each new temperature setting.

6.4 Current imaging tunnelling spectroscopy measurements

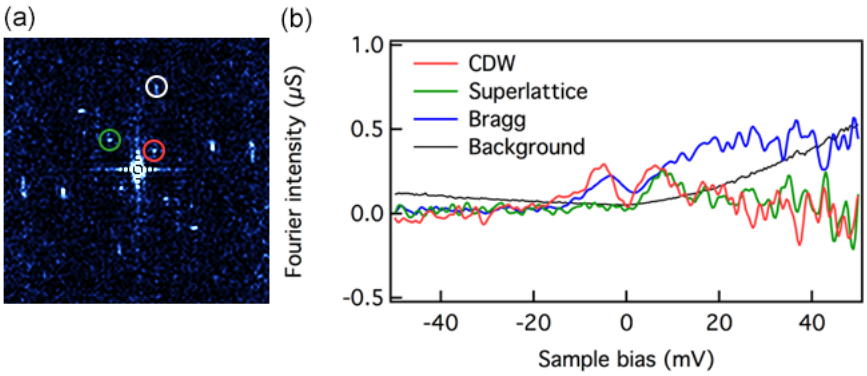

Figure 6.14: (a) Fourier transform of a numerically differentiated conductance map at 7.41 mV. This conductance map is a slice from a current imaging tunnelling spectroscopy (CITS) measurement from -100 mV to 100 mV, regulated at -100 mV and 50 pA, of a 8 nm $\times$ 8 nm area over the same region of MoS_2 from Figure 6.3. (b) Fourier intensity as a function of energy for the CDW, K superlattice and S Bragg spots in (a). The spots are enclosed by circles whose colour matches that of the corresponding trace, apart from Bragg spot which is marked by a white circle for better contrast. The superlattice plot is an average of two and the Bragg plot is an average of six. The Fourier intensity was normalised by subtracting the background intensity, which is also plotted. A binomial smoothing (factor 3) was applied to the three datasets.

Figure 6.14 contains analysis of a current imaging tunnelling spectroscopy (CITS) measurement of the MoS_2 surface, where all three lattices are observed. The raw dataset is a current map as a function of spatial position and sample bias or energy. Firstly, it was topography corrected using a decay constant of 3.5×10^9 m^{-1} for the vacuum gap, computed from a measurement of tunnel current as a function of tip-sample separation [91]. Numerically differentiating this give a differential conductance map as a function of position and energy, analogous to spatial mapping of energy-dependent density of states. Fourier transforming this gives a Fourier intensity map for each energy, and by sweeping through the measured energy range it shows the $(2\sqrt{3} \times 2\sqrt{3})R30^\circ$ CDW spots have no dispersion and the 2×2 superlattice spots do not appear at all biases. These results are easier to display by plotting the Fourier intensity as a function of bias or energy for each of the three different spots — see Figure 6.14 (b). The plot for the CDW spot clearly shows a

gap around zero bias or the Fermi energy, similar to the gap feature observed in Figure 6.10, this directly links the gap to the CDW lattice. The corresponding plot for the superlattice spot shows a peak and rise for low positive biases, a consequence of the intercalating layers of K atoms donating electrons to the low energy unoccupied states. The said plot for Bragg spot shows signs of a gap at zero energy, indicating the CDW is present in the top S layer.

This method gives the FT spots for the periodicities at each individual electronic state, the energy resolution of which depends on the spectroscopy settings of the measurement, whereas the FT of an STM image gives the spots for the periodicities of all energies upto the image bias.

In Figure 6.14 (a), only two spots are seen for the CDW lattice instead of the expected six, because as in Figure 6.6 of Section 6.1.4, the modulations of the CDW are more visible from the bottom left to the top right of the STM image (see Fig. 6.15 (c)).

The superlattice spots are shown to only appear at low empty-state biases, prompting the question why is it still observed on the surface when imaging in the filled-states, for example it is present in the STM image of Figure 6.5. The reason for this is, as well as making an electron contribution, the intercalating layer of K below the top, surface MoS_2 layer additionally gives a physical contribution which is what is imaged. The periodicity of the 2×2 lattice imaged matches the distribution of K atoms at this level of intercalation, as shown in Figure 2.16 and described earlier.

Figure 6.15 features two numerically differential conductance maps taken at biases corresponding to the two peaks either side of the CDW gap in the plot of Fourier intensity against bias in Fig. 6.14 (b). The two maps serve as spatial maps of the density of states at the peak energies, and they display the phase difference across the gap at zero bias. The modulations are out of phase between the filled-states map at -5 mV (Fig. 6.15 (a)) and the empty-states map at 5 mV (Fig. 6.15 (b)). The maps show the CDW modulation to be predominately running from the bottom left to the top right corner in agreement with the topographic image

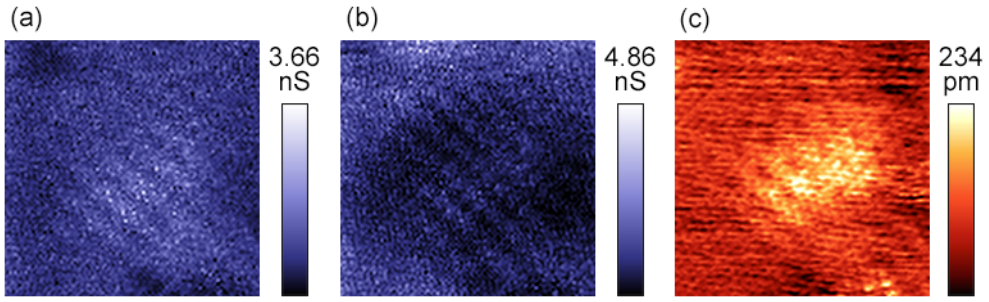

Figure 6.15: Differential conductance maps at (a) -5 mV and (b) 5 mV, from the CITS measurement featured in Figure 6.14. The two biases correspond to the peaks either side of the gap at zero bias for the CDW plot of Fourier intensity against bias in Fig. 6.14 (b). The CITS measurement was smoothed (factor 3) along the z (conductance) axis, before extracting the two maps. (c) A topographic image of the same 8 nm $\times$ 8 nm region, taken at -100 mV and 50 pA.

in Fig. 6.15 (c) and the Fourier transform in Fig. 6.14 (a).

6.5 Conclusions

I have presented the first STM investigation of K-intercalated 2H-MoS_2, which includes the discovery of a CDW phase. This discovery marks the first ever experimental observation of a CDW state on MoS_2.

STM imaging of K-intercalated MoS_2 at 5 K, along with its corresponding Fourier transforms, has revealed three different lattices on the surface: a 1×1 S lattice, of the top imaged S layer; a 2×2 K superlattice, due to the intercalating layers of K; and a commensurate $(2\sqrt{3} \times 2\sqrt{3})R30^\circ$ CDW.

Initially, the CDW was only observed localised to subsurface defects, most likely caused by greater levels of K intercalation, but the coverage increased for lower sample bias magnitudes. The CDW state was observed at liquid helium and liquid nitrogen conditions, clearly suggesting the transition to the CDW phase lies at higher temperatures.

Three pieces of evidence were presented to prove this is a CDW, and simultaneously rule out other explanations such as Friedel oscillations and Moiré patterns. Firstly, the periodicity does not change with bias or energy; it is dispersionless. Secondly, spectroscopy measurements display a small energy gap of about 23 mV, around the Fermi level, in the differential conductance or density of states. And

thirdly, the modulations are out of phase when the bias polarity is reversed, i.e. when switching between empty- and filled-states.

Data processing of a CITS measurement gave a plot of Fourier intensity as a function of energy for each of the three different lattices. For the CDW, a gap was displayed around zero bias, directly associating the gap to the CDW lattice. For the superlattice, there was a peak at the low empty-state biases, a result of electron donor nature of the intercalating layers of K. As for the S lattice, there was what resembles a small gap, indicating the CDW is present in the top S layer.

Chapter 7

Conclusions

In this thesis, I have presented studies of confined and correlated electron states on semiconductor surfaces. I have investigated the electronic states confined to structures of dangling bond point defects on the hydrogen-terminated silicon (001) surface, as well as the many-body, correlated electronic phases of potassium-intercalated molybdenum disulfide.

7.1 Dangling bonds on H-terminated Si(001)

Dangling bond (DB) arrangements, containing two to four DBs and for the first time spanning two-dimensions, were purposefully created on H-terminated Si(001). The excited molecular states of these DB structures were observed in empty-states STM imaging at high sample bias and low tunnel current settings. I was the first to investigate the effect of bias and current in a single situation of a pair of DBs. Simulating the tip-induced band bending and calculating it as a function of semiconductor depth, gave the opportunity to create numerical energy level diagrams. They showed at high biases and low currents, electrons could resonantly tunnel from the tip to the excited state of the structure.

The appearance of a DB structure's excited state was shown to be influenced by the surface reconstruction of Si(001) and additional DBs created in close proximity, since both alter the potential landscape around the structure. Using appropriate 2D potential wells to model the DB structure, for which the Schrödinger equation was numerically solved, individual bound states were simulated. Considering how the

ordering of individual states depends upon the potential of the background surface and combining the individual states using an approximation of the tunnelling matrix element, allowed us to replicate the states observed in STM imaging. The additional DB in the proximity effect introduces an additional potential well, meaning greater wavefunction overlap and energy splitting, thus lowering the excited state in energy.

7.1.1 Future work

The next stage of this research project would involve collecting scanning tunnelling spectroscopy measurements of a DB dimer, before and after the creation of a proximity DB. The spectroscopy, and thus the density of states, would display the quantum bound states of the dimer including the excited molecular state and the proposed lowering of the excited molecular state in energy due to the proximity effect. Point spectroscopy, measuring tunnel current as a function of sample bias, would be obtained for the central protrusion of a dimer's excited molecular state and the dimer's two constituent DBs. However, the central protrusion is extremely bright and tall, and broader, compared to the two constituent DBs, and the height difference would perturb the comparison of the two measurements. To counter this, the tip height should be varied when taking the point spectra, in other words, the tip is stepped in a certain vertical distance, closer to the sample, before taking the measurement of the DB. The height of the vertical step can be determined from a topographic line profile, by measuring the height difference between the DB and the central protruding lobe of the excited molecular state.

7.2 Charge density wave of K-intercalated MoS_2

I have presented the discovery, and the first experimental evidence, of a charge density wave (CDW) state of K-intercalated 2H-MoS_2. A complementary STM and STS investigation, along with the Fourier transforms, was used to characterise the CDW state. It was revealed to have a commensurate $(2\sqrt{3} \times 2\sqrt{3})R30^\circ$ lattice and an energy gap of about 23 mV at the Fermi level. Measurements also revealed a 1×1 lattice, of the top S layer that was imaged and hosted the CDW, and a 2×2 lattice, due to the electron doping nature of the intercalating layers of K.

The CDW was observed localised to subsurface defects, most likely caused by greater levels of K intercalation, but the coverage increased as the sample bias magnitude was decreased. The CDW state was observed at liquid helium and liquid nitrogen conditions, suggesting the transition to the CDW phase lies at a higher temperature.

7.2.1 Future work

The next step for this research project would be to make accompanying electron transport measurements for this K-intercalated MoS_2 sample. Such as a temperature dependent measurement of the in-plane resistance, measuring the resistance from room temperature down to liquid helium temperatures, to accurately determine the transition temperature to the CDW phase. Sudden drops in resistance will signal transitions to different correlated electron phases. Once this temperature value is known then the STM, and its counter heating capabilities, can be efficiently used to image a CDW on the surface below this temperature and show the CDW disappear above the temperature, i.e. mapping the transition with topographic images as function of temperature. Once this transition temperature is known, the CDW state will be fully characterised. Following this, STM and STS studies of other intercalations, including alkali and alkaline earth metals, of MoS_2 may commence, in the search for CDWs and other exotic, correlated electron states.

Appendix A

Charge density of a doped semiconductor

E_F	Fermi level
E_C	Conduction band minimum
E_V	Valence band maximum
E_D	Donor impurity level
E_A	Acceptor impurity level
E_{Fi}	Intrinsic Fermi level

Table A.1: Key of the symbols used to describe the electron energy levels of a doped semiconductor. All energies are measured with respect to the intrinsic Fermi level, which is taken to be the zero of the energy scale.

Consider a spherical shell in reciprocal space, of radius k and thickness dk. The product of the volume of the shell and the density of allowed k values gives the density of states.

$$\begin{aligned} g(k)\,dk &= 4\pi k^2\,dk \times \left(\frac{2\pi}{L}\right)^{-3} \\ &= \frac{Vk^2}{2\pi^2}\,dk. \end{aligned}$$

L being the distance between allowed states in real space ($V = L^3$). To convert this into a function of energy, the spin degeneracy of electronic states, $g(E)\,dE = 2g(k)\,dk$, and the dispersion relationship, $E = \frac{\hbar^2 k^2}{2m}$, have to be considered. Thus

using

$$k = \left(\frac{2m}{\hbar^2}E\right)^{\frac{1}{2}} \text{ and } \frac{dE}{dk} = \frac{\hbar^2}{m}k,$$

gives

$$g(E) = 2g(k)\frac{dk}{dE} = 2\frac{V}{2\pi^2} \times k \times k\frac{dk}{dE} = \frac{V}{\pi^2} \times \left(\frac{2m}{\hbar^2}E\right)^{\frac{1}{2}} \times \frac{m}{\hbar^2} \quad \text{(A.1)}$$

$$= \frac{V\sqrt{2}}{\pi^2\hbar^3}m^{\frac{3}{2}}E^{\frac{1}{2}}. \quad \text{(A.2)}$$

The density of electrons n, or the number of electrons per unit volume V in the conduction band, is given by

$$n(E_F,T) = \frac{1}{V}\int_{E_C}^{\infty} f(E,E_F,T)g_C(E)\,dE. \quad \text{(A.3)}$$

Where $f(E,E_F,T)$ is the Fermi-Dirac distribution for the electrons,

$$f(E,E_F,T) = \frac{1}{1+\exp(\frac{E-E_F}{k_BT})},$$

which gives the probability of an electron state of energy E at a temperature T being occupied, and $g_C(E)$ is density of states in the conduction band,

$$g_C(E) = \frac{V\sqrt{2}}{\pi^2\hbar^3}(m_e^*)^{\frac{3}{2}}(E-E_C)^{\frac{1}{2}},$$

adapted from Equation A.2 by replacing the free electron mass m with the conduction band effective mass m_e^*.

Similarly, the density of holes p is given by

$$p(E_F,T) = \frac{1}{V}\int_{-\infty}^{E_V} f_h(E,E_F,T)g_V(E)\,dE. \quad \text{(A.4)}$$

Where $f_h(E,E_F,T)$ is the Fermi-Dirac distribution function for holes,

$$f_h(E,E_F,T) = 1 - f(E,E_F,T) = \frac{1}{1+\exp(\frac{E_F-E}{k_BT})},$$

and $g_V(E)$ is the density of valence band states,

$$g_V(E) = \frac{V\sqrt{2}}{\pi^2\hbar^3}(m_h^*)^{\frac{3}{2}}(E_V - E)^{\frac{1}{2}},$$

with m_h^* being the valence band effective mass.

The density of ionised donors N_D^+, or the probability of whether a donor state is occupied or not, is given by

$$N_D^+(E_F) = N_D\left(\frac{1}{1+2\exp\left(\frac{E_D-E_F}{k_BT}\right)}\right), \tag{A.5}$$

where N_D is the concentration of donor atoms and the factor of two in front of the exponential term is due to spin degeneracy. This is assuming no interaction between dopant states.

Similarly the density of ionised acceptors N_A^- is given by

$$N_A^-(E_F) = N_A\left(\frac{1}{1+4\exp\left(\frac{E_F-E_A}{k_BT}\right)}\right), \tag{A.6}$$

where N_A is the concentration of acceptor atoms and the additional factor of two in front of the exponential term represents the light and heavy hole bands.

Finally Equations A.3, A.4, A.5 and A.6 can be substituted into the equation below to give an expression for the charge density ρ of a doped semiconductor.

$$\rho = e(p - n + N_D^+ - N_A^-)$$

Bibliography

[1] J. W. Lyding, T. C. Shen, J. S. Hubacek, J. R. Tucker, and G. C. Abeln. Nanoscale patterning and oxidation of H-passivated Si(100)-2x1 surfaces with an ultrahigh vacuum scanning tunneling microscope. *Appl. Phys. Lett.*, 64(15):2010, 1994.

[2] S. R. Schofield, P. Studer, C. F. Hirjibehedin, N. J. Curson, G. Aeppli, and D. R. Bowler. Quantum engineering at the silicon surface using dangling bonds. *Nat. Commun.*, 4:1649, apr 2013.

[3] R. B. Somoano, V. Hadek, A. Rembaum, S. Samson, and J. A. Woollam. The alkaline earth intercalates of molybdenum disulfide. *J. Chem. Phys.*, 1068(1975):1068–1073, 1975.

[4] John A. Woollam and Robert B. Somoano. Physics and chemistry of MoS2 intercalation compounds. *Mater. Sci. Eng.*, 31(Ii):289–295, dec 1977.

[5] M. Mitchell Waldrop. More Than Moore. *Nature*, 530:145, 2016.

[6] F. Withers, O. Del Pozo-Zamudio, A. Mishchenko, A. P. Rooney, A. Gholinia, K. Watanabe, T. Taniguchi, S. J. Haigh, A. K. Geim, A. I. Tartakovskii, and K. S. Novoselov. Light-emitting diodes by band-structure engineering in van der Waals heterostructures. *Nat. Mater.*, 14(February):301–306, 2015.

[7] Norikuni Yabumoto, Kazuyuki Saito, Mizuho Morita, and Tadahiro Ohmi. Oxidation Process of Hydrogen Terminated Silicon Surface Studied by Thermal Desorption Spectroscopy. *Jpn. J. Appl. Phys.*, 30(Part 2, No. 3B):L419–L422, 1991.

[8] Lequn Liu, Jixin Yu, and J. W. Lyding. Atom-resolved three-dimensional mapping of boron dopants in Si(100) by scanning tunneling microscopy. *Appl. Phys. Lett.*, 78(3):386–388, 2001.

[9] A. M. Yakunin, A. Yu Silov, P. M. Koenraad, J. H. Wolter, W. Van Roy, J. De Boeck, J. M. Tang, and M. E. Flatté. Spatial structure of an individual Mn acceptor in GaAs. *Phys. Rev. Lett.*, 92(21):216806–1, 2004.

[10] Kitiphat Sinthiptharakoon, Steven R Schofield, Philipp Studer, Veronika Brázdová, Cyrus F Hirjibehedin, David R Bowler, and Neil J Curson. Investigating individual arsenic dopant atoms in silicon using low-temperature scanning tunnelling microscopy. *J. Phys. Condens. Matter*, 26(1):012001, dec 2013.

[11] Qing Hua Wang, Kourosh Kalantar-Zadeh, Andras Kis, Jonathan N Coleman, and Michael S Strano. Electronics and optoelectronics of two-dimensional transition metal dichalcogenides. *Nat. Nanotechnol.*, 7(11):699–712, 2012.

[12] Amity Andersen, Shawn M. Kathmann, Michael a. Lilga, Karl O. Albrecht, Richard T. Hallen, and Donghai Mei. First-principles characterization of potassium intercalation in hexagonal 2H-MoS2. *J. Phys. Chem. C*, 116:1826–1832, 2012.

[13] Roscoe G Dickinson and Linus Pauling. The crystal structure of molybdenite. *J. Am. Chem. Soc.*, 45(6):1466–1471, 1923.

[14] R. Murray and B. Evans. The thermal expansion of 2H-MoS2 and 2H-WSe2 between 10 and 320 K. *J. Appl. Crystallogr.*, 12(3):312–315, 1979.

[15] M. Haider, Jason Pitters, Gino DiLabio, Lucian Livadaru, Josh Mutus, and Robert Wolkow. Controlled Coupling and Occupation of Silicon Atomic Quantum Dots at Room Temperature. *Phys. Rev. Lett.*, 102(4):046805, jan 2009.

[16] Lucian Livadaru, Jason Pitters, Marco Taucer, and Robert Wolkow. Theory of nonequilibrium single-electron dynamics in STM imaging of dangling bonds on a hydrogenated silicon surface. *Phys. Rev. B*, 84(20):1–14, nov 2011.

[17] Marco Taucer, Lucian Livadaru, Paul G. Piva, Roshan Achal, Hatem Labidi, Jason L. Pitters, and Robert A. Wolkow. Single-Electron Dynamics of an Atomic Silicon Quantum Dot on the H-Si(100)-(2x1) Surface. *Phys. Rev. Lett.*, 112(25):256801, jun 2014.

[18] Taro Hitosugi, S Heike, T Onogi, T Hashizume, S Watanabe, Z Li, K Ohno, Y Kawazoe, T Hasegawa, and K Kitazawa. Jahn-Teller Distortion in Dangling-Bond Linear Chains Fabricated on a Hydrogen-Terminated Si(100)-2x1 Surface. *Phys. Rev. Lett.*, 82(100):4034, 1999.

[19] Wei Ye, Kyoungmin Min, Pamela Peña Martin, Angus A. Rockett, N.R. Aluru, and Joseph W. Lyding. Scanning tunneling spectroscopy and density functional calculation of silicon dangling bonds on the Si(100)-2x1:H surface. *Surf. Sci.*, 609:147–151, mar 2013.

[20] N Nilius T. M. Wallis and W. Ho. Electronic Density Oscillations in Gold Atomic Chains Assembled Atom by Atom. *Phys. Rev. Lett.*, 89:236802, 2002.

[21] S. Fölsch, P. Hyldgaard, R. Koch, and K. H. Ploog. Quantum wire behavior in a one-component metallic system: Monatomic Cu chains on Cu(1 1 1). *Phys. E Low-Dimensional Syst. Nanostructures*, 24(1-2 SPEC. ISS.):111–114, 2004.

[22] Keisuke Sagisaka and Daisuke Fujita. Quasi-one-dimensional quantum well on Si(100) surface crafted by using scanning tunneling microscopy tip. *Appl. Phys. Lett.*, 88(20):203118, 2006.

[23] B. Fain, J. C. Girard, D. Elvira, C. David, G. Beaudoin, A. Beveratos, I. Robert-Philip, I. Sagnes, and Z. Z. Wang. Electronic structure of cleaved InAsP/InP(001) quantum dots measured by scanning tunneling spectroscopy. *Appl. Phys. Lett.*, 97(17):1–4, 2010.

[24] Stefan Fölsch, Jesús Martínez-Blanco, Jianshu Yang, Kiyoshi Kanisawa, and Steven C. Erwin. Quantum dots with single-atom precision. *Nat. Nanotechnol.*, 9(June):505–508, jun 2014.

[25] M F Crommie, C P Lutz, and D M Eigler. Confinement of electrons to quantum corrals on a metal surface. *Science*, 262(5131):218–220, 1993.

[26] Jason L Pitters, Iana A Dogel, and Robert A Wolkow. Charge control of surface dangling bonds using nanoscale Schottky contacts. *ACS Nano*, 5(3):1984–9, mar 2011.

[27] Takashi Kumagai, Felix Hanke, Sylwester Gawinkowski, John Sharp, Konstantinos Kotsis, Jacek Waluk, Mats Persson, and Leonhard Grill. Controlling intramolecular hydrogen transfer in a porphycene molecule with single atoms or molecules located nearby. *Nat. Chem.*, 6(1):41–6, jan 2014.

[28] D H Lee and J A Gupta. Tunable field control over the binding energy of single dopants by a charged vacancy in GaAs. *Science*, 330(6012):1807–10, dec 2010.

[29] Kin Fai Mak, Changgu Lee, James Hone, Jie Shan, and Tony F. Heinz. Atomically thin MoS2: A new direct-gap semiconductor. *Phys. Rev. Lett.*, 105(13):2–5, 2010.

[30] T. Eknapakul, P. D C King, M. Asakawa, P. Buaphet, R. H. He, S. K. Mo, H. Takagi, K. M. Shen, F. Baumberger, T. Sasagawa, S. Jungthawan, and W. Meevasana. Electronic structure of a quasi-freestanding MoS2 monolayer. *Nano Lett.*, 14(3):1312–1316, 2014.

[31] C. J. Arguello, S. P. Chockalingam, E. P. Rosenthal, L. Zhao, C. Gutiérrez, J. H. Kang, W. C. Chung, R. M. Fernandes, S. Jia, A. J. Millis, R. J. Cava, and A. N. Pasupathy. Visualizing the charge density wave transition in 2H-NbSe2 in real space. *Phys. Rev. B*, 89(23):235115, jun 2014.

[32] Miguel M Ugeda, Aaron J Bradley, Yi Zhang, Seita Onishi, Yi Chen, Wei Ruan, Claudia Ojeda-Aristizabal, Hyejin Ryu, Mark T Edmonds, Hsin-zon Tsai, Alexander Riss, Sung-Kwan Mo, Dunghai Lee, Alex Zettl, Zahid Hussain, Zhi-Xun Shen, and Michael F. Crommie. Characterization of collective ground states in single-layer NbSe2. *Nat. Phys.*, 12(1):92–97, nov 2015.

[33] Matteo Calandra, I. I. Mazin, and Francesco Mauri. Effect of dimensionality on the charge-density wave in few-layer 2 H-NbSe2. *Phys. Rev. B - Condens. Matter Mater. Phys.*, 80(24):1–4, 2009.

[34] A. M. Novello, B. Hildebrand, A. Scarfato, C. Didiot, G. Monney, A. Ubaldini, H. Berger, D. R. Bowler, P. Aebi, and Ch. Renner. Scanning tunneling microscopy of the charge density wave in TiSe2 in the presence of single atom defects. *Phys. Rev. B*, 92(8):081101, 2015.

[35] Sara Barja, Sebastian Wickenburg, Zhen-fei Liu, Yi Zhang, Hyejin Ryu, Miguel M. Ugeda, Zahid Hussain, Zhi-Xun Shen, Sung-kwan Mo, Ed Wong, Miquel B. Salmeron, Feng Wang, Michael F Crommie, D Frank Ogletree, Jeffrey B. Neaton, and Alexander Weber-Bargioni. Charge density wave order in 1D mirror twin boundaries of single-layer MoSe2. *Nat. Phys.*, (April):1–26, apr 2016.

[36] K.C. Rahnejat, C.A. Howard, N.E. Shuttleworth, S.R. Schofield, K. Iwaya, C.F. Hirjibehedin, C. Renner, G. Aeppli, and M. Ellerby. Charge density waves in the graphene sheets of the superconductor CaC(6). *Nat. Commun.*, 2:556–558, 2011.

[37] B. J. Van Zeghbroeck. Effective mass in semiconductors. `http://ecee.colorado.edu/~bart/book/effmass.htm`, 1997.

[38] A. Asenov, A.R. Brown, J.H. Davies, S. Kaya, and G. Slavcheva. Simulation of intrinsic parameter fluctuations in decananometer and nanometer-scale MOSFETs. *IEEE Trans. Electron Devices*, 50(9):1837–1852, sep 2003.

[39] J R Weber, W F Koehl, J B Varley, A Janotti, B B Buckley, C G Van de Walle, and D D Awschalom. Quantum computing with defects. *Proc. Natl. Acad. Sci. U. S. A.*, 107(19):8513–8, may 2010.

[40] L. Mayor. Stacking up 2d materials. *Physics World*, 29(5):28–29, May 2016.

[41] Xiaomu Wang and Fengnian Xia. Van der Waals heterostructures: Stacked 2D materials shed light. *Nat. Mater.*, 14(3):264–265, 2015.

[42] G Binnig, H Rohrer, C Gerber, and E Weibel. Surface studies by scanning tunneling microscopy. *Phys. Rev. Lett.*, 49(1):57–61, 1982.

[43] C. J. Chen. *Introduction to Scanning Tunneling Microscopy*. Oxford series in optical and imaging sciences. Oxford University Press, 1993.

[44] D. K. Schweizer and E. K. Eigler. Positioning single atoms with a scanning tunneling microscop, 1990.

[45] A. I. M. Rae. *Quantum Mechanics*. Taylor & Francis, fifth edition, 2007.

[46] D. A. Bonnell, editor. *Scanning Probe Microscopy and Spectroscopy*. Wiley-VCH, second edition, 2001.

[47] J Tersoff and Dr Hamann. Theory and application for the scanning tunneling microscope. *Phys. Rev. Lett.*, 50(25):1998, 1983.

[48] R. M. Feenstra. Electrostatic potential for a hyperbolic probe tip near a semiconductor. *J. Vac. Sci. Technol. B Microelectron. Nanom. Struct.*, 21(5):2080, 2003.

[49] Robert H. Kingston and Siegfried F. Neustadter. Calculation of the Space Charge, Electric Field, and Free Carrier Concentration at the Surface of a Semiconductor. *J. Appl. Phys.*, 26(6):718, 1955.

[50] R Seiwatz and M Green. Space Charge Calculations for Semiconductors. *J. Appl. Phys.*, 29(7):1034–1040, 1958.

[51] D. J. Chadi. Atomic and Electronic Structures of Reconstructed Si(100) Surfaces. *Phys. Rev. Lett.*, 43(1):43–47, jul 1979.

[52] J. Dąbrowski and H. J. Müssig. *Silicon Surfaces and Formation of Interfaces*. World Scientific, 2000.

[53] P. Y. Yu and M. Cardona. *Fundamentals of Semiconductors: Physics and Material Properties*. Springer, third edition, 2005.

[54] M. D. McCluskey and E. E. Haller. *Dopants and Defects in Semiconductors*. CRC Press, 2012.

[55] P T Greenland, S a Lynch, a F G van der Meer, B N Murdin, C R Pidgeon, B Redlich, N Q Vinh, and G Aeppli. Coherent control of Rydberg states in silicon. *Nature*, 465(7301):1057–61, jun 2010.

[56] J. R. Hook and H. E. Hall. *Solid State Physics*. The Manchester physics series. Wiley, second edition, 1991.

[57] S. M. Sze and K. K. Ng. *Physics of Semiconductor Devices*. Wiley, third edition, 2007.

[58] B Pajot and A M Stoneham. A Spectroscopic Investigation Of The Lattice Distortion At Substitutional Sites For Group-V And Group-VI Donors In Silicon. *J. Phys. C-Solid State Phys.*, 20(32):5241–5252, 1987.

[59] J. P. Campbell and P. M. Lenahan. Density of states of Pb1 Si/SiO2 interface trap centers. *Appl. Phys. Lett.*, 80(11):1945, 2002.

[60] Frank J. Ruess, Lars Oberbeck, Michelle Y. Simmons, Kuan Eng J. Goh, Alex R. Hamilton, Toby Hallam, Steven R. Schofield, Neil J. Curson, and Robert G. Clark. Toward Atomic-Scale Device Fabrication in Silicon Using Scanning Probe Microscopy. *Nano Lett.*, 4(10):1969–1973, oct 2004.

[61] Paul G Piva, Gino a DiLabio, Jason L Pitters, Janik Zikovsky, Moh'd Rezeq, Stanislav Dogel, Werner a Hofer, and Robert a Wolkow. Field regula-

tion of single-molecule conductivity by a charged surface atom. *Nature*, 435(7042):658–61, jun 2005.

[62] R. J. Hamers. Characterization of localized atomic surface defects by tunneling microscopy and spectroscopy. *J. Vac. Sci. Technol. B Microelectron. Nanom. Struct.*, 6(4):1462, jul 1988.

[63] K. Teichmann, M. Wenderoth, S. Loth, R. Ulbrich, J. Garleff, a. Wijnheijmer, and P. Koenraad. Controlled Charge Switching on a Single Donor with a Scanning Tunneling Microscope. *Phys. Rev. Lett.*, 101(7):076103, aug 2008.

[64] M. van der Wielen, a. van Roij, and H. van Kempen. Direct Observation of Friedel Oscillations around Incorporated SiGa Dopants in GaAs by Low-Temperature Scanning Tunneling Microscopy. *Phys. Rev. Lett.*, 76(7):1075–1078, 1996.

[65] Katsuyoshi Kobayashi. Mechanism of subsurface imaging in scanning tunneling microscopy. *Ultramicroscopy*, 73(1-4):163–168, 1998.

[66] G. Grüner. The dynamics of charge-density waves. *Rev. Mod. Phys.*, 60(4):1129–1181, 1988.

[67] Jt T Ye, Yj J Zhang, R. Akashi, Ms S Bahramy, R Arita, and Y Iwasa. Superconducting Dome in a Gate-Tuned Band Insulator. *Science (80-.).*, 338(6111):1193–1196, 2012.

[68] D. Jiang K. S. Novoselov A. K. Geim S. V. Morozov and A. A. Firsov Y. Zhang S. V. Dubonos I. V. Grigorieva. Electric Field Effect in Atomically Thin Carbon Films. *Science (80-.).*, 306(5696):666–669, oct 2004.

[69] K S Novoselov, D Jiang, F Schedin, T J Booth, V V Khotkevich, S V Morozov, and A K Geim. Two-dimensional atomic crystals. *Proc. Natl. Acad. Sci. U. S. A.*, 102(30):10451–10453, 2005.

[70] C. Kittel. *Introduction to Solid State Physics*. John Wiley & Sons, Inc., sixth edition, 1986.

[71] C. Bird, A. Fisher, and D. Bowler. Soliton effects in dangling-bond wires on Si(001). *Phys. Rev. B*, 68(11):115318, sep 2003.

[72] Aaron J. Bradley, Miguel M. Ugeda, Felipe H. Da Jornada, Diana Y. Qiu, Wei Ruan, Yi Zhang, Sebastian Wickenburg, Alexander Riss, Jiong Lu, Sung Kwan Mo, Zahid Hussain, Zhi Xun Shen, Steven G. Louie, and Michael F. Crommie. Probing the Role of Interlayer Coupling and Coulomb Interactions on Electronic Structure in Few-Layer MoSe2 Nanostructures. *Nano Lett.*, 15(4):2594–2599, 2015.

[73] Katsuyoshi Kobayashi and Jun Yamauchi. Electronic structure and scanning-tunneling-microscopy image of molybdenum dichalcogenide surfaces. *Phys. Rev. B*, 51(23):17085–17095, 1995.

[74] Anjan Soumyanarayanan, Michael M Yee, Yang He, Jasper van Wezel, Dirk J Rahn, Kai Rossnagel, E W Hudson, Michael R Norman, and Jennifer E Hoffman. Quantum phase transition from triangular to stripe charge order in NbSe2. *Proc. Natl. Acad. Sci. U. S. A.*, 110(5):1623–7, 2013.

[75] C. Monney, E. F. Schwier, M. G. Garnier, N. Mariotti, C. Didiot, H. Beck, P. Aebi, H. Cercellier, J. Marcus, C. Battaglia, H. Berger, and A. N. Titov. Temperature-dependent photoemission on 1T -TiSe2: Interpretation within the exciton condensate phase model. *Phys. Rev. B - Condens. Matter Mater. Phys.*, 81(15):1–9, 2010.

[76] Chen Wang, B. Giambattista, C. Slough, R. Coleman, and M. Subramanian. Energy gaps measured by scanning tunneling microscopy. *Phys. Rev. B*, 42(14):8890–8906, 1990.

[77] J.A. Wilson, F.J. Di Salvo, and S. Mahajan. Charge-density waves and superlattices in the metallic layered transition metal dichalcogenides. *Adv. Phys.*, 24(2):117–201, 1975.

[78] Ion getter and titanium sublimation pumps. `https://www.vacom.de/en/downloads/vacom-product-catalog`, March 2016.

[79] S. R. Schofield. A collection of data analysis macros for igor pro. https://github.com/dleifohcs/srs-igor, May 2016.

[80] Inger Ekvall, Erik Wahlström, Dan Claesson, Håkan Olin, and Eva Olsson. Preparation and characterization of electrochemically etched W tips for STM. *Meas. Sci. Technol.*, 10(1):11–18, jan 1999.

[81] B. S. Swartzentruber. Scanning tunneling microscopy studies of structural disorder and steps on Si surfaces. *J. Vac. Sci. Technol. A Vacuum, Surfaces, Film.*, 7(4):2901, jul 1989.

[82] Jason L. Pitters, Paul G. Piva, and Robert a. Wolkow. Dopant depletion in the near surface region of thermally prepared silicon (100) in UHV. *J. Vac. Sci. Technol. B Microelectron. Nanom. Struct.*, 30(2):021806, 2012.

[83] R. B. Somoano, V. Hadek, and A. Rembaum. Alkali metal intercalates of molybdenum disulfide. *J. Chem. Phys.*, 697(1973):4–9, 1973.

[84] S. Janecek and E. Krotscheck. A fast and simple program for solving local Schrödinger equations in two and three dimensions. *Comput. Phys. Commun.*, 178(11):835–842, jun 2008.

[85] R. M. Feenstra. Semitip, version 6. http://www.andrew.cmu.edu/user/feenstra/semitip_v6/, May 2011.

[86] R M Feenstra, Y Dong, M P Semtsiv, and W T Masselink. Influence of tip-induced band bending on tunnelling spectra of semiconductor surfaces. *Nanotechnology*, 18:044015, 2006.

[87] A. M. Suleman. Investigating tip-induced band bending on the silicon surface. Master's thesis, University College London, 2012.

[88] D. R. Lide, editor. *Handbook of Chemistry and Physics*. CRC Press, 84 edition, October 2003.

[89] Gerd Binnig and Heinrich Rohrer. Scanning tunneling microscopyfrom birth to adolescence. *Rev. Mod. Phys.*, 59(3):615–625, 1987.

[90] Albert Bruix, Jill A. Miwa, Nadine Hauptmann, Daniel Wegner, Soren Ulstrup, Signe S. Gronborg, Charlotte E. Sanders, Maciej Dendzik, Antonija Grubisic Cabo, Marco Bianchi, Jeppe V. Lauritsen, Alexander A. Khajetoorians, Bjork Hammer, and Philip Hofmann. Single-layer MoS2 on Au(111): Band gap renormalization and substrate interaction. *Phys. Rev. B - Condens. Matter Mater. Phys.*, 93(16):165422, 2016.

[91] S. Loth. *Atomic Scale Images of Acceptors in III-V Semiconductors Atomic Scale Images of Acceptors in III-V Semiconductors Atomic Scale Images of Acceptors in III-V Semiconductors*. PhD thesis, Göttingen University, 2008.